Title
Neuron structure-function correspondence as revealed by biological scaling theory

Author
Desai-Chowdhry, Paheli

Publication Date
2023

Peer reviewed|Thesis/dissertation

UNIVERSITY OF CALIFORNIA

Los Angeles

Neuron structure-function correspondence as revealed by biological scaling theory

A dissertation submitted in partial satisfaction
of the requirements for the degree
Doctor of Philosophy in Biomathematics

by

Paheli Desai-Chowdhry

2023

ABSTRACT OF THE DISSERTATION

Neuron structure-function correspondence
as revealed by biological scaling theory

by

Paheli Desai-Chowdhry
Doctor of Philosophy in Biomathematics
University of California, Los Angeles, 2023
Professor Van M. Savage, Chair

Neurons are connected by complex branching processes that collectively process information for organisms to respond to their environment. Classifying neurons according to differences in structure or function is a fundamental piece of neuroscience. Here, by constructing new biophysical theory and testing against our empirical measures of branching structure, we establish a correspondence between neuron structure and function as mediated by principles such as time or power minimization for information processing as well as spatial constraints for forming connections. Based on these principles, we use Lagrange multipliers to predict scaling ratios for axon and dendrite sizes across branching levels. We test our predictions for radius scale factors against those extracted from images, measured for species that range from insects to whales. Notably, our findings reveal that the branching of axons and peripheral nervous system neurons is mainly determined by time minimization, while dendritic branching is mainly determined by power minimization. Further comparison of different dendritic cell types reveals that Purkinje cell dendrite branching is constrained by material costs while motoneuron dendrite branching is constrained by conduction time delay. We

extend this model to incorporate asymmetric branching, where there are multiple different paths from the soma to the synapses and thus multiple interpretations of conduction time delay; one considers the optimal path and the other considers the sum of all possible paths, leading to different predictions. We find that the data for motoneurons show a distinction between the asymmetric and symmetric branching junctions, corresponding to predictions using different interpretations of the time-delay constraint. Moreover, the more asymmetric branching junctions are localized near the synapses, indicating that different functional principles affect the structure at different regions of the cell. Finally, we use machine-learning methods to classify cell types using functionally relevant structural parameters derived from our model. Incorporating branching level as a feature in classification in addition to parameters related to information flow improves performance across methods, suggesting that information flow drives localized differences in morphology. Future directions of this work include estimating specific parameters related to functional tradeoffs and myelination using numerical optimization and analyzing changes across stages of development.

The dissertation of Paheli Desai-Chowdhry is approved.

Marcus L. Roper

Sriram Sankararaman

Mary E. Sehl

Daniel J. Tward

Van M. Savage, Committee Chair

University of California, Los Angeles

2023

To my parents,

who inspired my love of school and learning,

and my mentors in high school, college, and graduate school,

who gave me confidence in my ability to pursue science and mathematics.

TABLE OF CONTENTS

LIST OF FIGURES

LIST OF TABLES

ACKNOWLEDGMENTS

First, I would like to acknowledge my advisor, Van Savage, whose curiosity, knowledge, and openness was instrumental in all of this work. When I first came to visit UCLA and began telling him about my interests in neuroscience, he responded with enthusiasm - although the lab did not focus on neuroscience, he explained that he had long wondered about the applicability of the image software used to study vessels to look at neurons. Throughout my time at UCLA, I could not have asked for a more smooth graduate school experience, and it has been in large part due to the atmosphere in the Savage lab. I have always felt comfortable discussing ideas with him, even in the early stages, and I have always resonated with his approach to biomathematics - his questions are initially motivated by the biology, and his knowledge of applied mathematics is what carries those questions forward. I'm tremendously grateful to have had this opportunity not only to learn from him, but also to develop as an independent researcher. His willingness to discuss even half-baked ideas has helped me grow more confident in being more comfortable with the uncertainty that is inherent in research.

Second, I would like to acknowledge Alex Brummer, a former postdoc in our lab and current professor at the College of Charleston, South Carolina, without whom this work would not be possible. Much of this work, including the complicated asymmetric branching calculations, were inspired by mathematical framework of his extension of scaling theory in vascular networks to include branching asymmetry. Having used his calculations as a road map for my own, and as a source of consultation when I've been stuck, I have truly come to appreciate the intelligence and creativity with which he built the framework from scratch. Moreover, he was an amazing mentor, and I could always count on him to send me long, detailed email explanations in response to even my smallest questions, and to schedule zoom meetings with me that helped keep me afloat during the pandemic.

I would also like to acknowledge my current and former labmates, Mauricio Cruz-Loya, Jason Lin, and Shaili Mathur. Mauricio, in particular, has been an immense source of

support for me throughout the Biomathematics PhD program, and I greatly benefitted from his detailed notes and derivations that helped get me through studying for the comprehensive exams. Shaili has been a great source of inspiration for me as a very precocious undergraduate student, now a graduate student at Stanford, who was always willing to discuss ideas with me and help me prepare for presentations. I would like to acknowledge my undergraduate mentee, Samhita Mallavarapu, who has contributed to a lot of preprocessing and visualization for the data in this work, and whose willingness to learn and immense progress throughout the course of her time working under my supervision has reaffirmed my passion for mentorship and teaching.

I would like to acknowledge my committee, Marcus Roper, Sriram Sankararaman, Mary Sehl, and Daniel Tward, whose instruction, questions, and criticism have driven forward this research, particularly for the Machine-Learning classification project, in directions that I'm not sure they would've otherwise reached. I would like to acknowledge Janet Sinsheimer, who was the first person I met at UCLA and who personally reached out to me when I was admitted to discuss the program and her experience as a woman in the program. She is deeply missed, and her contributions to the community will be forever remembered and celebrated. I would like to acknowledge Marilyn Gray, my supervisor at the Graduate Writing Center at UCLA, which has been an important and rewarding part of my experience here. I want to acknowledge Samantha Andrews, Emily Fitch, Stacey Beggs, and Trisha Mazumder, the staff at UCLA Biomathematics and the GWC who have been responsible for the logistics that have made all the program functions possible.

I would like to acknowledge my mentors from my undergraduate research experiences who have continued to inspire and support me. In particular, I would like to thank Sasha Shirman, my former physics instructor who helped bring me into research, without whom I would have never had the confidence to apply for a PhD in this field, and Professor Henry Abarbanel for supporting my research interests and including me in his group as an undergrad. I would like to thank Eve Armstrong, whose comfort with acknowledging the uncertainty in science

and research has inspired much of my perspective today, and her letter of recommendation helped me obtain the funding that has made my graduate school experience possible. I would like to acknowledge Anna Miller, whose friendship and support has been consistent from the time we shared an office in my undergraduate research group through graduate school.

I would like to thank my colleagues in Biomathematics who I have not already mentioned, Gabriel Hassler, Vicky Kelley, Jianxiao Yang, Bhaven Mistry, Benjamin Chu, Alfonso Landeros, Sam Christensen, Rachel Mester, Mariana Harris, Christine Craib, and Siqi Fang. Gabe has helped me throughout my experience in the program, from discussing the courses with me to emotional support through the ups and downs of research. Vicky was one of my first friends at UCLA, and her kindness and energy will always amaze me. Jianxiao has been my primary source of support and camaraderie in getting through exams, as the only other PhD student in my year. Rachel has been the one person to get me out of the house the most, and whose weekly Friday morning swimming plans have kept me functional.

I would like to thank my friends outside of the program who have shaped my time in graduate school. In particular, I want to thank Daria Bazzi, Drishti Saxena, Julie Wiedemann, Jar-Yee Liu, Natella Baliaouri, Reyna Bhakta, Shreya Mukund, and Kim Cárdenas, whose daily support and humor has gotten me through graduate school. I also want to thank Rob Ulrich, Erin Bacasen, Christopher Ikonomou, and Claire Polizu for facilitating the communities and student organizations that have helped me feel more connected to the broader UCLA community. I want to thank my parents, Swati Desai and Bhagwan Chowdhry, whose love of school and education inspired mine, my dog, Lily, my constant companion, my brother, Saransh Desai-Chowdhry, for being a constant source of support and inspiration, and my aunt, Reeta Desai, who has been my local emergency contact in Los Angeles throughout the course of graduate school and who has been like a second mother to me.

I would like to acknowledge the National Science Foundation (NSF grant number DGE-1650604 and DGE-2034835) and the National Institutes of Health (NIH grant number 2T32GM008185-31 and 5T32GM008185-32) for the funding that has made all of this possible.

VITA

2012-2017 Tutor. Taught elementary through college level Mathematics and Science.

2016-2018 Undergraduate Research Assistant, Professor Henry Abarbanel's Research Group, Physics Department, University of California, San Diego.

2018 B.S. (Mathematics, Applied Science), University of California, San Diego.

2018–present Research Assistant, Biomathematics Department, UCLA. Fellow, NIH SIBTG (T32) and NSF GRFP. Mathematical modeling of neurons.

2020–present Consultant and STEM Masters Thesis Mentor, Graduate Writing Center, UCLA. Supported fellow graduate students with writing fellowship applications, personal statements, manuscripts, and thesis projects.

2021 Teaching Assistant, Computational and Systems Biology, UCLA. Taught a laboratory section of an upper-division course in mathematical and computational modeling in biology under the direction of Professor Van Savage.

2021-2023 Undergraduate Research Mentor, Computational and Systems Biology, UCLA. Supervised an undergraduate student, Samhita Mallavarapu. Oversaw research projects and provided training in programming skills.

PUBLICATIONS AND PRESENTATIONS

Paheli Desai-Chowdhry, Alexander B Brummer, and Van M Savage. "How axon and dendrite branching are guided by time, energy, and spatial constraints" In: *Scientific Reports* 12, 20810 (2022). https://doi.org/10.1038/s41598-022-24813-2

Paheli Desai-Chowdhry, Alexander B Brummer, Samhita Mallavarpu, and Van M Savage. "Neuronal Branching is Increasingly Asymmetric Near Synapses, Potentially Enabling Plasticity While Minimizing Energy Dissipation and Conduction Time." In: *Under Review* (2023). https://doi.org/10.1101/2023.05.20.541591

Paheli Desai-Chowdhry, Alexander B Brummer, Samhita Mallavarapu, and Van M Savage. "Information Flow Drives Localized Morphological Differences Across Neuronal and Glial Cell Types." In: *In Preparation* (2023).

Paheli Desai-Chowdhry, Alexander B Brummer, and Van M Savage. "Scaling Theory in Axons and Dendrites." *SIAM (Society for Industrial and Applied Mathematics) Annual Meeting.* Zoom (July 2021). Oral.

Paheli Desai-Chowdhry, Alexander B Brummer, and Van M Savage. "Asymmetric Branching Scale Factors as Features in Neuronal and Glial Cell-Type Classification Using Machine Learning Methods." *APS (American Physical Society) March Meeting.* Chicago, IL, US (March 2022). Oral.

Paheli Desai-Chowdhry, Alexander B Brummer, and Van M Savage. "Axons and Dendrites Branching Structure-Function Correspondence" *International Conference on Mathematical Neuroscience (ICMNS).* Zoom (July 2022). Oral.

Paheli Desai-Chowdhry. "Dynamics and Complexity" *Gordon Research Seminar (GRS) Unifying Ecology Across Scales.* Manchester, NH, US, (July-August 2022). Oral (Discussion Leader).

CHAPTER 1

Introduction

Over the last 200 years, the advent of advanced microscopy techniques and staining methods has led to the conceptualization of neurons as independent cellular units of the nervous system. The Spanish neuroanatomist Santiago Ramón y Cajal utilized the Golgi staining technique to make detailed drawings of neurons, comparing neurons across a range of cell types and species [130]. This work not only established the existence of multiple cell types, but showed that specific cell types were characteristic of localized regions of the nervous system. The Golgi staining technique allowed for the discernment of treelike processes—axons and dendrites—extending from the soma (cell body) of neurons [51]. The diversity in form and function of dendrites suggests that they have evolved to fill a range of functional roles in the nervous system [126]. Indeed, Ramón y Cajal argued that the diversity of morphological forms in neuron processes could all be explained by the physical laws of conservation for time, space, and material [24]. This work, presented in "Histology of the Nervous System of Man and Vertebrates," is considered the founding document of neurobiology, and is possibly the only document over 100 years old that is still regularly consulted by neuroscientists. This documement is arguably the first attempt at cell-type classification in neuroscience. As neuron cell types differ based on characteristic morphological, physiological, molecular, and connectional properties, the most reasonable approach to understanding this complexity, and how it integrates to the structure and function of brain circuits, is attempting to cluster the diverse cells into characteristic groups [130].

The two classes of neuron processes, axons and dendrites, differ in both function and

form. Axons, with their long parent branches sometimes extending across distances of over a meter and projecting between regions of the nervous system [94], generally conduct signals from the soma to the synapses, where they connect to other neurons, and have likely evolved to minimize conduction time delay [30]. Axons are electrically active and conduct action potentials, and they play an essential role in transferring large amounts of information between brain areas in a short amount of time [64]. In contrast, dendrites have shorter parent branches and more extensive branching trees, carrying signals from the synapses to the soma and generally relying on passive electronic spread [94]. Thus, it is likely that different principles related to the attenuation of signals are more important factors governing the structures of dendrites than for axons [30].

Neuronal tissue is energetically costly to operate and maintain, creating pressures to minimize metabolic energy costs in signalling [12]. While attempts have been made to quantitatively describe Ramón y Cajal's laws using graph theory [36], generating realistic synthetic neurons [37], this approach is limited because it does not take into account these metabolic factors that affect information flow in neurons. An important consideration in the design of neurons is the functional tradeoff between material costs, energetic costs, and time costs. Although wider fibers exhibit less attentuation of passive signals, rendering both passive spread and active propagation faster [94], creating fibers of larger width and thus volume increase both material costs and energetic costs needed for maintenance [64, 121, 97]. Moreover, an important adaptation of the nervous system is myelination—a fatty sheath that surrounds fibers and speeds up conduction [109]. Foundational experimental and theoretical work has shown that the conduction time delay decreases for myelinated fibers; the conduction velocity is proportional to the square root of the diameter of neuron fibers for unmyelinated fibers, and proportional to the diameter itself for myelinated fibers [52, 100]. Thus, studies that focus solely on the path length of neuron processes in order to optimize conduction time ignore key attributes—conduction speed and its relation to the radius—that drive information processing in the nervous system.

Another potential consequence of this tradeoff between time delay and metabolic costs is hemispheric specialization. Previous studies have shown that for some cells, there is an allometric scaling relationship between cell size and body mass of species [104] that applies to a range of biological cells, including neurons. If larger animals have processes that have a larger volume, and therefore are wider,they may conduct signals more rapidly but will do so at the expense of a metabolic and material cost that is associated with the larger volume [121]. On the other hand, some specific types of neurons have been observed to be invariant in size in relation to species size [126]. Previous studies have proposed that hemispheric specialization is an adaptation that arises in larger animals in order to offset the long conduction time delays that are associated with cells remaining the same width within larger brains; that is, cells that often communicate with one another are clustered closer to each other [97].

A promising approach to address this complexity of the structure-function relationship and the tradeoffs that occur across neuron cell-types is biological scaling theory, as it has previously been applied to relate branching structures in other biological networks—such as blood vessels and plants—to functional properties related to transport, material costs, and space-filling. West, Brown, and Enquish (WBE) proposed that allometric biological scaling relationships, such as Kleiber's law, which relates body mass to metabolic rate via a 3/4 exponent [60], arise due to resource distribution networks that are optimized to supply all parts of the body [125]. The branching processes of neurons, emerging from the soma, are analogous to the branching vessels in cardiovascular networks, emerging from the heart. Moreover, previous work has characterized branching blood vessels using analogous mathematical descriptions of electrical circuits [129], implying that there might also be functional similarities between these diverse biological systems. These structural and functional similarities suggest that applying the mathematical framework developed to study the relationship between branching patterns of blood vessels and transport, metabolism, material costs, and space-filling [103, 22, 23] might be useful in developing a framework to understand

the functional tradeoffs across cell types in the nervous system.

There are vast amounts of data available online in public repositories that allow us to analyze morphological properties in neurons and test our theoretical predictions based on biophysics models to empirical quantities, allowing us to further develop the model. In this study, we focus on one resource, NeuroMorpho.Org [10]—a publicly accessible archive of digital reconstructions of neuron morphology. This archive has neurons from a range of species and sizes—from insects and rodents to elephants and whales—allowing for cross-species comparisons and analysis of potential allometric relationships. The morphological data is collected using a range of microscopy techniques, including light microscopy and electron microscopy, as well as a range of software techniques used to trace the images into 3-dimensional quantitative reconstruction data [10]. The data is organized according to cell-types and brain regions, and there is also data available from human patients that is labelled by disease such as epilepsy and cancer.

There is also a remarkable amount of data available for non-neuronal nervous systems cells. For a long time, it was thought that these cells, named glia based on the greek word for glue, basically functioned as structural aids for neurons without any function of their own [53]. However, recent work has revealed that they have diverse functions that contribute to brain function and information processing. In particular, astrocytes and microglia have been shown to respond to electrical stimulation [45]. They have branching processes that are comparable to neurons, allowing for a similar method of analysis. The vast amounts of data available at NeuroMorpho.Org are the result of shared efforts from labs all over the world. Moreover, the archive is constantly being updated [10], providing many opportunities to further our understanding.

Our work here makes use of these valuable resources and the existing mathematical framework used to describe cardiovascular networks to tackle the problem of cell-type classification and understanding the relationship between structure and function in the nervous system. Chapter 2 establishes a unifying model that describes the relationship between structure

and function in neurons, combining the principles of minimizing conduction time delay and energetic costs while taking into account material costs and space-filling constraints. The parameters of this model can be adjusted for a variety of factors such as myelinated versus unmyelinated fibers, and consideration of different tradeoffs. Theoretical predictions of morphological quantities in this model are compared to distributions in morphological data across a range of species and cell types. Correspondences are drawn between specific cases of the model that lead to predictions that agree with specific cell and process types. In addition to these correspondences that apply across species of different sizes, an allometric scaling relationship between conduction time delay and body mass is extracted from this model and validated using data.

Chapter 3 explores relaxing the assumption of symmetric branching that is imposed in Chapter 2, allowing for further important insights. While the symmetric assumption implies that all paths from the soma to the synapses are equal in length, asymmetric branching leads to multiple possible paths of varying lengths. When optimizing the structure for time delay, which path is most important to minimize? Is it the shortest path? The longest path? Some combination of all the paths? This chapter considers theoretical predictions based on all these possible interpretations, and finds that different interpretations correspond to the median values in the data corresponding to different regions in the cell, suggesting that even within a single cell, there are multiple regimes describing different structure-function correspondences. Moreover, the presence of asymmetric branching appears to be localized at specific regions, leading to important hypotheses about the functional underpinnings of asymmetric branching in neurons.

Chapter 4 extends this framework of asymmetric branching networks, combining the theory with machine-learning classification methods to highlight difference between different types of neuronal dendrites as well as between different types of glial cells, astrocytes and microglia. Although machine-learning is often a black box, obscuring mechanistic insight into the clustering of data into groups, the use of parameters related to information flow in

nerve cell processes from the theory provides insight into the functional basis that underlies observed differences in structure. The incorporation of a third factor related to the spatial position of branching junctions relative to the cell body and synapses improves the performance of classification methods—particularly for distinguishing glial cells—suggesting that the differences in information flow are localized to specific regions of the cell.

We apply these methods to observe morphological differences between healthy and diseased cells, identifying localized morphological differences in pyramidal cells of tumor and epilepsy patients compared to control cells. These results highlight the promise of our methods to apply to larger datasets and address important problems in neuroscience such as characterization of glia, which are poorly understood, and disease-specific alterations in neuron morphology.

Chapter 5 discusses future directions of this work, including: i. alternate characterizations of branch lengths and labeling schemes, ii. numerical analysis of the model, and iii. further studies of morphological changes across time and stages of development. Appendices A, B, and C expand upon the calculations and analysis discussed in the previous chapters, as well as highlighting topics that were explored but the results were inconclusive, providing potential avenues for future investigation. Appendix D details the data sources used in this work.

CHAPTER 2

How Axon and Dendrite Branching Are Guided by Time, Energy, and Spatial Constraints

2.1 Introduction

Neurons are fundamental structural units of information processing and communication in animals. They are made up of a centralized cell body, called the soma, and two types of extending processes, axons and dendrites. These processes transfer information between cells in the form of electrical and chemical signals. Axons generally conduct signals from the cell body to the synapses, where they connect with the dendrites of other neurons. These dendrites generally conduct signals from the synapse to the cell body. The processes form synaptic connections with one another in complex patterns. Different types of cells exhibit diverse morphological forms - some neurons have no axons or dendrites, while some have long axon processes that extend over meters, and others have vast dendritic trees that branch extensively to fill two- or three-dimensional space, corresponding to the mathematical and modeling concept known as space-filling [56].

Seminal studies in neuroscience characterized morphological differences across cell types. For instance, Santiago Ramón y Cajal's "Histology of the Nervous System of Man and Vertebrates" is considered to be the founding document of neurobiology [130], consisting of detailed drawings and comparative descriptive analysis of neuron morphology across different cell types and species [24]. Modern techniques and devices have allowed for more precise quantitative measurements at the single-cell level. For example, recent work has established

quantitative morphological distinctions across different cell types, focusing on quantities such as mean dendritic length, total dendritic length, and number of branching points [46, 70].

As vast as the structural diversity is, there is an even greater diversity of functional properties [56]. Within sensory, motor, and interneurons, there are different types of neurotransmitters and receptors that affect the nature of signal processing [109]. A major future goal of neuron cell-type classification is to establish a correspondence between morphological and functional properties [130]. Here, we seek to address the question of how structural properties relate to neuron function and whether there are evolutionary driving forces that dictate how morphology is optimized by biological principles or pressures.

A promising approach to the relationship between neuron structure and function is biological scaling theory, as it has previously been applied to understand patterns in the branching structures of biological resource distribution networks. Generally, a biological property Y scales with body mass M as $Y = Y_0 M^b$, where Y_0 is a proportionality constant and b is a scaling exponent [125]. An example is metabolic rate scaling with body mass to the power 3/4, a result known as Kleiber's Law [60].

West, Brown, and Enquist (WBE) proposed that Kleiber's law and other biological scaling laws arise because biological organisms are sustained by resource distribution branching networks that are optimized to supply all parts of the body [125]. Past work on cardiovascular networks has employed WBE theory to derive scaling laws for the vessel radius and length as a result of minimizing power loss for fluid flow along with space filling in order to fuel whole organism metabolism [103]. Moreover, previous results have shown a quarter-power allometric scaling relationship between cell size and body size in a range of cell types in mammals, including neurons [104].

Single neuron cells have centralized cell bodies that are analogous to the heart and branching processes that are analogous to blood vessels. Consequently, we propose that a similar approach based on optimizing organismal function subject to biophysical constraints may be fruitful for attempting to predict and understand the branching structures of axons and

dendrites. As such, we consider biophysical properties of neurons that might play an important role in governing structure, and we use empirical imaging data to guide our evaluation of the relative importance of different functions.

One important evolutionary function of neuronal networks is the transferring of large amounts of information between brain regions in a short amount of time [64]. At the individual cell level, the varied morphological forms observed for neurons are various adaptations to basic principles such as limiting signal time delay [24]. Thus, it is important to consider conduction time as a key design principle that governs neuronal branching structures.

Indeed, foundational work by Cuntz et al. has used graph theory to quantify and study how connections among axons and dendrites determine conduction time delay. This approach focuses on the tradeoff between wiring costs and conduction time, represented as path length [36]. The results formalize the laws set forth by Ramón y Cajal, leading to a graph-theoretical algorithm that generates synthetic and biologically accurate axonal and dendritic trees [37].

Although this formalism is deeply insightful and very successful at explaining neuron structures, two key aspects are absent for optimizing Ramón y Cajal's laws: the diameter of axonal and dendritic fibers is not incorporated, and the principle of conservation of space, as set forth by Ramón y Cajal, is missing. Because axon and dendrite radius relates to resistance to the flow of electrical current, it has a profound effect on signaling speed and conduction time. The radius is thus a key structural feature governing the function of neurons. Moreover, space-filling principles constrain the possible connections, branching, and network structure of neurons. Consequently, in this paper we take a similar approach to Cuntz et al. [36, 29] except we now incorporate the dependence of conduction time on fiber radius and myelination (insulation that surrounds the fiber and facilitates signal transduction [109]), using principles set forth by Hodgkin and Rushton [52, 100], along with the principle of space-filling.

A complicating factor that creates a tradeoff is that as the speed of information processing increases, energy loss due to dissipation also increases [64]. Indeed, signaling in the brain

consumes a substantial amount of energy [12], suggesting that energy expenditure is another important factor constraining neuron structure. Previous work has shown that the relationship between metabolic rate and conduction time plays an important role in determining axon function in species across scales of body size [121]. This leads to the WBE framework, which relies on the assumption that resource distribution networks are optimized such that the energy used to transport resources is minimized [125]. This framework is applied to cardiovascular networks by minimizing power lost to dissipation in small vessels, leading to the derivation of a power law (also known as Murray's law), which states that the radius scales with an exponent of 3 in branching blood vessels [103].

Importantly, Wilfred Rall derived a similar power law for neurons. By using the assumption that the charge is conserved at branching junctions, the diameter of daughter branches and parent branches can be related by an exponent of 3/2 [93]. Rall found that this power law holds for motoneurons but not for other cell types. Because of this seminal work, many subsequent theoretical and experimental studies on the scaling of neuron branching have used Rall's law as a baseline for quantifying variation in scaling exponents by calculating departures and differences from the 3/2-value of the scaling exponent for Rall's law [51, 111]. Although there are many functional differences between cardiovascular networks and neurons, the presence of these analogous scaling laws suggests that the mathematical framework applied to branching blood vessels might be useful to apply to neurons. While energy efficiency is the primary constraining factor considered in studies of cardiovascular systems, neurons differ in that information processing and signalling is a key consideration. We use the objective function approach from biological scaling theory for cardiovascular systems as a basis and use it to construct new models and functions that incorporate characteristic properties of neurons across their vast diversity of cell types, morphologies, and physiological functions. Applying this lens to look at neurons will expand upon existing frameworks, and comparative studies might help capture more nuances in other biological systems as well.

In this paper, we show that much of the variation around Rall's law can be explained

and predicted using our approach—varying the relative importance and weighting of time versus energy and the associated biological and physical constraints to consider a host of functions that can be optimized to derive predictions for diverse morphological quantities. That is, building on biological and physical principles that constrain electrophysiological signaling and information processing in neurons, we construct a general model that predicts a suite of neuron morphologies based on which biological or physical principles are under the strongest selection. Our model includes both conduction time and energy efficiency while also incorporating additional factors such as the material costs and space-filling [24]. We make theoretical predictions for how branch radius changes across branching generation for both axons and dendrites. We compare these predictions to our empirically measured data to make conclusions about the functional basis for morphological differences observed across cell types. We also use this model to predict how conduction time delay in neurons changes with neuron size, another of our predictions that is supported by empirical data. We use data collected from light and electron microscopy. These data collected by different methods yield extremely consistent results, strengthening support for our general model as a basis to predict neuron morphology.

2.2 Theory

2.2.1 Model

Because conduction time delay and power usage are fundamental and costly for information processing in neurons, we develop a mathematical objective function to jointly minimize time and power that is subject to constraints [19]. By deriving the minimization conditions, we predict how biological principles and constraints govern neuronal structure, as achieved via evolutionary pressures and developmental processes that shape branching networks and materials, such as myelination. Our work differs substantially from work on the cardiovascular system that does not consider effects of conduction time delay, as the physiology and func-

tion of neurons conducting currents differ in essential ways from blood vessels transporting blood. As a consequence, we also obtain different scaling relations than for the cardiovascular system. Here, we obtain a suite of predictions based on the details of the particular type of neuron such as functional differences and myelination.

Equation 2.1 is a general form of our objective function. The biophysical constraints are represented as functions and added to the expressions to be minimized, allowing us to use the method of undetermined Lagrange multipliers to optimize this overall objective function.

$$F = \alpha P_{TOT} + (1-\alpha) T_{TOT} + \sum_{i}^{N} \lambda_i f_i(r_k, l_k, k, n, m_c, d) \tag{2.1}$$

Here, P_{TOT} is the power lost due to dissipation and T_{TOT} is the time delay for a signal travelling across the network. The parameter α can be varied to consider the tradeoff between these two principles in governing the structure of different cell types. The functions f_i represent biophysical constraint functions that generically depend on the branch radius r_k and the branch length l_k, where k is the branching generation of the network (with 0 being the trunk and N being the tips). This function also depends on the total number of branching levels N of a neuron process, the branching ratio n, the mass of the cell m_c, and the dimension d of space into which the neuron processes project. The branching ratio, n, is equal to 2 for a bifurcating network, though it may vary in general. We use optimization methods to calculate scaling relationships between the radius of successive branches, $\frac{r_{k+1}}{r_k}$, as shown in Figure 2.1.

In Equation 2.1, the first term is the power loss due to dissipation, given by $P_{TOT} = \sum_{k=0}^{N} \frac{l_k}{r_k^2 n^k}$. For a neuronal network, we define the power loss by the equation, $P = I_0^2 R_{net}$, where I_0 is the ionic current and R_{net} is the resistance to current flow in the network. Because we are focusing on average, large scale quantities across the full extent of the neuron and need to consider a coarse-grained average of signal propagation, we can reasonably approximate axons and dendrites as wires through which current flows and encounters resistance from

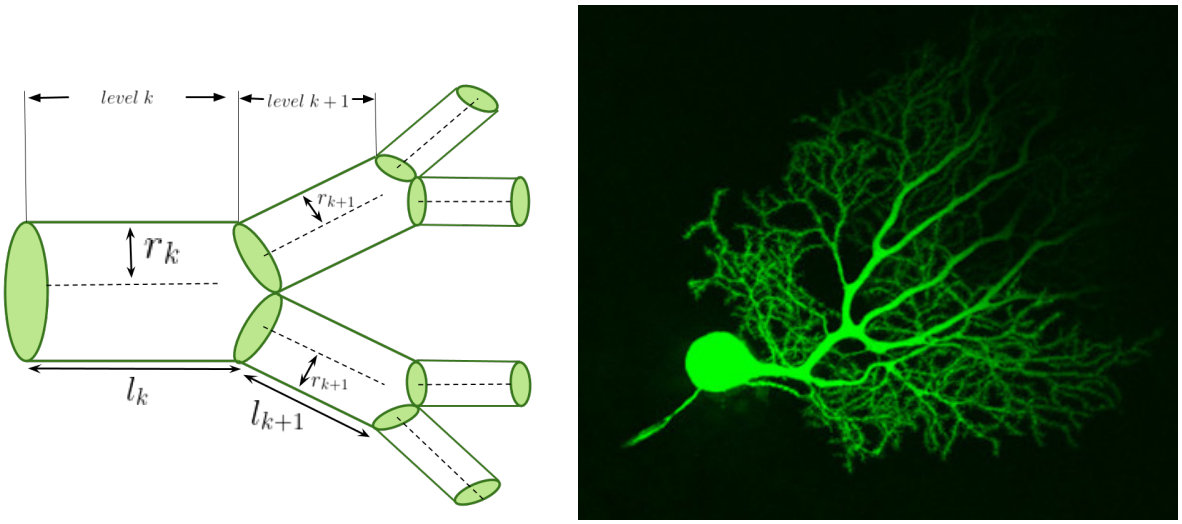

Figure 2.1. A hierarchical branching network A visual depiction of the successive branching levels of a network and the quantities of interest alongside an image of a mouse cerebellar Purkinje neuron and its dendritic branching structure. This image was obtained using confocal microscopy and Lucifer yellow fluorescent dye. We have cropped this image available on CellImageLibrary.Org, distributed by Maryann Martone, Diana Price, and Andrea Thor [74].

the neuron fiber. The resistance is given by $R_k = \frac{\rho l_k}{A_k}$, where A_k is the cross sectional area of the wire, and l_k is the length of the segment at that level. The parameter ρ is the intrinsic resistivity of the axon or dendrite, and we assume that ρ is constant, meaning that the material is uniform [56]. Approximating axons and dendrites as cylinders, the cross-sectional area is πr_k^2 for level k, and the resistance is $R_k = \frac{\rho l_k}{\pi r_k^2}$. Following standard practice, we have absorbed all physical constants into the Lagrange constants, and the magnitude of these terms do not affect the theoretical predictions.

The second term represents conduction time delay, $T_{TOT} = \sum_{k=0}^{N} \frac{l_k}{r_k^{\frac{1}{2}+\epsilon}}$, and arises because the average velocity of a signal along a single branch is $\bar{v} = l_k/t_k$, where t_k is the time delay. We can solve this expression for t_k and sum $\frac{1}{\bar{v}}$ over the length of each branch [97]. At each generation, we consider a single branch to denote the total path length of a signal, and we calculate the total conduction time delay by summing the time delays for single branches

across all N generations. The parameter ϵ describes the degree of myelination. Previous work has shown that the conduction speed is proportional to the square root of the diameter for an unmyelinated fiber [52], and directly proportional to the diameter for a myelinated fiber [100]. Thus, an ϵ value of 0 corresponds to an unmyelinated fiber, and a value of $\frac{1}{2}$ corresponds to a myelinated fiber.

Notably, we include linear terms for P_{TOT} and T_{TOT}, consistent with approaches for other systems in physics and economics. Because our quantities are always positive based on their biological interpretation, minimizing these terms and the overall functions effectively minimizes all monotonic transformations such as positive powers or logarithms of the function. Consequently, our predicted minima and scaling ratios actually hold for a broad range of functional forms (in the same way that maximum likelihood and maximum entropy calculations minimize the logarithm of the function to also find the minimum of the linear form). In addition, many complicated nonlinear functions behave linearly near critical points and linearity is the simplest form in lieu of additional information, providing additional reasons for its use as a starting point. Future studies may expand on this baseline model to consider other mathematical forms if sound biological justification is provided for their consideration.

With this form of the objective function, we can switch between models that optimize either conduction time or power usage by varying α between 0 and 1, corresponding to the following two equations.

$$T = \sum_{k=0}^{N} \frac{l_k}{r_k^{\frac{1}{2}+\epsilon}} + \lambda \sum_{k=0}^{N} n^k r_k^2 l_k + \lambda_m m_c + \sum_{k=0}^{N} \lambda_k n^k l^d \tag{2.2}$$

$$P = \sum_{k=0}^{N} \frac{l_k}{r_k^2 n^k} + \lambda \sum_{k=0}^{N} n^k r_k^2 l_k + \lambda_m m_c + \sum_{k=0}^{N} \lambda_k n^k l^d \tag{2.3}$$

In these two equations, the governing optimization principle (first term) is constrained by brain region volume (second term), neuron size (third term), and space-filling (fourth term).

These quantities are held constant during the optimization. We can define the total volume as $\sum_{k=0}^{N} n^k \pi r_k^2 l_k$, based on the assumption that the projections are cylindrical and branches are symmetric. We absorb the constant π into the Lagrange multiplier λ. The term that describes size, m_c, is the mass of the cell. The last constraint comes from the fact that a resource distribution network must extend and branch out to reach as much of the space it fills as possible, whether it is a 2-dimensional plane or 3-dimensional volume. Each branch in a given level of the network reaches a fixed volume of cells in the space it fills, called the service volume, and the total service volume at each level is preserved. The service volumes vary in proportion to l_k^d, so the total volume is proportional to the service volumes summed across each of the branches at a given generation k, $n^k l_k^d$ [103]. Thus, this quantity is held constant as a constraint function at each level k in the N generations. We assume that the branching ratio is constant, so the number of vessels at level k is n^k.

The predictions that arise from these two functions will correspond to different cell types and processes based on differences in signaling properties. We hypothesize that the principle of power loss due to dissipation will be favored in determining the structure of processes that rely on passive electronic spread, such as dendrites, while the principle of conduction time delay will be favored in determining the structure of processes that are electrically active and conduct action potentials, such as axons. The power term describes the attenuation of a signal depending on the internal resistivity of the process. For processes that conduct action potentials, the time delay term is a more useful descriptor, as it accounts for signaling not limited to passive attenuation and considers differences observed in myelinated and unmyelinated fibers. Through the tradeoff between these principles, our general model accounts for both types of signaling.

Furthermore, we note that the energetic cost of maintaining the resting membrane potential is already captured in the constraint for the total network volume. This is crucial when considering energy consumption in neurons because a large component is involved in maintaining the resting membrane potential that goes beyond energy loss to dissipation [12].

This resting membrane potential depends on the energy required by the sodium-potassium pump, which increases with surface area of the neuron [12]. Increasing surface area corresponds to an increase in volume if we assume that myelination has minimal affects on the total surface area (see Section 2.5), so that energy consumption is a per-volume quantity [121].

Crucially and somewhat surprisingly, the space-filling constraint does not change any of our predictions for radius scaling ratios. However, space-filling does play a crucial role in determining how neuron size scales with body size across species, as well as the predictions for length scaling ratios, $\frac{l_{k+1}}{l_k}$, as shown in Appendix A. Notably, we do not compare these predictions to empirical length scaling ratios here because that would likely require the introduction and usage of an alternative labeling scheme like the Horton-Strahler method as opposed to the generational labeling scheme for branch radius throughout the rest of this paper (see Section 2.5). As such, we leave that construction and analysis to future work in which we will delve deeper into asymmetric branching and alternative labeling schemes.

In Section 2.2.3, we show that minimizing power subject to a conduction time delay constraint leads to a $\frac{1}{4}$-power scaling between conduction time delay and neuron size. This objective function can be described by the following equation:

$$P^* = \sum_{k=0}^{N} \frac{l_k}{r_k^2 n^k} + \lambda \sum_{k=0}^{N} \frac{l_k}{r_k^{\frac{1}{2}+\epsilon}} + \lambda_m m_c + \sum_{k=0}^{N} \lambda_k n^k l^d \tag{2.4}$$

Equations 2.2, 2.3, and 2.4 are all specific cases of the more general Equation 1, with varying values of α as well as choice of constraint functions.

2.2.2 Scaling Ratio Calculation

We use the method of Lagrange multipliers to solve for the values of the scaling ratios for radius, $\frac{r_{k+1}}{r_k}$ that minimize the objective function. Below, we show a sample calculation of

the method of Lagrange multipliers for the case of power minimization (Eq. 2.3). A more detailed calculation can be found in Section A.1.

We will first minimize P by differentiating with respect to radius at an arbitrary level k and setting the result equal to 0.

$$\frac{\partial P}{\partial r_k} = \frac{-2l_k}{n^k r_k^3} + 2\lambda n^k r_k l_k = 0 \tag{2.5}$$

Solving for the Lagrange multiplier, we have

$$\lambda = \frac{1}{n^{2k} r_k^4} \tag{2.6}$$

Using the fact that the Lagrange multiplier is a constant and thus the denominator must be constant across levels, we can solve for the scaling ratio

$$\frac{r_{k+1}}{r_k} = n^{-1/2} \tag{2.7}$$

This method is used to solve for the scaling ratios for radius for the other cases and compared to empirical results. These findings are summarized in Table 1 in the Results section.

To ease comparison with previous work, we first note that the convention in neuroscience is to quantify changes in branching radius by using the following equation that relates the diameter of a parent branch to the two daughter branches:

$$d_0^\eta = d_1^\eta + d_2^\eta \tag{2.8}$$

We next note that much existing work presents results as a measure of departure from the baseline of Rall's law, corresponding to $\eta = \frac{3}{2}$ [93].

Conveniently, for symmetrically branching networks, there is a simple correspondence between this conventional formulation, focusing on scaling exponents relative to Rall's law, and our model, focusing on radius scaling ratios

$$\frac{r_{k+1}}{r_k} = n^{-1/\eta} \tag{2.9}$$

For example, Rall's law, $\eta = \frac{3}{2}$, corresponds to the radius scaling ratio $\frac{r_{k+1}}{r_k} = n^{-2/3}$ in our framework. This equation allows for a simple translation for us to validate our general model's various predictions due to the tradeoff of different functional principles in the context of existing results in the neuroscience literature.

2.2.3 Allometry Calculation

We now use the objective function P* (Eq. 2.4), to derive a functional scaling relationship between conduction time delay and body mass. Here, we consider conduction time delay as a constraint, focusing on the unmyelinated case ($\epsilon = 0$), and considering the case of 3-dimensional space filling ($d = 3$).

We begin by taking the derivative of P* with respect to radius and length and then setting these derivatives equal to zero to solve for the multipliers λ and λ_k, respectively, at the stationary point. Substituting the expression for λ_k back into the original expression for P^*, we get an expression that simplifies to the original power term that it minimized, $\sum_{k=0}^{N} \frac{l_k}{r_k^2 n^k}$. For simplicity, we replace the power term with P and the time delay constraint term with T and rearrange. This calculation is shown in detail in Section A.2.

Previous results have shown a proportional relationship between m_c, the mass of a single cell, and the fourth root of an animal's body mass, $M^{1/4}$, on average, though specific cell types might vary slightly from this general rule [104]. Thus, we can replace this term and consider a new Lagrange multiplier with the absorbed constant

$$P^* = 2P + \lambda T + \lambda_M M^{1/4} \tag{2.10}$$

We will now take the derivative of this term with respect to M, the mass, and set it equal to 0.

$$\frac{\partial P^*}{\partial M} = 2\frac{\partial P}{\partial M} + \lambda \frac{\partial T}{\partial M} + \lambda_M \frac{\partial M^{1/4}}{\partial M} = 0 \tag{2.11}$$

Previous results have shown that the energetic cost, which we have interpreted here as power loss due to dissipation, decreases with increasing body weight of animals at a linear rate on average for both myelinated and unmyelinated fibers, as metabolic rate is a per volume quantity [121]. Thus, we can express $\frac{\partial P}{\partial M}$ generally as a negative constant, $-C$. We can rewrite the above expression as follows

$$\frac{\partial T}{\partial M} = \frac{-\lambda_M M^{-3/4}}{4\lambda} + 2\frac{C}{\lambda} \tag{2.12}$$

Solving and applying the initial condition that T=0 when M=0, we have

$$T = \frac{-\lambda_M}{\lambda} M^{1/4} + \frac{2C}{\lambda} M \tag{2.13}$$

Thus, from this equation, we have extracted the scaling relationship - a mixed power law relationship that includes a $\frac{1}{4}$-power law and a linear term with relative weights. Figure 5 shows experimental data that support this theoretical result of the $\frac{1}{4}$-power law.

2.3 Methods

To test the theoretical predictions and model, it is important to look at empirical data for scaling ratios for radius between child and parent branches in successive levels. We analyzed

data from NeuroMorpho.Org - an online database with digital reconstructions from a wide range of species [10]. In this dataset, we have included reconstructions from neuron images using light microscopy methods as well as electron microscopy (EM) images made available through researchers involved with recent projects such as the FlyEM project at Janelia [107, 6]. Figures 2.2, 2.3, and 2.4 show five examples of images of neuron reconstructions obtained from NeuroMorpho.Org. These reconstructions are obtained by tracing neuron image stacks obtained using various microscopic and staining techniques for in vitro neurons and slicing at regular intervals. This database provides 3D reconstruction data that are organized in text files by pixels, in files that specify a pixel ID label for each point, the x,y,z spatial coordinates, the radius of the fiber at each point, and a parent pixel ID, referring to the adjacent pixel previously labelled. The scaling ratios for radius and length can be obtained by organizing this data in terms of branches. This is accomplished by finding the pixels at which the difference between the child pixel ID and the parent pixel ID is greater than 2, which can be defined as branching points. Based on the branching points, a branch ID and parent branch ID can be assigned to each of the pixels.

The radius can be extracted from each of the branches by taking each of the radius values in each branch and averaging them by the following formula, defining each branch as branch k, where the pixels i range from 1 to N_k, and where N_k is the last pixel of each branch

$$r_k = \sum_{i=1}^{N_k} \frac{r_i}{N_k} \tag{2.14}$$

The length of each branch can be extracted by summing up the Euclidean distances between each of the points in the branch by the following formula:

$$l_k = \sum_{i=1}^{N_k} \sqrt{(x_i - x_{i-1})^2 + (y_i - y_{i-1})^2 + (z_i - z_{i-1})^2} \tag{2.15}$$

Once the radius and length of each of the branches is found, the scaling ratios are com-

puted by dividing the daughter radius by the corresponding value for the parent branch. Through this method and using the Python library matplotlib, we generate histograms to visualize the distributions. For the radius distributions, we find a large peak at $\frac{r_{k+1}}{r_k} = 1.0$, which is likely due to the resolution limit of the images. After a certain level, the radius for each of the branches is equivalent to the pixel size itself. Thus, in our distributions for radius, we focused on the data for scaling ratios that are less than 1.0. We use solid black lines to denote the mean values in the data, and error bars represent twice the Standard Error of the Mean (SEM)–the standard deviation divided by the square root of the number of data points.

We looked at neuron reconstructions from both axons and dendrites, and from a range of cell types, brain regions, and species. More detailed information about the source of each of the individual reconstructions can be found in Appendix D.

For dendrites, we looked at three different types of cells: Golgi cells, Purkinje cells, and motoneurons. The Golgi cells are from *Giraffa*, *Homo Sapiens*, *Loxodonta africana*, *Megaptera novaeangliae*, *Neofelis nebulosa*, *Pan troglodytes*, *Panthera tigris* [3], and *Mus musculus* [117]. The Purkinje cells are from *Cavia porcellus* [95], *Mus musculus* [80, 28, 81, 75], and *Rattus* [71, 75, 118]. The motoneurons are from *Danio rerio* [79, 112], *Drosophila melanogaster* [107], *Felis Catus* [35], *Mus musculus* [42], *Oryctolagus cuniculus* [110], *Rattus* [99], and *Testudines* [31]. In Figure 2, we look at the combined dendrite data for all cell types and species. In Figure 2.3, we look at the radius scaling ratios of Purkinje cells and motoneurons individually, and draw comparisons between the two.

Due to the small size of axons and the limited resolution of images, the data available on NeuroMorpho.Org are limited in scope. The data shown in Figure 2.2 was taken from the following species: *Anisoptera* [48], *Brachyura* [17], *Drosophila melanogaster* [54], *Gallus gallus domesticus* [44], and *Rattus* [73]. The neurons were taken from a range of brain regions: the midbrain, the hippocampus, the antennal lobe, the optic lobe, and the ventral nerve cord.

To study peripheral nervous system neurons, we sampled from reconstruction data that was labelled by region on NeuroMorpho.Org. This data, shown in Figure 2.4, was taken from *Drosophila melanogaster* [50, 84, 127] and *Mus musculus* [14, 65, 26, 106] and includes dendritic arborizations, sensory neurons, somatic neurons, and touch receptors.

To look at functional scaling relationships between mass and conduction time delay, we first look at data for conduction time delay in motoneurons and sensory neurons across a range of species sizes, listed in order of size: *Soricidae*, *Mus musculus*, *Rattus*, *Cavia porcellus*, *Oryctolagus cuniculus*, *Felis Catus*, *Canis lupus familiaris*, *Sus scrofa*, *Ovis aries*, *Giraffa*, and *Loxodonta africana* [40]. Using the mean conduction velocity measured in studies of each species, this conduction time delay data was calculated by estimating the animal leg length using the average body mass, and then dividing that distance by the measured velocities that vary across species. We use a log-log plot, shown in Figure 2.5, to obtain a power law relationship between body mass and conduction time, where the slope is equal to the power.

2.4 Results

We compared theoretical predictions for scaling ratios calculated from objective functions T, P, and P^* with the mean values we measure from the empirical data. Because mean values capture the average overall branching properties for axons and dendrites, the mean represents the most natural and straightforward starting point for comparing our general theory with empirical data. To further clarify our approach in the context of previous studies, most neuroscience studies focus on the *median values* of *scaling exponent* data that are *exponentially distributed*, whereas here, we focus on *scaling ratio* data with *normal* and *symmetric distributions*, thus rendering the difference between the mean and median values to be negligible. As theory is refined and additional predictions are made, other features of the distribution, such as those related to the spread, should also be measured and compared (see Section 2.5). Based on the results of these comparisons for different types of neurons and

processes, we determine the functional properties that play the greatest role in determining structure for different processes and cell types.

2.4.1 Theoretical Predictions

Using the model and the method of undetermined Lagrange multipliers as detailed above, we made theoretical predictions for functions using different values of the parameters. Table 2.1 shows the results for the various objective functions minimizing conduction time delay and power. The approximations listed are based on the simplifying assumption that the network is purely bifurcating, with a branching ratio of 2.

We consider the theoretical predictions for four objective functions. The first two objective functions are specific cases of T (Eq. 2.2) that minimize conduction time delay. We consider this function for two possible values of the parameter ϵ. The unmyelinated case corresponds to $\epsilon = 0$, whereas $\epsilon = \frac{1}{2}$ signifies the myelinated case. The second two objective functions minimize power. The objective function P (Eq. 2.3) minimizes power with the volume fixed as a constraint. The alternative objective function P^* (Eq. 2.4), is the objective function that minimizes power with the time delay fixed as a constraint. For power minimization we focused on the unmyelinated case where $\epsilon = 0$, since its predictions align most with the data from dendrites, which are typically unmyelinated. These predictions can be transformed into results comparable with existing literature using Eq. 2.9.

For all of the calculations, we considered different values of the parameter d, the dimension of space filled by the processes. A value of $d = 2$ signifies neuron processes that branch into a 2-dimensional plane, such as Purkinje cells in the cerebellum. A value of $d = 3$ signifies neuron processes that fill a 3-dimensional volume, such as motoneurons [109]. We interpreted the volume constraint as a material constraint, assuming that the processes are cylindrical for both 2- and 3-dimensional space-filling. It is interesting to note that the dimension of space filling does not affect results for radius scaling ratios. However, it does play a role in the results of the theoretical predictions for length. As in the studies of cardiovascular

Table 2.1. Results for Radius Scaling Ratio Theoretical Predictions

Biophysical Principle	Prediction	Closest Biological Match	Data Mean
Time Minimization, Unmyelinated ($T, \epsilon = 0$)	$n^{-2/5} \approx 0.76$	Peripheral Nervous System Neurons	0.76 ± 0.008
Time Minimization, Myelinated ($T, \epsilon = \frac{1}{2}$)	$n^{-1/3} \approx 0.79$	Axons	0.79 ± 0.001
Power Minimization with Fixed Volume (P)	$n^{-1/2} \approx 0.71$	Purkinje cell dendrites	0.69 ± 0.007
Power Minimization with Fixed Time Delay (P^*)	$n^{-2/3} \approx 0.63$	Motoneuron dendrites	0.64 ± 0.006

network branching, we focused on radius scaling ratios in this analysis [85]. We explain this choice further in Section 2.5.

2.4.2 Axons and Dendrites

Figure 2.2 shows histograms that illustrate the differences in distributions of radius scaling ratios for dendrites and axons, along with representative images of the morphology of these two processes. Axons generally carry signals from the cell body to the synapses, where they transfer information to the dendrites of other neurons. Dendrites have extensive, tree-like structures and generally connect with the axons of other neurons to carry signals to the cell body. The distributions observed for these scaling ratios resemble the distributions observed in scaling ratios of cardiovascular networks, with the radius scaling ratios exhibiting a normal distribution. Note that the distribution of scaling ratios for axons is normal, but we have restricted it to values between 0 and 1, eliminating the cases where the resolution limit of the images is reached and the values greater than 1, which are biologically questionable.

In this figure, we show the comparison of the mean dendrite radius scaling ratio, 0.67 ± 0.004, with theoretical predictions from the four different calculations. We find that the

dendrite radius scaling ratio mean is closest to the theoretical predictions from the objective functions minimizing power. The mean lies in between the optimal scaling ratios for function P, so $n^{-1/2} \approx 0.71$, which holds volume to be fixed, and function P^*, so $n^{-2/3} \approx 0.63$, which holds time delay to be fixed. Later, in Figure 2.3 we look at the distributions of radius scaling ratios in these Purkinje cells and motoneurons individually to compare them to the closest theoretical results. In Section 2.5, we elaborate on the implications of focusing on the means in this analysis over the spread of the distributions.

Note that the radius scaling ratio mean for axons, 0.79 ± 0.001, is significantly larger than the mean radius scaling ratio observed for dendrites, 0.67 ± 0.004. The axon scaling ratio mean in the data is closest to the theoretical prediction, $n^{-1/3} \approx 0.79$, for the objective function that minimizes time, T, for myelinated fibers, $\epsilon = \frac{1}{2}$. The next closest prediction, $n^{-2/5} \approx 0.76$, is that of the objective function that minimizes time, T for unmyelinated fibers, $\epsilon = 0$. This suggests that time minimization and myelination are important factors that determine the structure for axons.

2.4.3 Purkinje Cells and Motoneurons

One of the parameters that we built into our theoretical model is d, the dimension of space filling of the processes. Thus, we looked at the comparison of results from data from representative cells with 2-dimensional and 3-dimensional dendritic trees. For 2-dimensional dendritic trees, we looked at cerebellar Purkinje cell data from rodents including mice, rats, and guinea pigs. For 3-dimensional dendritic trees, we looked at motoneurons from a range of species including rodents, amphibians, cats, and humans. The histograms for these two cell types, along with a representative image for each type, are shown in Figure 2.3. The theoretical results of minimizing power and time cost functions while varying the parameter d does not capture the differences in radius scaling ratios observed in this data. We hypothesized that the differences observed can be explained by other principles such as the functional differences of these cell types. The mean for Purkinje cells, 0.69 ± 0.01, agrees

with the theoretical predictions for the function P, that is power minimization with a volume constraint, $n^{-1/2} \approx 0.71$, while the mean for motoneurons, 0.64 ± 0.01, agrees with the theoretical predictions for function P^*, that is power minimization with a time constraint, $n^{-2/3} \approx 0.63$.

Based on the results of the comparison of Purkinje cells and motoneurons, we concluded that volume plays a greater role in constraining the structural design of Purkinje cells, while time plays a greater role in constraining the structural design of motoneurons.

2.4.4 Peripheral Nervous System Neurons

In the Peripheral Nervous System (PNS), motoneurons play an important role in the exchange of information with sensory neurons. Peripheral nerves carry sensory information and interact with motoneurons, which directly innervate effector cells such as muscles [109]. Thus, the importance of conduction time as a constraint for motoneurons motivated us to examine data from other types of PNS neurons such as sensory neurons. Figure 2.4 shows the radius scaling distribution of a sample of the PNS neurons labeled by region on NeuroMorpho.Org. This data was taken from flies and mice. The mean radius scaling ratio, 0.76 ± 0.01, is closest to the theoretical prediction, $n^{-2/5} \approx 0.76$, for the objective function, T, that minimizes time for unmyelinated fibers, $\epsilon = 0$. This suggests that time is an important factor in optimizing structure for PNS neurons.

2.4.5 Time Delay Scaling

So far, we have focused on predictions and data combined from species of a range of sizes. Here, we consider how function varies across species of a range of body masses. We used P^*, the equation minimizing power with fixed time delay. As shown in Section 2.2.3, our theoretical calculations have led to the relationship between conduction time delay and mass described in Equation 2.13.

In order to test this theoretical result, we analyzed experimental data to determine an observed relationship between time delay as a function of species size. Previous experimental studies have looked at conduction time delay across species ranging from shrews to elephants [40]. A regression analysis of the data shows that the $\frac{1}{4}$-power mass term is more significant than the linear term, as is shown in more detail in the Appendix, in Section A.3. Furthermore, we used a log-log plot to determine the power of the relationship, plotting the log of the conduction time delay data against the log of the average body mass of each species. This plot is shown in Figure 2.5.

Our theoretical predictions suggest the presence of a $\frac{1}{4}$ (=0.25) power law that relates species mass to neuron conduction time delay. These experimental results support this power law, as the power law determined from the data is 0.30 ± 0.04. It is possible that at a wider range of masses, a scaling law closer to the linear relationship might be observed. Further data and analysis of the relationship between the size of individual neurons and processes and species mass and between conduction velocity and time delay will provide useful insight into this allometry.

2.5 Discussion

A comparative analysis of the radius scaling ratios of different processes and cell types suggests that there are selection pressures for different functional roles that underlie the diversity in neuron branching patterns. There are a number of characteristic differences observed between axons and dendrites that are maintained across species and cell size. Axons are long and function to transmit signals over large distances, sometimes between different regions of the nervous system [94]. Moreover, axons have the unique property of myelination, which provides an important role in information transfer in the nervous system [122]. Our results indicate that the radius scaling ratio mean for axons is closest to the prediction that minimizes time for conduction through myelinated fibers, which supports this notion

that information processing speed is a key principle governing the structure of axons. The predictions and results from the data for axons are supported by previous theoretical results predicting scaling laws for myelinated axons [111].

In contrast, dendritic trees are relatively short, have more extensive branching, and generally do not conduct action potentials [94]. Previous theoretical work on wiring optimization in cortical circuits similarly proposes that there are differing evolutionary selection pressures governing axons and dendrites. Rather than conduction time delay, the key principle behind dendritic structure is passive cable attenuation [30]. Our results suggest that dendrites are optimized to minimize power, which is related to a voltage drop, with a volume constraint that we have interpreted as a cost in materials. Thus, minimizing power in our theoretical framework is effectively minimizing the attenuation of the passive signals in dendrites.

There is a great deal of diversity in the branching structures of dendritic trees, and the differences in scaling ratio distributions among the different types gives us important insights into their distinct functional roles. We found that the structure of Purkinje cells and motoneurons are both governed by power minimization, and Purkinje cell structure is constrained by volume while motoneuron structure is constrained by time delay. The predictions and results from the data for Purkinje cells and motoneurons are supported by previous theoretical and experimental results [51, 123]. We conclude that time plays a greater role in optimizing the structure for motoneuron dendrites.

Efficiency in information processing is a key function of neurons in the sensorimotor system, and our results emphasize that function as a key feature governing their structural design. When organisms are exposed to environmental stimuli, it triggers a response in the motor system that must be executed very rapidly. Some of these responses are innate, and some are learned through practice, gradually increasing in speed [119]. We found that the structure of neurons in the peripheral nervous system, such as the sensory neurons that relay information from the environment to motoneurons, is governed by time minimization, which is consistent with the evolutionary function of the sensorimotor system. The correspondence

of our theoretical predictions with empirical measurements from neurons of different types supports intuitive notions about neuron computation in these specific cell types.

So far, we have looked at optimization problems minimizing power and time individually. However, it is possible that there might be intermediate values, and different cell types might have different relative importance of time and power in determining structure. A possible avenue for future work is using numerical methods to extend the number of functional principles we consider and to better estimate parameters, such as the relative importance of different functional principles and degree of myelination. This might provide a more biologically realistic estimate for scaling ratios, as it is likely that neuron cell structures are designed to optimize not only conduction speed or energy efficiency, but a relative combination of both.

Recent work has looked at data and the scaling exponents in dendrites to compare the results to Rall's law for neurons - with a 3/2 exponent to describe branching diameters - as well as exponents derived for other biological networks such as cardiovascular networks and trees. Their data show a range of exponents varying from Rall's law, and they propose that cell biological constraints related to intracellular transport and the cytoskeleton are important in determining the morphology of neurons [66]. This is supported by other recent studies that relate dendritic morphology, including measures of caliber, to cytoskeletal proteins such as microtubules and actin filaments [83, 7]. While it is likely that these are important considerations driving morphology, our general model derives scaling ratios with a range of values - depending on the tradeoff of functional principles - that agree with the median range of exponents in their data, suggesting that our framework is a promising general model that accounts for much of the observed variation around Rall's law.

The similarities in distributions of scaling ratios in radius and length between neurons and cardiovascular networks suggest that a unifying framework underlies these diverse biological systems. Moreover, our work extends previous work on biological scaling theory in resource distribution networks by considering other driving factors besides energy efficiency as well as the tradeoff between multiple functional principles. This approach and the inclusion of

additional principles has the potential to motivate future studies both in neuroscience and biological resource distribution networks.

Some features of neural systems not captured by our current model could be incorporated in future iterations. For instance, the morphology of dendritic arbors is not static but is constantly changing based on interactions with surrounding neurons and glia [109]. Moreover, we have formulated the space-filling constraint based on the idea that cardiovascular networks are optimized such that vessels feed every cell in the body. However, neurons exhibit more complex space-filling patterns due to their interactions with one another, such as tiling and self-avoidance [25, 124]. It might also be fruitful to consider different formulations of the space-filling constraints for different types of neurons. For example, axons tend to have projections that feature a longer parent branch, and the daughter branches occur further away from the soma. Indeed, previous work has extended the WBE model to look at scaling in plants [91]. Previous work on space-filling for plants such as palm trees, which have similar morphology, might help guide future studies in this direction and improve predictions, particularly for length scaling ratios.

We have chosen to focus on radius scaling ratios in this analysis because the branch length measurements are not accurately characterized, as also previously reported for vascular scaling [85]. Recent work suggests Horton-Strahler labeling — where the first level begins at the tips, and higher levels are determined when two branches of the same level combine — may yield better estimates of branch length scaling [21]. For instance, previous work on river networks has used Horton-Strahler labeling, and it has been applied to other networks in biology, particularly those in in which asymmetric branching is observed [116, 58].

Hermann Cuntz's group has also applied this ordering method to analyze dendritic trees, finding differences in branching metrics across neuron cell types [120]. In future work, we plan to investigate how this alternative labeling scheme for branch lengths compares with theoretical predictions derived using our framework. We hypothesize that applying this labeling scheme to define branching levels for length will give a distribution of scaling ratios

that looks more like the normal distributions observed for radius scaling ratios, and values for means that agree more closely with our theoretical predictions, as has been seen in work on cardiovascular networks.

Furthermore, we note that our comparison of the predictions to the data involve only the mean values. The mean provides a single, simple, cumulative, and easily interpretable measure. Other possible choices include the mode of the distributions, which would differently account for the spread or the shape of the variation of the distributions. The mean and mode values do not align in all cases. Future work should look further into additional features–such as variance or higher-order moments–of the distributions of radius and length scaling ratios in order to extract even more valuable information from the data.

Additionally, we have represented the energy consumption here as the power lost due to dissipation during signaling. In neurons, however, maintaining the resting membrane potential makes up a significant fraction of the energetic costs. Here, we assumed that this cost is captured in the volume term in the model. However, it might be possible to more explicitly formalize the inclusion of the resting potential via the incorporation of additional factors that affect this cost. For example, myelination affects the surface area as well as the capacitance of axons, and the energy required to maintain the resting potential varies linearly with capacitance [121]. Incorporating these complexities in our model might improve its biological accuracy and usefulness when comparing predictions to empirical data from neurons.

Throughout this model, we have assumed that branching is symmetric - the radius and length of daughter branches are identical. Previous work has attempted to capture asymmetry in cardiovascular networks and plants [22]. Another major goal of our future work is to apply this theoretical framework to look at branching of neuron processes and to use branching properties related to asymmetry to compare different cell types. *This will be pursued in Chapter 3 of this dissertation.*

Beyond the scaling ratios for successive branches in the individual neuron processes,

it is interesting to consider allometric scaling relationships of species size and functional properties that vary with size. Previous work on cardiovascular networks has extracted an allometric scaling relationship that relates species size (or mass) with network volume [103], and other previous work on scaling has shown an allometric scaling relationship between single cell neurons and animal body mass [104]. In addition, when brains grow in size, they require more extensive axonal trees to traverse greater distances [16]. Building on these ideas from our theoretical formulation of the objective function that minimizes power subject to the constraint of fixed conduction time delay, we were able to extract a functional scaling relationship between species size and time delay for unmyelinated fibers. We derived that there is a mixed power law relationship between animal body mass and conduction time delay, including both a term with a $\frac{1}{4}$-power and a linear term with mass. The dominance of the $\frac{1}{4}$-power law is supported by experimental data of conduction time delay from species of a range of masses: the conduction time delay scales with the fourth root of the animal body mass.

An interesting aspect of this result is that neurons in larger animals have longer conduction delays. These results are important to consider in the context of evolution - longer delays might provide a functional explanation for the increased specialization of brain function hemispheres. Due to the greater conduction time delays, it might be advantageous for larger brains to exhibit more specialization and to organize cells with information about related memories and skills in localized clusters [97], thus improving the efficiency of information processing.

2.5.1 Conclusion

We conclude that neuron function places profound constraints on neuron morphology, thus cementing the foundations in Ramón y Cajal's work [24] and resulting theoretical and computational formalism by Cuntz and Chklovskii [36, 30]. We extend this work to include metabolic constraints and to consider the volumetric aspect of morphology. Our approach

provides a framework to measure and quantify neuron morphology, and a mathematically and theoretically advanced way to describe the influence of biophysical constraints in selecting morphological patterns in neurons. Combining empirical measures with our theoretical predictions, we showed fundamental differences between axons and dendrites and between Purkinje cells and motoneurons that are connected to the myelination of axons and the dimension of space being filled by the branching processes. Our results are consistent with and supportive of the hypothesis that the tradeoff between these functional principles governs neuronal branching and structure, and therefore accounts for the variation in scaling laws observed in recent studies [66]. Future work will shed even more light on these foundational questions by building models to capture more biological complexity and by obtaining larger amounts of data at higher resolutions across more species and more cell types. Indeed, looking across species and cell types will also help reveal further differences in neuronal function and tradeoffs among different principles that may transform how we understand the function and form of the brain.

Chapter 2 is taken from a published work by the dissertation author, ***Paheli Desai-Chowdhry****, Alexander B Brummer, and Van M Savage. "How axon and dendrite branching are guided by time, energy, and spatial constraints." In:* Scientific Reports *12, 20810 (2022). https://doi.org/10.1038/s41598-022-24813-2 [38], with minor changes to the figure captions.*

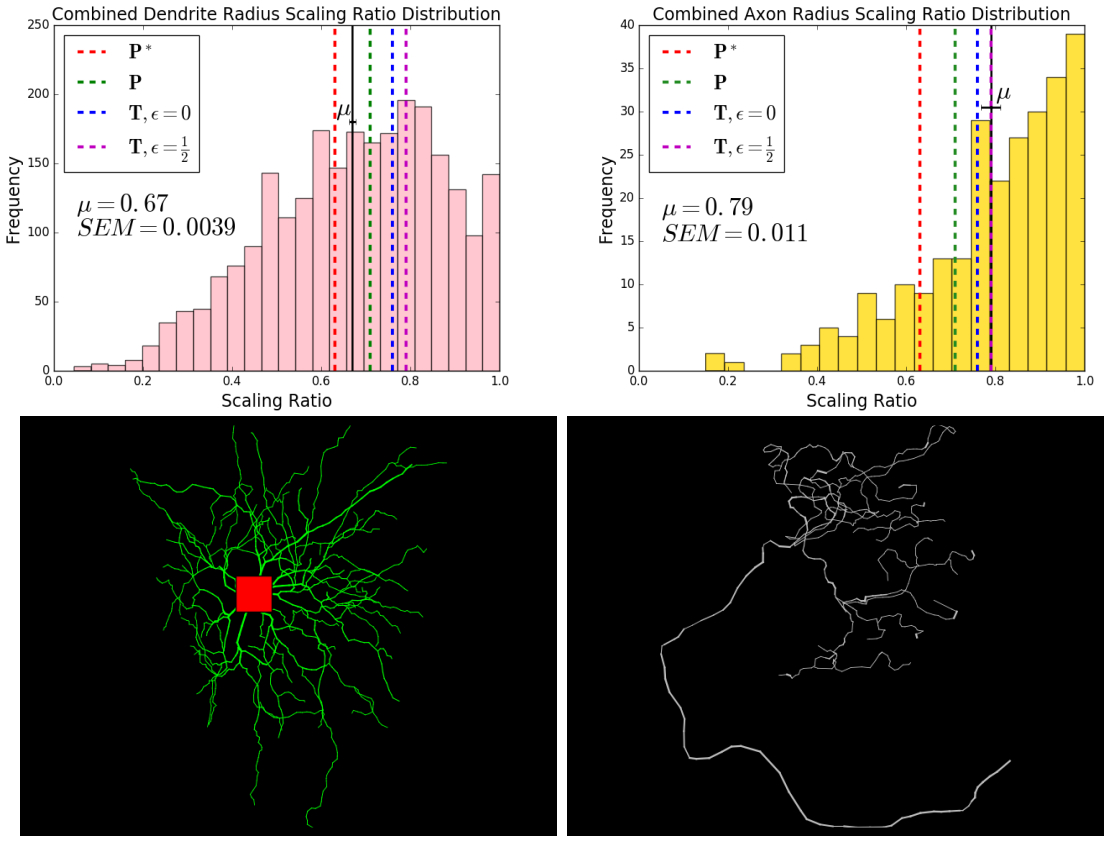

Figure 2.2. Comparison of Dendrite and Axon Radius Scaling Ratio Distributions, Combined Histograms showing the distributions of radius scaling ratios for axons and dendrites combined from a range of species, brain regions, and cell types available on NeuroMorpho.Org. In the figure, μ represents the mean and SEM represents the standard error of the mean (SEM). The standard deviations of the distributions are 0.20 for dendrites and 0.17 for axons. The black solid lines denote the mean in the distributions, shown with error bars, and the red, green, blue, and magenta dashed lines represent the theoretical predictions for various objective functions. We restricted radius scaling ratio data to values that are less than 1.0. The representative reconstruction images show the characteristic differences in morphology between dendritic and axonal trees. The dendritic tree, shown on the left, is taken from an elephant cerebellar Golgi cell [3]. The axonal tree, with a representative long parent branch, is taken from a mouse touch receptor [65].

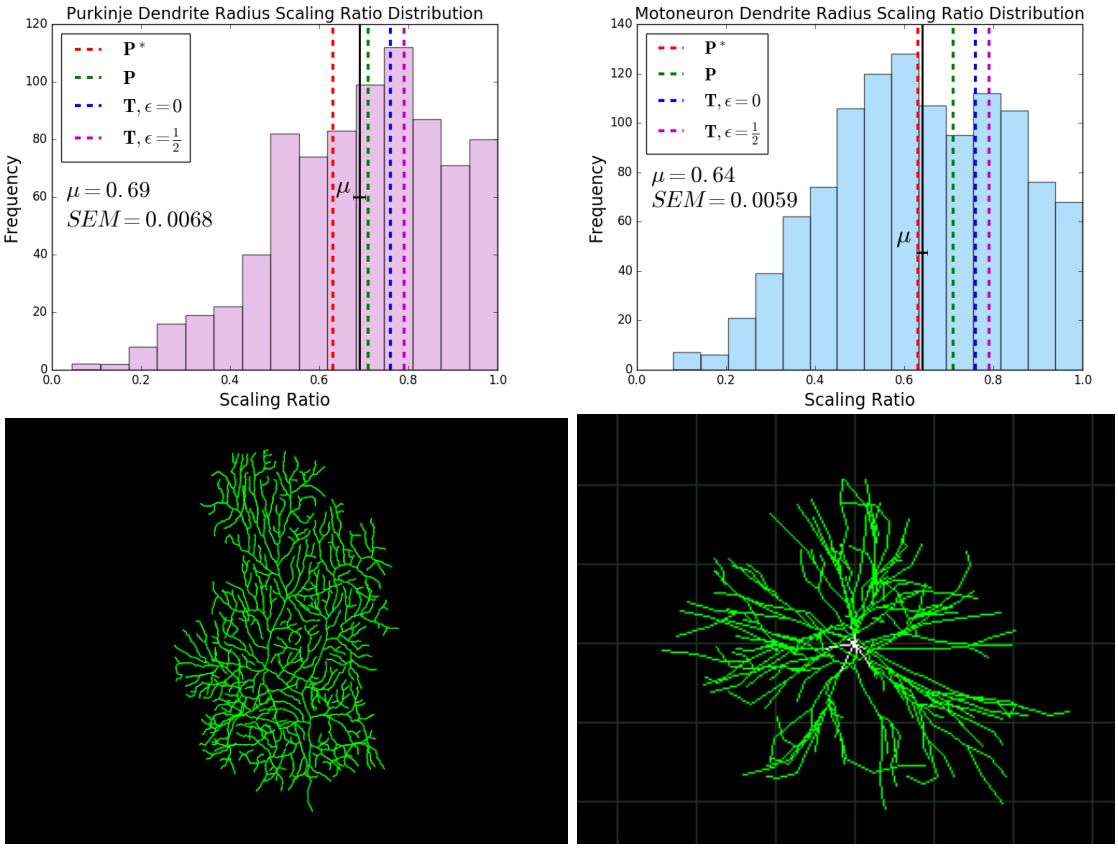

Figure 2.3. Comparison of Radius Scaling Ratio Distributions of Cerebellar Purkinje Cell and Motoneuron Dendrites A comparison of histograms showing the distribution of radius scaling ratios observed in dendrites of Purkinje cells and motoneurons, along with representative images. In the figure, μ represents the mean and SEM represents the standard error of the mean. The standard deviations of the distributions are 0.19 for Purkinje Cells and 0.20 for motoneurons. We have restricted radius scaling ratio data to values that are less than 1.0. The black solid lines denote the mean values in the distributions, shown with error bars, and the red, green, blue, and magenta dashed lines represent the theoretical predictions for various objective functions. The representative image for the Purkinje cell is from a mouse [81] and the representative image for the motoneuron is from a cat spinal motoneuron [35].

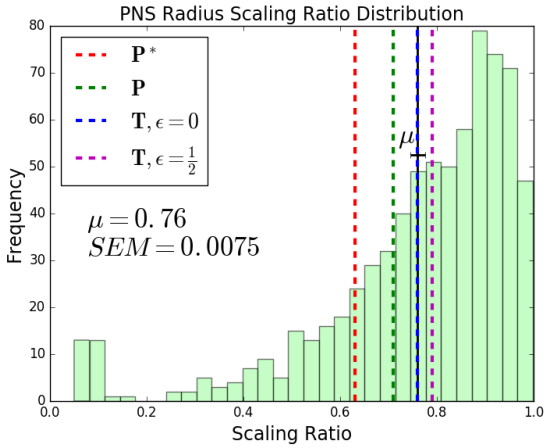

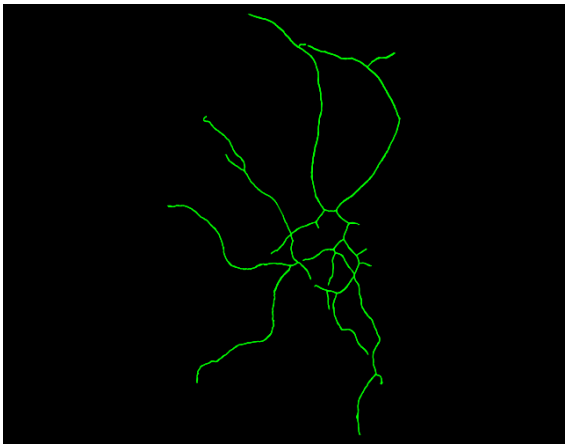

Figure 2.4. Peripheral Nervous System Neurons A histogram showing the distribution of radius scaling ratios in Peripheral Nervous System (PNS) neurons, along with a representative image of the dendritic tree of a mouse sensory neuron [106]. In the figure, μ represents the mean and SEM represents the standard error of the mean. The standard deviation of the distribution is 0.20. We have restricted radius scaling ratio data to values that are less than 1.0. The black solid lines denote the mean in the distributions, shown with error bars, and the red, green, blue, and magenta dashed lines represent the theoretical predictions for various objective functions.

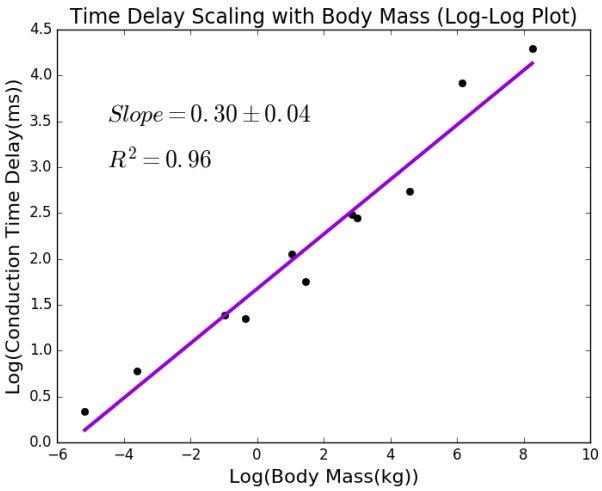

Figure 2.5. Scaling of Conduction Time Delay and Species Mass A scatter plot showing the relationship between the log of the conduction time delay and the log of the body mass of a range of species. Here, the slope, 0.30 ± 0.04, corresponds to the power that relates species mass to conduction time delay. This is close to our theoretical result of $\frac{1}{4}$ (=0.25).

CHAPTER 3

Neuronal Branching is Increasingly Asymmetric Near Synapses, Potentially Enabling Plasticity While Minimizing Energy Dissipation and Conduction Time

3.1 Introduction

The concept of asymmetry lies at the core of many biological processes, particularly in the nervous system, from asymmetries at the molecular level to whole-brain asymmetries. At the molecular level, asymmetry underlies the electrical and chemical transmission that enables information processing in the brain. Neurons connect to one another through axons and dendrites at synapses, where inter-cellular channels allow the transmission of signaling molecules, or neurotransmitters, and the spread of electrical currents. The asymmetry of these channels at the molecular level leads to functional asymmetry of the synapses, which is a key property enabling sensory processes [41]. At the cellular level, polarity and the asymmetric organization of cellular component is vital to many processes such as cell migration, cell division, and morphogenisis [55]. Asymmetry in neurons in particular has an important role in determining the physiology of neural circuits and cognition [33].

At the whole brain level, a key feature and an important topic in the study of the human brain is its division into hemispheres. The asymmetry between the left and right specialized regions of the human brain is crucial in our understanding of its structural organization and cognitive functions; many cognitive and psychiatric disorders are linked to specific alterations

in this lateral hemispheric asymmetry [62]. Hemispheric asymmetries have been observed not only in humans, but in a range of species–including mammals, birds, reptiles, and fish– suggesting that lateral asymmetry is not unique to humans but rather an important principle in the structure and function of the nervous system [86].

In order to begin to understand broad-level asymmetries in the human brain, it is important to begin with the basic building blocks of the nervous system: neurons [101]. Neurons are said to be one of the most polarized cells in the body, with two distinct structural and functional domains— axons and dendrites [15]. A deeper understanding of the details of the structure and function of these neurites and how they respond to developmental and environmental cues to form synaptic connections is a crucial step leading up to an understanding of whole-brain asymmetry, cognition, behavior, and how alterations lead to diseased states [101].

Axons and dendrites form extensive branching trees that allow them to connect to one another, enabling information processing and communication in animals. Axons and dendrites are morphologically and functionally distinct; axons have long parent branches that can transmit information across large distances, and dendrites have shorter branches with more extensive branching trees. Axons utilize action potentials to transmit information over long distances, sometimes even crossing brain regions. The branching patterns and asymmetries of axons are characterized by systematic changes in branching radius and length across bifurcation branching points and are known to play a key role in signal propagation dynamics in neurons [87]. These axons connect to the dendrites of other neurons, which in contrast, rely on passive electronic spread and do not conduct action potentials [94]. Axons and dendrites have different mechanisms for forming new branches near their synaptic connections, allowing them to form the circuitry that is the backbone of information flow in the nervous system in the most efficient and frugal way[115, 64]. Foundational work by Santiago Ramón y Cajal documented the vast diversity of structural forms in neurons through detailed drawings of the morphology of neurons across cell-types. Ramón y Cajal established

the correspondence between these diverse morphological forms and the vast functional diversity across cell-types by proposing functional principles that govern the structure such as conservation of space, time, and materials [24].

Previous work has attempted to develop a quantitative formalism to describe neurite branching through the laws of conservation of time and materials as described by Ramón y Cajal, using principles of optimization and a graph theoretical algorithm to generate biologically realistic synthetic axonal and dendritic trees [36, 29]. While this framework is able to successfully generate biologically accurate branching trees, it is limited in that it only considers the lengths of branching processes. Focusing on the 1-dimensional trace of these structures only captures one element of the biological factors that affect information processing speed, thus ignoring other important contributors. Foundational work by Hodgkin and Rushton describes the theoretical and empirical foundation for a quantitative description of the dependence of conduction velocity on the caliber of neurites as well as myelination [52, 100]. Our previous work incorporates volumetric interpretations of conduction time delay and material costs using mathematical principles from metabolic scaling theory in relation to cardiovascular networks to incorporate metabolic costs. Synthesizing these ideas leads to a unifying model that can predict various morphological structural parameters for axons and dendrites across a range of cell types [38].

We observe significant deviations from symmetric branching in neuron morphology data, as previewed in Figure 3.1 (D), suggesting that asymmetric branching is an important feature for the structure of neurons, likely corresponding to functional consequences as well. Although foundational work in modeling cardiovascular networks assumes that the branching junctions have perfect symmetry of the two daughter branches [125, 103], in biological resource distribution networks there is substantial variation around this symmetric case. Zamir first quantified deviations around symmetric branching that occur in vessels, showing differing levels of asymmetry across levels of coronary arteries [129, 128]. Further work by Tekin et al. built on this to establish systematic patterns in asymmetry throughout cardio-

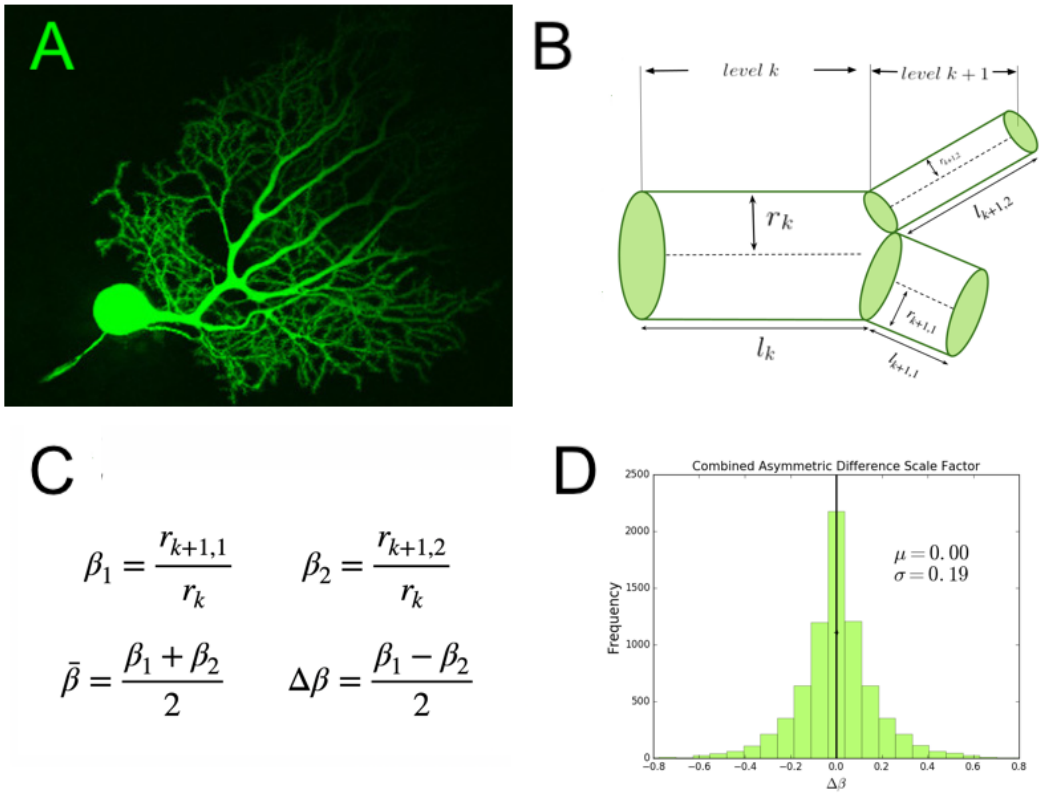

Figure 3.1. (A) An image of a mouse cerebellar Purkinje neuron and its dendritic branching structure. This image was obtained using confocal microscopy and Lucifer yellow fluorescent dye. We have cropped this image available on CellImageLibrary.Org, distributed by Maryann Martone, Diana Price, and Andrea Thor [74] (B) A diagram of a branching junction as part of a hierarchical branching network with successive branching levels, illustrating asymmetric branching junctions (C) Definitions of asymmetric scale factors, β_1 and β_2, and average and difference scale factors, $\bar{\beta}$ and $\Delta\beta$, (D) A quantification of the branching asymmetry present across all data analyzed, as measured by the difference scale factor, $\Delta\beta$, where the most symmetric values lie at a value of 0.

vascular networks, adding to the analysis of asymmetry in branching length and width to incorporate patterns of asymmetry in branching angles [114], as well as deriving optimization principles that underlie these patterns.

In order to understand the role of asymmetric branching in neuronal function across cell-types, here we extend our model of the structure-function correspondence to incorporate asymmetric branching. Using the asymmetric branching approach to model neurons, we must consider a multitude of path lengths from the soma to the synapses, suggesting that the whole network–rather than one optimal path–has an important contribution to neuron function and computation. Our results allow us to formulate hypotheses about the connection between branching and plasticity. In particular, our results suggest that it is possible that asymmetric branching emerges due to plasticity and responses to external factor. We hypothesize that asymmetric branching provides these dynamic branching processes with a robust architecture that is resilient to damage and allows them to adapt to fluctuating environments.

3.2 Theory

We represent neurons as hierarchically branching information processing networks, with successive branching levels that decrease in radius and length according to a scaling (i.e., power law) relationship. Figure 3.1 illustrates this with a representative image and a diagram of a branching junction.

We predict how the information processing function and surrounding substrate govern the branching structure of neurons. We do this by optimizing a mathematical cost function subject to a set of constraints, which allows us to obtain theoretical predictions for structural parameters that are the best possible given the biological constraints of the physical system [19]. Here, we choose a cost function that minimizes conduction time delay and energy consumption (represented by power loss) that is subject to computational, biological, and physical constraints.

$$C = \alpha P + (1 - \alpha)T + \sum_i \lambda_i f_i(r_k, l_k, k, N, n, \epsilon) \tag{3.1}$$

Equation 3.1 is a general form of this equation, where T is conduction time delay and P is power loss due to dissipation based on the assumption that these neuron processes are like wires through which a current is flowing, subject to electrical ohmic resistance. The parameter α can be toggled between 0 and 1 to minimize either power or time alone. The remaining terms in this function are constraint functions, representing biological quantities such as material costs that are held constant during the optimization. Each term in the cost function depends on the radius and length of the branch at each branching generation k, where 0 is the branching generation at the parent branch connected directly with the soma, and N is the last branching generation at the tips. The constraint functions f_i depend on the radius and length, r_k and l_k, the branching ratio n (where n = 2 for a bifurcating function), and a parameter describing myelination, ϵ, where $\epsilon = 0$ for unmyelinated fibers and $\epsilon = \frac{1}{2}$ for myelinated fibers. We chose this parameter to vary this way because of previous foundational experimental and theoretical work that shows the conduction velocity is proportional to the square root of the diameter of a neuron fiber for unmyelinated processes and directly proportional to the diameter for myelinated fibers [52, 100]. Here, we focus on two main constraints: a material constraint, which we represent as the total network volume, and a time delay constraint, which we consider for the specific cases that focus on power minimization.

In our previous work, we use optimization methods to solve for theoretical predictions for scaling ratios for radius and length of processes in successive branching generations, $\beta = \frac{r_{k+1}}{r_k}$ and $\gamma = \frac{l_{k+1}}{l_k}$ [38]. However, a key assumption of this work is that the branches are symmetric—the radius and length of the two daughter branches at each branching junction are identical. Despite this assumption, most biological axons and dendrites exhibit asymmetric branching [87, 43]. By analyzing neuron image reconstruction data from NeuroMorpho.Org [10], we quantify the pervasiveness of asymmetric branching across different cell types, as

shown in Figure 3.1 (D).

In Figure 3.1 (B), we show an example of asymmetric branching. Here, we have two unequal daughter branches at the bifurcation point, so there are two separate scaling ratios for radius and length, $\beta_{k,1} = \frac{r_{k+1,1}}{r_k}$ and $\beta_{k,2} = \frac{r_{k+1,2}}{r_k}$ (shown in Figure 3.1 (C)), and $\gamma_{k,1} = \frac{l_{k+1,1}}{l_k}$ and $\gamma_{k,2} = \frac{l_{k+1,2}}{l_k}$, respectively.

We define the average scale factor as $\bar{\beta} = \frac{\beta_1+\beta_2}{2}$ and the difference scale factor as $\Delta\beta = \frac{\beta_1-\beta_2}{2}$ (shown in Figure 3.1 (C)) based on conventions in previous work [22]. If we define β_1 as the scaling ratio corresponding to the larger branch, we can describe β_1 and β_2 in terms of the average and absolute value difference scale factors as in Equation 3.2.

$$\beta_1 = \bar{\beta} + |\Delta\beta|; \beta_2 = \bar{\beta} - |\Delta\beta| \tag{3.2}$$

Thus, we can think of $|\Delta\beta|$ as a measure of the magnitude of the asymmetry, or the amount of shift away from the average. Figure 3.1 (D) shows a distribution of $\Delta\beta$ in combined data for a range of cell types and species, preserving the sign as well as the magnitude to show variance around the symmetric case in both directions. We later break this data down into specific cell and process types in Figure 3.3.

Using an existing mathematical framework for asymmetric branching networks in the cardiovascular system [22], we extend our previous model [38] and are able to relax the assumption of symmetric branching. Using the scaling ratios in our expressions for power, time, and network volume along with the values for the radius and length at the tips, we derive whole network properties. As compared with our previous work, we needed to develop much more clever mathematical methods and do much more extensive derivations than for the symmetric theory. A big advance in overcoming these challenges is that we solve these equations recursively (See Appendix B).

First, we define power, one of the functions to be minimized in the optimization, in terms of the asymmetric scale factors.

$$P = R_{N,TOT} \sum_{k=0}^{N} \left(\prod_{j=k}^{N-1} \left[\frac{\beta_{j,1}^2}{\gamma_{j,1}} + \frac{\beta_{j,2}^2}{\gamma_{j,2}} \right] \right) \tag{3.3}$$

Note that we can also formulate this in terms of the difference and absolute value difference scale factors, where $\beta_{j,1}^2 = \bar{\beta} + |\Delta\beta|$ and $\beta_{j,2}^2 = \bar{\beta} - |\Delta\beta|$.

The other function to be minimized in the optimization is the conduction time delay. This term is more complicated with asymmetric branching, as there are multiple possible paths that a signal might take through the network. Previous work on plant networks deals with deviations from symmetry using a combination of terms relating to the mean and maximum path lengths [108]. Thus, we consider different cases of time delay: average time, total time, maximum time, and minimum time.

We define total time delay as follows in Equation 3.4.

$$T_{TOT} = T_{N,TOT} \sum_{k=0}^{N} \left(\prod_{j=k}^{N-1} \left[\frac{\gamma_{j,1}}{\beta_{j,1}^{\frac{1}{2}+\epsilon}} + \frac{\gamma_{j,2}}{\beta_{j,2}^{\frac{1}{2}+\epsilon}} \right]^{-1} \right) \tag{3.4}$$

The average time delay is similar, though the total time at each generation is divided by the number of branches at that generation.

$$\bar{T} = T_{N,TOT} \sum_{k=0}^{N} \frac{1}{2^k} \left(\prod_{j=k}^{N-1} \left[\frac{\gamma_{j,1}}{\beta_{j,1}^{\frac{1}{2}+\epsilon}} + \frac{\gamma_{j,2}}{\beta_{j,2}^{\frac{1}{2}+\epsilon}} \right]^{-1} \right) \tag{3.5}$$

Finally, we define the time delay for the maximum and minimum path length. If we choose $r_{k+1,1}$ to be the larger daughter radius (Figure 3.1 (B)), then we can define the maximum path length.

$$T_{MAX} = T_{N,TOT} \sum_{k=0}^{N} \left(\prod_{j=k}^{N-1} \left[\frac{\beta_{j,1}^{\frac{1}{2}+\epsilon}}{\gamma_{j,1}} \right] \right) \tag{3.6}$$

Similarly, we can define the minimum path length.

$$T_{MIN} = T_{N,TOT} \sum_{k=0}^{N} \left(\prod_{j=k}^{N-1} \left[\frac{\beta_{j,2}^{\frac{1}{2}+\epsilon}}{\gamma_{j,2}} \right] \right) \tag{3.7}$$

Next, we define the network volume or material cost— one of the constraint functions to be held fixed in the optimization.

$$V = V_{N,TOT} \sum_{k=0}^{N} \left(\prod_{j=k}^{N-1} \left[\frac{\beta_{j,1}^{2}}{\gamma_{j,1}} + \frac{\beta_{j,2}^{2}}{\gamma_{j,2}} \right]^{-1} \right) \tag{3.8}$$

In this study, we will minimize the cost function in equation 2.1 under different limits to arrive at a suite of relationships between the two scaling ratios, β_1 and β_2, based on a scaling exponent P that dictates a generalized conservation equation:

$$1 = \beta_1^P + \beta_2^P \tag{3.9}$$

Although the distribution of scaling exponents yields information about broad network behavior, we first focus on how asymmetry changes with the distance from the soma. If we find that the asymmetry is localized to specific parts of the cell, this could be due to differences in the functional underpinnings that drive structures in different regions of the cell or due to other extrinsic factors such as connecting neurons or due to environmental cues. In order to analyze the data in terms of distance from the soma, we can use an established measure called leaf number that has been used to study scaling in dendritic branching [66]. The leaf number is defined as the number of tips that are distal to each branch. The leaf number at the tips will be equal to 0, and the leaf number will be greatest near the soma. Figure 3.2 illustrates leaf numbering. For each pair of radius scaling ratios in the data, we have a corresponding leaf number of the parent branch of the junction. We can define asymmetry level in terms of the difference between β_1 and β_2, or the difference scale factor in Equation 3.2. Distributions of this difference scale factor for different cell types are shown in Figure 3.3. Looking at the relationship between leaf number and this measure of asymmetry

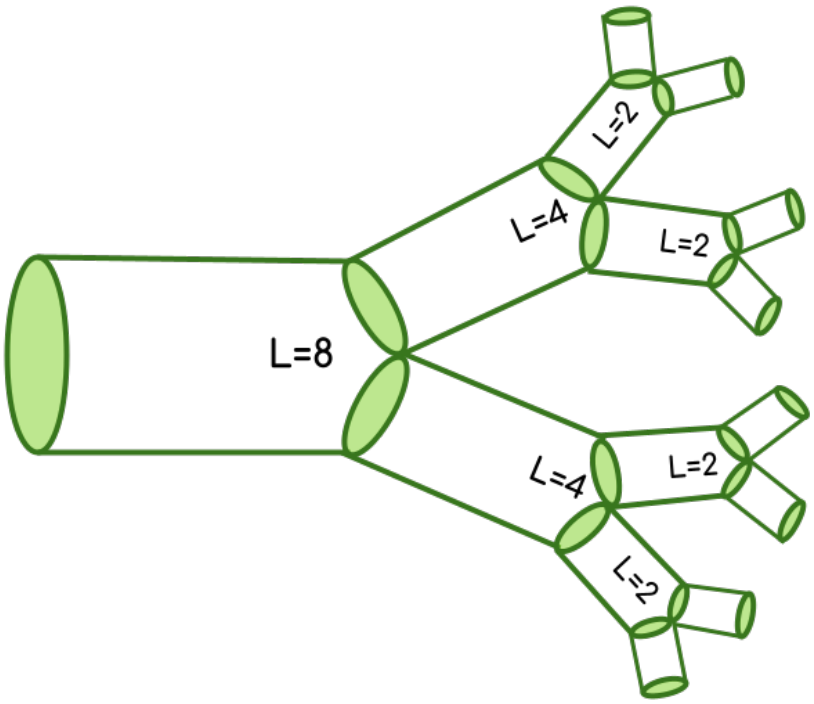

Figure 3.2. Branching Network with Leaf Number

will allow us to determine where the most asymmetry occurs in terms of distance from the soma, as illustrated in Figure 3.4.

Note that there is an analogous formulation for the difference scale factor for length, $\Delta\gamma = \frac{\gamma_1 - \gamma_2}{2}$. In our analysis, we fix the length scale factor, $\Delta\gamma = \frac{\gamma_1 - \gamma_2}{2}$, to always be positive. This enforces the following sign convention on the difference scale factor for radius. Consequently, when $\Delta\beta > 0$, one child branch will be both wider and longer than the other child branch. When $\Delta\beta < 0$, one child branch will be wider and shorter than the other child branch. These two scenarios correspond to *positive* and *negative* asymmetric branching and provide a visual way to interpret our results. Here, we focus on branch width rather than length, meaning our results are meaningful in terms of the magnitude but not the direction of asymmetry. For the length scaling to be correctly interpreted, we need to use an alternative [85, 23, 18, 38] labeling scheme for branching networks, such as Horton-Strahler labeling. We expand upon this in the Discussion section, Section 3.5.

3.3 Methods

We use the method of undetermined Lagrange multipliers to optimize cost functions with varying constraints[96]. When we perform this optimization, we arrive at equations that relate the two radius scaling ratios to each other raised to some scaling exponent (as in Equation 2.9) and corresponding to a generalized conservation rule. We minimize the function by differentiating with respect to each scaling ratio and setting the result equal to zero to solve for the multiplier. Using the fact that the multiplier is constant at each generation k, we set $\lambda_k = \lambda_{k+1}$ to solve for the resultant equation. More details on each of these calculations can be found in the Appendix B.

To test the theoretical predictions and model, we compared the results to data from NeuroMorpho.Org - an online database with digital reconstructions from a wide range of species [10]. These reconstructions are obtained by manually tracing neuron image stacks using computational methods, some manual and some automatic, obtained using microscopic and staining techniques for in vitro neurons and slicing at regular intervals. This database provides 3D reconstruction data that are organized in text files that specify a pixel ID label for each point, the x,y,z spatial coordinates, the radius of the fiber at each point, and a parent pixel ID that refers to the adjacent pixel previously labelled. The scaling ratios for radius and length can be obtained by organizing this data in terms of branches. This is accomplished by finding the pixels at which the difference between the child pixel ID and the parent pixel ID is greater than 2, which can be defined as branching points. Based on the branching points, a branch ID and parent branch ID can be assigned to each of the pixels. The radius can be extracted from each of the branches by taking each of the radius values in each branch and averaging them. The length of each branch can be extracted by summing up the Euclidean distances between each of the points in the branch. Once the radius and length of each of the branches is found, the scaling ratios are computed by dividing the daughter radius by the corresponding value for the parent branch. We can identify the branches that have the same

parent to find the two daughters. To extract the scaling exponent P as defined in Equation 3.9, we use the fsolve function in the python library SciPy to numerically solve for the roots of the equation $1 - (\beta_1^P + \beta_2^P) = 0$.

We look at neuron reconstructions from both axons and dendrites for diverse cell types, brain regions, and species. Due to the small size of axons and the limited resolution of images, the data available on NeuroMorpho.Org are limited in scope. The axon reconstruction data were taken from the following species: fruit flies [54], dragonflies [48], crabs [17], chickens [44], and rats [73]. The neurons were taken from a range of brain regions: the midbrain, the hippocampus, the antennal lobe, the optic lobe, and the ventral nerve cord.

The Purkinje cells are from mice [80, 28, 81, 75], rats [71, 75, 118], and guinea pigs *Cavia porcellus* [95]. The motoneurons are from zebrafish [79, 112], turtles[31], mice [42], rats [99], rabbits [110], and cats [35].

To study peripheral nervous system (PNS) neurons, we sampled from reconstruction data that was labelled by region on NeuroMorpho.Org. This data was taken from fruit flies [50, 84, 127] and mice [14, 65, 26, 106] and includes dendritic arborizations, sensory neurons, somatic neurons, and touch receptors.

The scaling ratio data were filtered to remove all daughter pairs where the scaling ratio corresponding to either daughter is equal to 1.0; these values likely occur due to the resolution limit of the image where the radius of both the daughter and the parent branches are equal to the pixel size. Since these values contribute artifacts to the distributions extracted from the data, we remove them from the final dataset.

3.4 Results

Here, we present our results and compare our theoretical predictions with empirical data.

3.4.1 Theory Results

From the general cost function as described in Equation 3.1, we derive a suite of predictions for scaling relationships. Through this suite of mathematical relationships, we can use optimization to derive powers and corresponding scaling ratios associated with each neuronal function and mechanism. Table 3.1 summarizes the results of these optimizations. More details on the calculations are in Appendix B.

3.4.2 Data Results

Here, we compare the theoretical predictions to empirical results, including histograms showing distributions of scaling exponents and the relationship between asymmetry and network level, or distance from the soma. The scaling exponent data was restricted to values above 0. As in the neuroscience literature [66], we compared the median values in the data to the theoretical predictions. The colored dotted lines show the theoretical predictions for each of comparison to the median as well as the relative peaks in the data.

3.4.2.1 Asymmetry Distributions Across Branching Generations

Figure 3.3 shows the distributions of asymmetry in the branching junctions of each of the neurite types, where degree of asymmetry is represented as the difference scale factor, $\Delta\beta$. The value of μ is the mean of the data, and σ is the standard deviation. For all of the neurite types, there is a normal distribution of asymmetry factors, with a peak at the symmetric case, where $\Delta\beta = 0$. Purkinje cells show the least asymmetry, as σ is the smallest, which is consistent with expectations based on the visual symmetries in their branching architecture.

Figure 3.4 shows plots relating the degree of asymmetry to the Leaf Number, where the smaller leaf numbers are the tips closest to the synapses, as illustrated in Figure 3. Here, we focus on the magnitude of the difference scale rather than the direction of asymmetry, defined by the absolute value of the difference scale factor $\Delta\beta$, as defined previously.

Minimize	Constraint	Result	Exponent	Corresponding cell type	Data median (95% CI)
P	V	$\beta_1^2 + \beta_2^2 = 1$	2	Purkinje cell dendrites	2.14 (2.03-2.27)
$T_{avg,ummyel}$	V	$\beta_1^{5/2} + \beta_2^{5/2} = 1$	5/2	PNS neurons	2.98 (2.76-3.16)
$T_{max,unmyel}$	V	$\beta_1^{5/2} = 1$	5/2	PNS neurons	2.98 (2.76-3.16)
$T_{min,unmyel}$	V	$\beta_2^{5/2} = 1$	5/2	PNS neurons	2.98 (2.76-3.16)
$T_{avg,myel}$	V	$\beta_1^3 + \beta_2^3 = 1$	3	Axons	2.96 (2.66-3.23)
$T_{max,myel}$	V	$\beta_1^3 = 1$	3	Axons	2.96 (2.66-3.23)
$T_{min,unmyel}$	V	$\beta_2^3 = 1$	3	Axons	2.96 (2.66-3.23)
P	$T_{tot,ummyel}$	$\beta_1^{3/4} + \beta_2^{3/4} = 1$	3/4	Asymmetric motoneurons	0.90 (0.82-1.08)
P	$T_{max,ummyel}$	$\beta_1^{3/2} = 1$	3/2	Motoneurons	1.39 (1.35-1.42)
P	$T_{min,ummyel}$	$\beta_2^{3/2} = 1$	3/2	Motoneurons	1.39 (1.35-1.42)

Table 3.1. Theoretical Predictions for scaling exponents for different functions and comparisons to the median values in the data The first column is the function that is minimized, either P or T, as obtained by varying α in Equation 2.1. The second column represents a constraint function or a quantity that is held fixed in the optimization. The third column is the result of the minimization using the method of undetermined Lagrange multipliers, and the fourth column is the scaling exponent inferred from these results, which we can compare to the median in the data, including a 95% confidence interval shown in the sixth column.

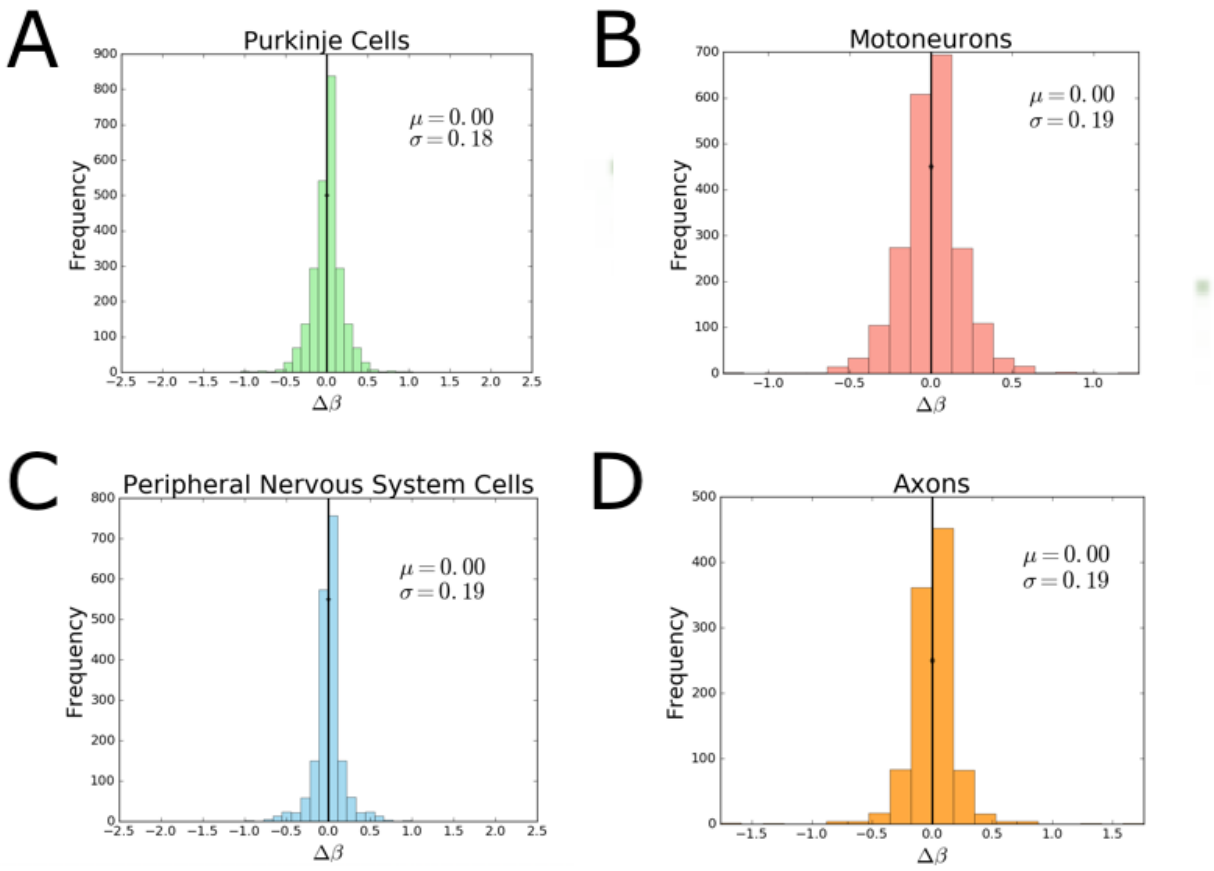

Figure 3.3. Plots of Asymmetric Difference Scale Factor for (A) Purkinje Cells, (B) Motoneurons, (C) Peripheral Nervous System Cells, and (D) Axons

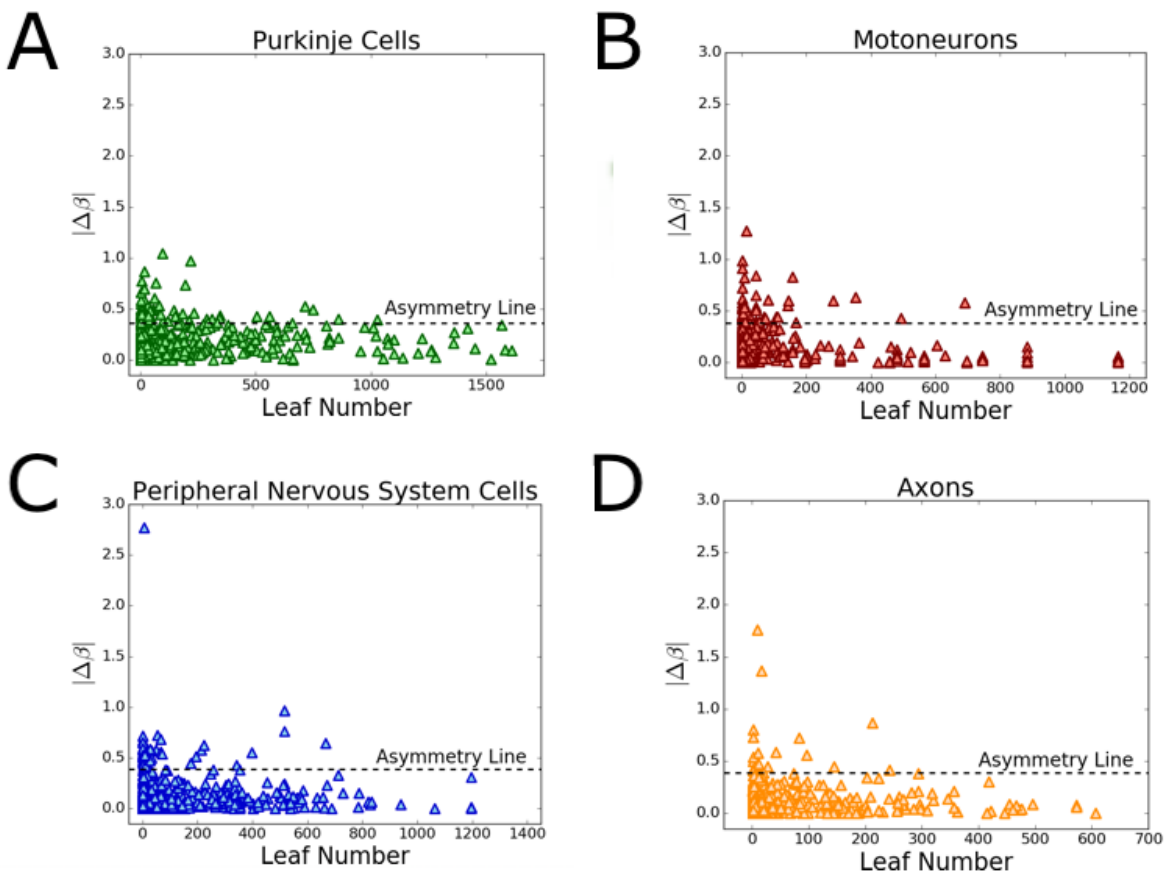

Figure 3.4. Plots of Degree of Asymmetry vs Leaf Number for A) Purkinje Cells, (B) Motoneurons, (C) Peripheral Nervous System Cells, and (D) Axons

The horizontal dashed line is what we define as a cutoff for the asymmetry line— a difference scale factor $\Delta\beta$ more than two standard deviations away from the mean (at which symmetry occurs)— that shows the division between the symmetric and asymmetric modes. We observe that the most asymmetric branching junctions, or those that occur above the asymmetry line, occur at lower leaf numbers, or closer to the synapses in the neuronal network.

3.4.2.2 Overall Network Power Distributions

Figure 3.5 shows the distributions of scaling exponents solved from the data. These show general network-wide trends in branching, and the corresponding solid black lines are the medians in the data. The medians in the Purkinje cell and motoneuron scaling exponent data correspond to the theoretical predictions for the functions minimizing power and the medians in the axons and PNS neuron scaling exponent data correspond to the theoretical predictions for the functions minimizing conduction time delay. The motoneuron data correspond to the prediction for the function that includes conduction time delay as a biophysical constraint, while the Purkinje cell data correspond to the prediction for the function that includes a material constraint.

3.4.2.3 Symmetric Versus Asymmetric Motoneuron Branching Junctions

Although the general network-wide trends are useful, we also split the data based on degree of asymmetry. We split the motoneuron data into symmetric and asymmetric branches, where the difference scale factor for the symmetric data fall within two standard deviations from 0. Analyzing the data separately in Figure 3.6, we find different median powers that correspond to theoretical predictions from different functions. The scaling exponent data for asymmetric branching junctions in motoneurons corresponds to the theoretical prediction for the function that interprets the conduction time delay as a sum of all possible paths,

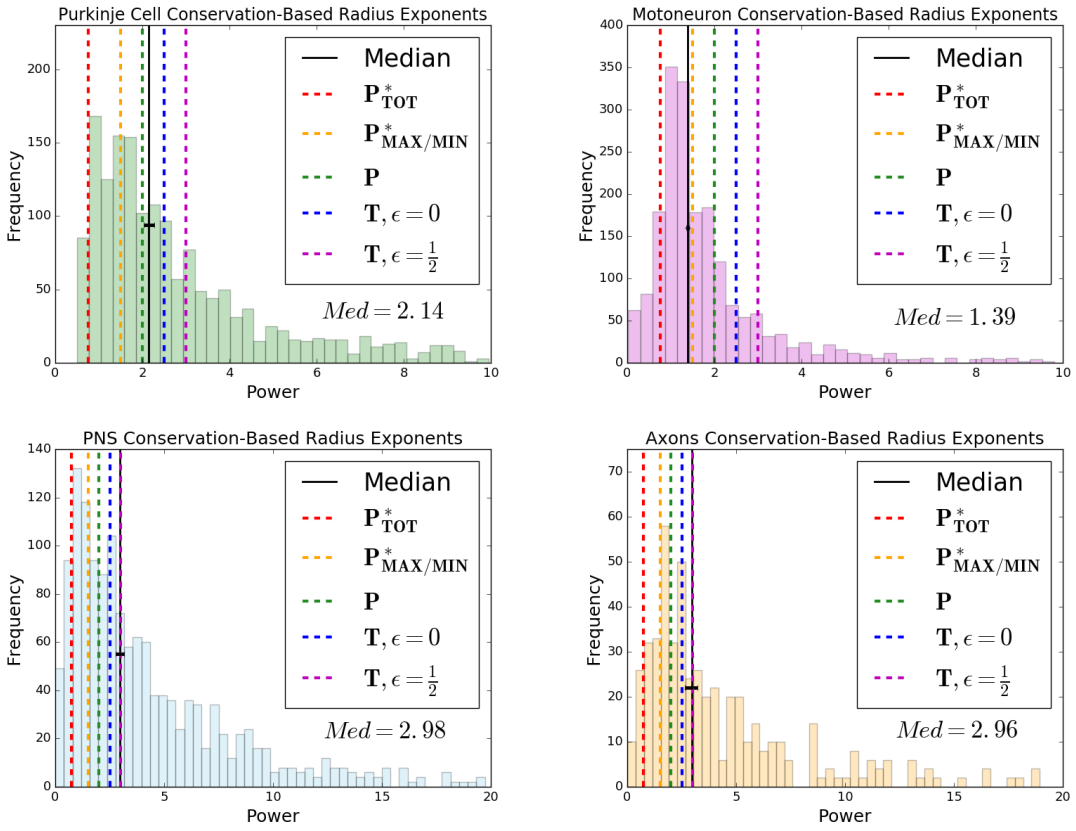

Figure 3.5. Branching Scaling Exponent Data

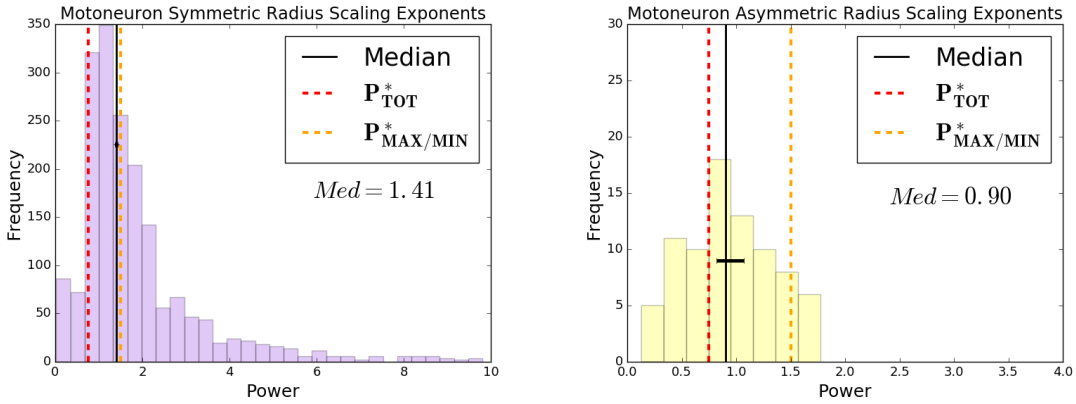

Figure 3.6. Symmetric and Asymmetric Scaling Exponent Data for Motoneuron Branching Junctions

while the data for the symmetric branching junctions correspond to the prediction for the function that considers one optimal path.

3.5 Discussion

Asymmetric branching in neurons gives rise to multiple possible paths from the soma to the synapses and vice versa. Although a symmetric branching network model can provide insights into the connections between branching patterns and functional principles of neurons, it obscures key features of these networks, such as large differences in path lengths from soma to tips and how those contribute to the functionality of neurons. The introduction of asymmetric branching to our model gives rise to multiple possible interpretations of the conduction time delay term, one that focuses on optimizing the path associated with either the maximum or minimum conduction time delay in the network, and another that takes into consideration the sum of all paths in the network. Notably, the mathematical results of the optimization of the models are the same for the symmetric model [38] and the maximum or minimum interpretation of conduction time delay in the asymmetric case. However, the total path interpretation of the conduction time delay leads to different results for the

function minimizing power with a time delay constraint. Moreover, for motoneurons, we find that splitting the scaling exponent data into the most symmetric and the most asymmetric data leads to different median values that correspond to theoretical predictions for different interpretations of this constraint, which also correspond to different regions in the cell relative to the soma and synapses. The median for asymmetric junctions corresponds to the theoretical prediction with the total path length interpretation of the conduction time delay constraint, suggesting that the whole network— rather than just one optimal path— is important for asymmetric branching junctions. The symmetric model obscures this distinction, and thus our comparisons of asymmetric and symmetric branching junctions lead us to look more closely at the position of branching junctions relative to the soma or the synapses, and whether there is any connection between this position and asymmetry.

We define this position using the key measure of leaf number. The distributions of leaf numbers shown in Figure 3.4 reflect what we know about differences in the structure of axons and dendrites. The maximum leaf number for axons is around 600, while it is around 1200-1600 for dendrites, thus reflecting the longer single parent branch for axons versus the more extensive branching and the greater number of branching generations for dendrites. Moreover, there are significant differences observed among different types of dendritic structures. The maximum leaf numbers for motoneurons and PNS neurons are around 1200, while it is around 1600 for Purkinje cells. We hypothesize that these differences might be due to differences in extracellular environments; motoneurons and PNS neurons are both part of the sensorimotor circuits that are localized in distal parts of the body, while Purkinje cells are located in the cerebellum within the brain itself. As dendrite branch formation is controlled by guidance cues in the environment that trigger complex intracellular signalling cascades and lead to protrusions [63], the vastly disparate biological environments and extrinsic cues likely greatly influence the extent of dendritic branching in these different cell types.

Although our analysis of the correspondences across cell types focuses on median values

in the data, as seen in other biological networks [114], we find much more variance at the local level. In neuroscience, theoretical and experimental work has shown that motoneurons grow in a roughly self-referential manner and their basic structure and branching points are predetermined. However, environmental cues and activity-dependent behavior cause local changes in morphology [77, 63]. Here, we are able to observe that the median scaling exponents differ significantly for symmetric and asymmetric branching in motoneurons, corresponding to different theoretical predictions. It is possible that the variance in symmetry of branching junctions might account for the wide distribution of scaling exponents for each cell type. The distributions of scaling exponents have a wide variance and multiple local peaks. Although we map the median scaling exponent to the closest theoretical prediction in this analysis, it is possible that there are multiple functional principles at play at different localized regions of the cells, corresponding to the peaks observed across the distribution. Moreover, we observe a correspondence between asymmetry of branching junctions and their relative position in a neurite, whether they are closer to the tips or to the soma. At the tips, where the leaf number is closest to zero, the branching junctions can be either extremely symmetric or extremely asymmetric.

Importantly, the most asymmetric branching junctions always occur at the tips. In contrast, the branching junctions that occur closest to the soma all fall under the symmetric type, where the $\Delta\beta$ value is within two standard deviations from the symmetric case. Thus, we observe **two different symmetry/asymmetry regimes, with a shift from the most symmetric branching at the soma to an increased number of asymmetric branching junctions at the tips**.

Because the tips of axons and dendrites are closest to the synapses, this suggests that the asymmetry might have to do with the forming of actual connections at the tips. This is consistent with existing knowledge that the branching of axons and dendrites is determined by synapses; new branches are formed preferentially near the synapses[115]. Moreover, previous studies have shown that there are activity-dependent changes in morphology of motoneurons

[57]. Studies of other biological networks have also shown that they are robust to damage and changes in the environment, developing corresponding changes in morphology to adapt to environments [59]. It is possible that the difference in power observed at the tip is due to changes as a result of activity-dependent behavior such as synaptic formation and pruning. This is consistent with empirically-informed mathematical models that describe the elongation of neurites as an extension of the cytoskeleton, where the most active building blocks (microtubules) are located at the distal portions and tips, making them more susceptible to developmental variation based on environmental cues [78].

Moreover, the fact that for asymmetric branching junctions, the interpretation of conduction time delay as a sum of all possible paths rather than one optimal path supports the notion that asymmetric branching is connected to plasticity in the network. These asymmetric branching patterns are determined by the sum of paths across the whole network, suggesting that the whole network is optimized in a way that is robust to damage in single paths and such that the whole network is optimized to make as many synaptic connections with other neurites as possible.

In this analysis, we have chosen to focus on radius scaling ratios and asymmetries that occur in the width of daughter branches. Although length asymmetry might provide additional insights into the properties of these networks, the branch length measurements are not accurately characterized, as also previously reported for vascular scaling [85] as well as other types of plant and animal networks [23, 18]. Recent work suggests Horton-Strahler labeling — where the first level begins at the tips, and higher levels are determined when two branches of the same level combine — may yield better estimates of branch length scaling, as it has been previously applied to neurons and other biological networks[21, 116, 120]. In future work, we plan to investigate how this alternative labeling scheme for branch lengths compares with theoretical predictions derived using our framework. If we are able to obtain meaningful results from the analysis of length scaling ratios, the direction of asymmetry and the distinction between the two types—*positive* and *negative* asymmetry— will be an

important consideration in addition to the magnitude which we focused on here.

Moreover, we aim to formulate a new constraint that relates to the way in which neurons fill space. So far, our optimization considers only intrinsic properties of neurons without explicitly accounting for: 1. interactions amongst neurons, 2. electrical activity that might strengthen or prune synapses, and 3. environmental chemoattractants and chemorepellants that might shape the growth and development of neurons, particularly in relation to their length. Adding this interaction term might lead us to understand length scaling ratios more.

Future studies have the potential to illuminate the function of asymmetry in neuron plasticity by analyzing in-vivo neuron image data taken across stages of development. Long term, a greater understanding of the details of the asymmetries observed within and among neurites and single cells may help pave the way to understanding lateral asymmetries in the brain and the structure-function correspondence.

In conclusion, we find that our asymmetric branching model for axons and dendrites brings to light the importance of considering all possible paths from the synapse to the soma rather than one optimal path. While this distinction does not affect the predictions for functions that minimize conduction time delay, they alter the predictions for the functions that minimize power and fix conduction time delay as a constraint. For motoneurons, the different interpretations of conduction time delay correspond to the median in the scaling exponent data of different types of branching junctions. The symmetric branching junctions agree with the predictions focusing on one optimal path, while the asymmetric branching junctions agree with the predictions that take all paths into consideration.

Moreover, the asymmetric branching junctions are localized closer to the synapses, suggesting that there is some connection between asymmetric branching and environmental factors, plasticity, and whole network robustness. This distinction between predictions for asymmetric and symmetric branching is observed only when time delay is a constraint (as opposed to a function to be minimized) and for motoneuron dendrites (but not axons). This is consistent with the notion that dendrites, in contrast to axons, are shorter with more

extensive branching that allows them to connect to multiple other neurons [94]. Our results support the notion that the whole network with its various paths—rather than simply optimal paths—are important factors governing the structures of these dendrites. Dendrite branches must reach multiple potential synaptic targets, and these synaptic connections are constantly evolving, forming, and pruning. This asymmetric branching framework is necessary in order to study and reason about these features of the network.

Chapter 3 is taken from a submitted work that is currently under review by the dissertation author, ***Paheli Desai-Chowdhry****, Alexander B Brummer, Samhita Mallavarpu, and Van M Savage. "Neuronal Branching is Increasingly Asymmetric Near Synapses, Potentially Enabling Plasticity While Minimizing Energy Dissipation and Conduction Time." In:* Under Review *(2023). https://doi.org/10.1101/2023.05.20.541591 [39].*

CHAPTER 4

Information Flow Drives Localized Morphological Differences Across Neuronal and Glial Cell Types

4.1 Introduction

Neurons are the fundamental structural units of the nervous system, connecting to one another through their branching processes - axons and dendrites - that allow them to transmit information in the form of electrical and chemical signals. There is a vast diversity of different types of cells that have different morphological forms and biological functions in the nervous system circuitry [56]. Arguably, the first attempt at cell-type classification in neuroscience is credited to the neuroanatomist Santiago Ramón y Cajal, who made detailed drawings of the morphological forms of a range of neuronal cell types across species and attempted to comparatively analyze them, arriving at a set of biophysical functional principles that dictate neuron morphology [24]. While Ramón y Cajal's work focused on qualitative descriptions of the distinctions across these cell types, more recent work has made use of increasingly quantitative technology to analyze distinctions across cell-types and establish a quantitative structure-function correspondence [36, 30, 38, 46, 70, 2]. A major goal in cell-type classification in neuroscience is to establish a correspondence between the different criteria that distinguish cell types from one another, such as morphological, physiological, connective/topological, and molecular properties.

Another major goal is to better understand how disease affects these properties in different cell types, and whether there are disease-related alterations that are specific to certain

cell types [130].

In order to understand the structure, function, and pathology of neuronal cells, it is also important to understand the context in which these cells exist. About half of brain cells are comprised of non-neuronal nervous system cells, called glia. Glial cells are a broad class of cells consisting of the subcategories microglia, astrocytes, and oligodendrocytes [45]. For a long time, it was thought that they were simply glue for neurons without any specific function of their own [53]. More recent research has revealed a range of functions that make them integral to brain function and even information processing. Oligodendrocytes are essential in providing myelin sheaths that protect neuron processes and increase the conduction velocity of information transfer [90]. Astrocytes are a key part of synapses—the connections between neurons—that play important roles in regulating synaptic transmission and plasticity [9]. They also play a role in the signalling that controls blood flow and metabolism in the brain [13]. Microglia are key in generating immune responses and maintaining homeostasis in the central nervous system. They are very sensitive to the environment and they undergo drastic morphological changes in response to neuronal activity and the presence of pathogens [113]. Glial cells, unlike axons, cannot generate action potentials. However, they are electrically active and they communicate with neurons. Microglia and astrocytes in particular have been shown to respond to electrical stimulation [45]. Although their functions are vastly different, they have branching processes that are comparable to neurons, and allow for a similar method of quantitative morphological analysis.

Previous work analyzes the structure-function correspondence between other types of branching biological networks—such as blood vessels, lungs, and plants—by combining machine-learning classification techniques with a biologically informed mathematical theory that relates vessel branching structure to functional properties related to resource transport and supply. Rather than simply classifying cells based on arbitrary structural quantities, the connection of these features to function based on the theory provides insights into the structure-function correspondence [23]. Further work uses parameters extracted from

this theoretical model as features in classification methods that separate cancerous tissue from healthy vessel tissue, providing evidence for the promise of these parameters as potential imaging biomarkers to identify tumors [21]. While previous recent studies have used machine-learning methods to classify between different types of neuronal and glial cell types [2], the features they use are structural, and mechanistic insight into how these features relate to different in function is unclear. Moreover, while these studies focus on length as morphometric features classifying cell types [2], the caliber of neuronal and glial processes is an important structural feature in that it relates to information flow. Since we have previously built a theory relating neuron morphology to function inspired by this mathematical framework [38, 39], a promising approach to address cell-type classification as well as potential disease-related alterations in neuronal and glial cells is to combine this theory with machine-learning methods to comparatively analyze cells. Here, we conduct this analysis for different types of dendrites and glial cells as well as applying these methods to analyze differences between healthy cells and cells from tumor and epilepsy patients.

4.2 Theory

Our model considers the tradeoffs among biological functions that neuron structures are evolved to optimize. One important evolutionary function of neuronal networks is the transfer of large amounts of information between brain regions in a short amount of time [64]. At the individual cell level, the varied morphological forms observed for neurons are various adaptations to basic principles such as limiting signal time delay [24]. Thus, it is important to consider conduction time as a key evolutionary principle that governs neuronal branching structures. We formulate this model based on the dependence of conduction velocity on fiber radius and myelination, using principles set forth by Hodgkin and Rushton [52, 100]. In addition to optimizing solely conduction time velocity in neurons, there are additional costs due to signaling in the brain that consumes a substantial amount of energy [12], suggesting

that energy expenditure is another important factor that constrains neuron structure. Previous work has shown that the relationship between metabolic rate and conduction time plays an important role in determining axon function in species across scales of body size [121]. This leads to the WBE framework, which relies on the assumption that resource distribution networks are optimized such that the energy used to transport resources is minimized [125]. Our model includes both conduction time and energy efficiency while also incorporating additional factors such as material costs and space-filling [24]. Synthesizing these ideas leads to a unifying model that can predict various morphological structural parameters for axons and dendrites across a range of cell types [38, 39].

We represent neurons as hierarchically branching information processing networks, with successive branching levels that decrease in radius and length according to a scaling relationship. We define β as the scaling relationship between the daughter and parent widths, $\frac{r_{k+1}}{r_k}$. Figure 3.1 illustrates this with a representative image and a diagram of a branching junction. Since these branching junctions are often asymmetric—that is, the two daughter branches are not equal to one another—there are two separate scaling ratios that correspond to each of the daughter branches, β_1 and β_2. Based on these two quantities, we can define the average scale factor as $\bar{\beta} = \frac{\beta_1+\beta_2}{2}$ and the difference scale factor as $\Delta\beta = \frac{\beta_1-\beta_2}{2}$ (shown in Figure 3.1 (C)) based on conventions in previous work [22]. If we define β_1 as the scaling ratio corresponding to the larger branch, we can describe β_1 and β_2 in terms of the average and absolute value difference scale factors as in Equation 1.

$$\beta_1 = \bar{\beta} + |\Delta\beta|; \beta_2 = \bar{\beta} - |\Delta\beta| \tag{4.1}$$

Thus, we can think of $|\Delta\beta|$ as a measure of the magnitude of the asymmetry, or the amount of shift away from the average. Figure 3.1 (D) shows a distribution of $\Delta\beta$ in data combined across a range of cell types and species, preserving the sign as well as the magnitude to show variance around the symmetric case in both directions.

We predict how biological function such as information processing and space-filling govern the branching structure of neurons by optimizing a mathematical cost function subject to a set of constraints, which allows us to obtain theoretical predictions for structural parameters that are the best possible given the biological constraints of the physical system [19]. Here, we choose a cost function that minimizes conduction time delay and energy consumption (represented by power loss) that is subject to computational, biological, and physical constraints. The biophysical constraints are represented as functions and added to the expressions to be minimized, allowing us to use the method of undetermined Lagrange multipliers to optimize this overall objective function [96].

$$C = \alpha P + (1 - \alpha)T + \sum_i \lambda_i f_i(r_k, l_k, k, N, n, \epsilon) \tag{4.2}$$

In this general function C, we can define P as the power lost due to dissipation, which relates to the decay of signals traveling in dendrites from the synapses to the cell body. For a neuronal network, we define the power loss by the equation, $P = I_0^2 R_{net}$, where I_0 is the ionic current and R_{net} is the resistance to current flow in the network. Because we are focusing on average, large scale quantities across the full extent of the neuron and need to consider a coarse-grained average of signal propagation, we can reasonably approximate axons and dendrites as wires through which current flows and encounters resistance from the neuron fiber. The resistance is given by $R_k = \frac{\rho l_k}{A_k}$, where A_k is the cross sectional area of the wire, and l_k is the length of the segment at that level. The parameter ρ is the intrinsic resistivity of the axon or dendrite, and we assume that ρ is constant, meaning that the material is uniform [56]. Approximating axons and dendrites as cylinders, the cross-sectional area is πr_k^2 for level k, and the resistance is $R_k = \frac{\rho l_k}{\pi r_k^2}$. Following standard practice, we have absorbed all physical constants into the Lagrange constants, and the magnitude of these terms do not affect the theoretical predictions.

For an asymmetric branching junction, we define the power loss across the branching network based on recursion using the scaling rations β_1 and β_2 as well as the analogous

length scaling relationships, defined as $\gamma = \frac{l_{k+1}}{l_k}$. Using our expressions for these quantities based on the average and difference scale factors in Equation 1, we can describe P as

$$P = R_{N,TOT} \sum_{k=0}^{N} \left(\prod_{j=k}^{N-1} \left[\frac{(\bar{\beta_j} + |\Delta\beta_j|)^2}{\bar{\gamma_j} + |\Delta\gamma_j|} + \frac{(\bar{\beta_j} - |\Delta\beta_j|)^2}{\bar{\gamma_j} + |\Delta\gamma_j|} \right] \right) \tag{4.3}$$

In our analysis, we fix the length scale factor, $\Delta\gamma = \frac{\gamma_1 - \gamma_2}{2}$, to always be positive. This enforces the following sign convention on the difference scale factor for radius. Consequently, when $\Delta\beta > 0$, one child branch will be both wider and longer than the other child branch. When $\Delta\beta < 0$, one child branch will be wider and shorter than the other child branch. These two scenarios correspond to *positive* and *negative* asymmetric branching and provide a visual way to interpret our results. Here, we focus on branch width rather than length, meaning our results are meaningful in terms of the magnitude but not the direction of asymmetry. For the length scaling to be correctly interpreted, we need to use an alternative [85, 23, 18, 38] labeling scheme for branching networks, such as Horton-Strahler labeling. We expand upon this in the Discussion.

In our function C, the parameter α can be varied to consider the tradeoff between the two principles, P, power loss, and T, conduction time delay. Here, we focus on dendrites and glia, which are associated with passive cable attenuation as a key principle rather than action potentials [30, 94, 45]. This is associated with the principle P, which is related to a voltage drop. We confirm this by looking at the range of scaling ratios and exponents in the data and noticing that they all fall within the range of predictions for specific cases of the function C that focus on minimizing power loss, P, as predicted in our previous work [38, 39]. Our function T, time delay, as described in our model is associated more with active conduction, or action potentials. We associate this principle more with axons, as they are designed to transmit large amounts of energy in a short amount of time [94]. Since we do not analyze axons as extensively in this study, we omit the expression for T. More information on this principle can be found in our previous work [39]. We elaborate on this in the Discussion.

It is clear that the parameters $\bar{\beta}$ and $\Delta\beta$ as defined by this model contribute to information flows through these networks. Although previous work on other types of biological networks focused on these parameters as features to classify between networks [23], here, we explore the incorporation of another feature into our classification. In order to quantify the distance of a branching junction relative to the soma and the synapses, we can use an established measure called leaf number that has been used to study scaling in dendritic branching [66]. We will refer to the leaf number as L_n throughout this paper and will later use a relative measure, $L_{n,rel}$, to normalize this parameter across cells to allow for comparisons based on distance from the soma. The leaf number is defined as the number of tips that are distal to each branch. The leaf number at the tips will be equal to 0, and the leaf number will be greatest near the soma. Figure 3.2 illustrates leaf numbering. For each pair of radius scaling ratios in the data, we have a corresponding leaf number of the parent branch of the junction. Our previous work has shown that the most asymmetric branching junctions occur closest to the tips or the synapses. Moreover, there are different functional principles governing the structure at different regions of the cells [39]. Here, we argue that leaf number provides us with essential information about these structures and their correspondence with function. For some comparisons, incorporating leaf number plays a greater role in distinguishing the two groups, as the classification methods perform better with the inclusion of $L_{n,rel}$ as a feature.

For the comparison of diseased cells to healthy cells in particular, there are differences that occur at specific leaf numbers, meaning different locations in the cell. Our results thus suggest that the morphological distinctions between cells are driven by information flow at localized cell regions.

4.3 Methods

The morphological data we analyze in this study is taken from NeuroMorpho.Org [10], an online database with a large amount of morphological data reconstructed from neuron and glia images for a range of cell types and species. In this study, we focus on 4 different types of dendrites—motoneurons, purkinje cells, medium spiny neurons (MSNs), and pyramidal cells—and two different types of glial cells—astrocytes and microglia—along with some axon data. The quantitative morphological data is extracted from images by tracing neuron image stacks using computational methods, some manual and some automatic, that were obtained using a range of microscopic and staining techniques for in vitro neurons sliced at regular intervals. We analyze a total of 160 individual images and 6689 branching points. The motoneurons were from cats [35], mice [20], and rats [99]. The Purkinje cells were from mice [28, 69]. The medium spiny neurons were from mice [49]. The pyramidal neurons were from humans [61, 5]. The astrocytes were from mice[68, 32, 67] and rats [27]. The microglia were from mice [11, 98, 1] and rats [8, 76]. The axons were from mice [14].

The data is stored in text files by pixel, where each pixel contains a pixel ID number, x, y, and z spatial coordinates, the radius (based on the distance from the location of the pixel to the edge of the process on each side), and a parent pixel ID number referring to the previous pixel to which each pixel connects. For this analysis, we convert this pixel-based data to branch-based data, defining the branch points in the pixel data by identifying the pairs of pixels where the parent pixel ID numbers are separated by 2 or more. Thus, we obtain branch-based data with a list of branch ID numbers and corresponding parent branch ID numbers. For each branch, we take the average radius of each of the pixels belonging to that branch to assign a radius value.

For each branch, we can find the scaling ratio, β, by dividing its radius by the radius of the parent branch to which it is assigned. We can identify two daughter branches of the same branching junction by identifying branches that share the same parent branch. From

the two daughters, we can extract the parameters $\bar{\beta}$ and $\Delta\beta$ by computing $\bar{\beta} = \frac{\beta_1+\beta_2}{2}$ and $\Delta\beta = \frac{\beta_1-\beta_2}{2}$. We filter this data by removing all pairs of daughter for which any one of the daughters has $\beta \geq 0.999$. The values that are very close to 1 are likely an artifact due to the resolution limit of the images; after a certain level, all of the radius value are equal to the pixel size of the image, leading to the computation of $\beta \approx 1$. Filtering these data removes large peaks and symmetries observed in the raw data that are due to these limitations of the measurements.

In this study, we are also interested in looking at the position of these branching junctions relative to the soma and the synapses. We measure this based on the leaf number, L_n—the number of distal branches at every branching junction. We calculate this by looping through the branch data, identifying the tips as the branches that are not the parent branches of other branches, and assigning each of the remaining branches the sum of the number of distal tips of its daughters branches. However, in order to normalize these L_n values to allow for comparisons between different cells and cell-types, we define a new parameter, $L_{n,rel}$. For each cell, from the list of L_n values, we identify the maximum value, $L_{n,max}$, defining the branch furthest from the tips or closest to the soma. We define each of the other $L_{n,rel}$ values at each point i relative to this value, computing $L_{n,rel,i} = log_2\left(\frac{L_{n,max}}{L_{n,i}}\right)$. Thus, for the point at which $L_{n,max} = L_n$, $L_{n,rel}$ is equal to 0, defines the soma. For some images, we averaged the values of $\bar{\beta}$ and $\Delta\beta$ at each $L_{n,rel}$ for each image or cell-type in order to aid visualization and discernment of clusters in the data.

For each comparison, we assigned each cell-type a classifier label to be either 0 or 1. The closest set to a balanced set was created by balancing the number of images used for each cell-type, but it should be noted that with this method, it is not possible to control for the number of data points in each image due to the variability of the images. When two cell-types were being compared and more data were available for one type, a subset of data for that type was used for comparison in order to achieve even more balance. Between 70-80% of the images were randomly assigned to the training data for each cell type, and the remaining data

were assigned to the test set. We used 7 different machine-learning classification methods, which we later refer to by abbreviations: Logistic Regression (LR), Support Vector Machine (SVM), K-Nearest Neighbors (KNN), Random Forest (RF), Decision Tree (DT), Naïve Bayes (Bayes), and Neural Networks (NN). These methods were implemented in RStudio. For Logistic Regression, we used the function *glm* to build the model for the classifier. For Support Vector Machine and Naïve Bayes classification, we used the package 'e1071', using the functions *svm* and *naiveBayes*. For SVM, we used the 'radial' kernel, which we showed to perform better than other kernels. This is supported by previous results [2, 72]. For K-Nearest Neighbors, we used the package 'FNN' using the function *knn*, where the number of nearest neighbors, k, was chosen based on local maxima of the performance metrics of classification, accuracy and AUC. For Random Forest classification, we used the package 'randomForest', using the function *randomForest*. For Decision Tree classification, we used the package 'rpart', using the function *rpart*. For Neural Networks, we used the package 'neuralnet', using the functions *neuralnet* and *compute*.

These classification methods use the features, either $\bar{\beta}$ and $\Delta\beta$ or $\bar{\beta}$, $\Delta\beta$, and $L_{n,rel}$ and the assigned classifier label in the training set to predict the classifier labels for each of the points in the test set. These predicted values are given in a list of the length of the number of points in the test data. One way to measure the performance of the classification methods is to look at how accurately the points are classified, comparing the predictions to the classifier labels of each of the points in the test set and reporting the percentage of points that are labeled accurately. Here, in Table 4.9, we report the accuracy measures of each of the classification methods by image, where the classification was performed on the raw branching junction test data for all the images, and the average predicted label for each image was compared to the true label. However, a more useful measure of the performance of these methods is the area under the curve (AUC) of the Receiver Operating Characteristic (ROC) Curve that considers the tradeoff between true positive rates and false positive rates, which is more useful for datasets like these that are not balanced. Tables

4.1-8 report the performance of the 7 classification methods based on the AUC, where the uncertainty measure is based on a 95% confidence interval. The ROC metrics, such as the AUC and confidence intervals, were computed using the package 'pROC.' The plots of the ROC curves were created using the package 'ggplot2.' The plots of all other visualizations were created using the Python library matplotlib.

4.4 Results

In Figure 4.1, we illustrate the feature space of the combined data from a range of different dendritic cell-types, as well as axons and glial cells, based on $\bar{\beta}$, $\Delta\beta$, and $L_{n,rel}$. We can locate clear clusters that indicate the distinctions between the types based on these features. Figure 4.2 further indicates the distinctions between dendrites, axons, and glial processes. We observe that out of the cell and process types observed here, the small localized cluster at low $\bar{\beta}$ as well as low $L_{n,rel}$ values are unique to dendrites. It is important to note that for all of these cell and process types, there appears to be a general relationship between both $\bar{\beta}$ and $L_{n,rel}$ as well as between $\Delta\beta$ and $L_{n,rel}$, as we show in Figure 4.3.

We further illuminate the differences between different cell-types within these three groups, comparing dendrites and glial cells first, and then applying these methods to look at distinctions between healthy and diseased cells.

4.4.1 Dendrites

Here, we compare 4 different types of dendrites—Motoneurons, Purkinje cells, Medium Spiny Neurons, and Pyramidal cells—for a total of 6 comparisons. Visual representations of these cells, reconstructed from the image morphological data on NeuroMorpho.Org [10] are shown in Figure 4.4. Tables 1, 2, 3, 4, 5, and 6 show the performance of 7 different classification methods. We first compare these dendrites using $\bar{\beta}$ and $\Delta\beta$ as features, as shown in Figure 4.5. The performance of these methods are measured by the AUC (area under curve) of the

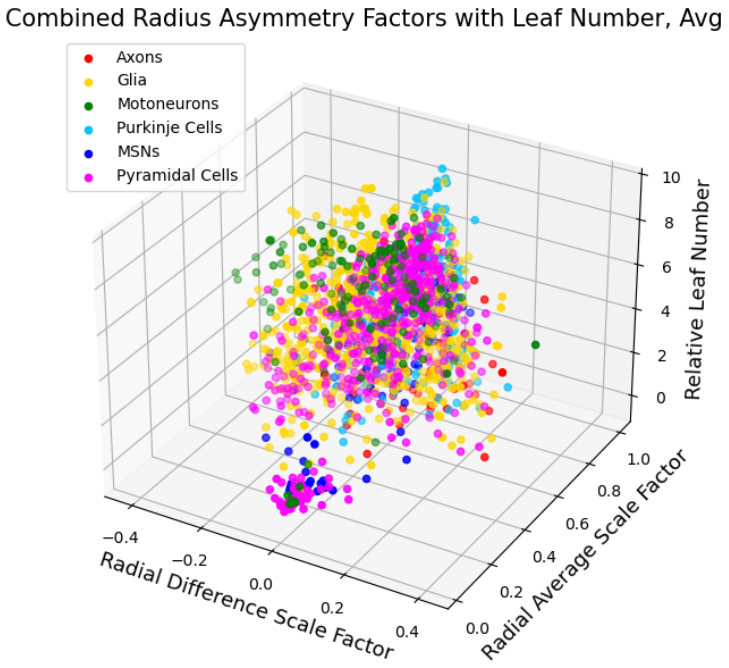

Figure 4.1. Plots of different cell/process types in the feature space of $\bar{\beta}$, $\Delta\beta$, and $L_{n,rel}$. Here, for each image, the average $\bar{\beta}$ and $\Delta\beta$ are taken at each level, $L_{n,rel}$

ROC curves, which are also shown in Figure 4.6. Next, we compare these dendrites using $\bar{\beta}$, $\Delta\beta$, and $L_{n,rel}$ as features, as shown in Figure 4.7. The ROC curves for this feature space are also shown in 4.8. The data in Tables 4.1-6 are based on the combined branching point data for all images. Classification of the cell-types in the test sets based on the whole images, or the average prediction of each of the points in the images, is shown in Table 4.9.

For all of these comparisons, the 7 classification methods perform relatively well, and incorporating $L_{n,rel}$ as an additional feature in the classification improves the performance, though the improvement is most significant for the comparison of Medium Spiny Neurons and all the other three cells. The classification method that consistently performed the best for all comparisons was Random Forest.

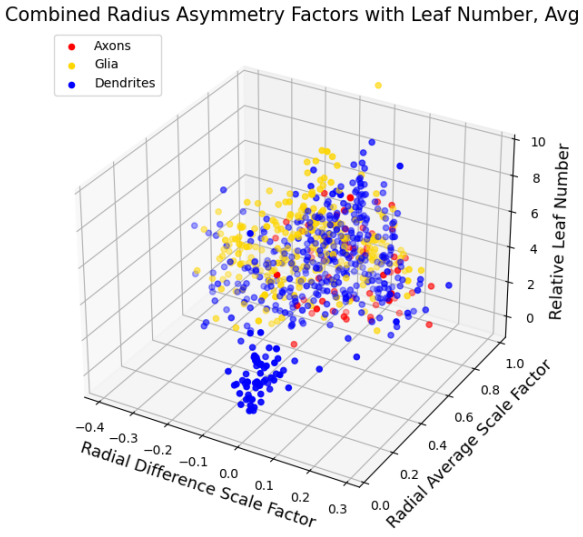

Figure 4.2. Plots of different cell/process types, clustered by axons, dendrites, and glial cells, in the feature space of $\overline{\beta}$, $\Delta\beta$, and $L_{n,rel}$. Here, for each cell type, the average $\overline{\beta}$ and $\Delta\beta$ are taken at each level, $L_{n,rel}$

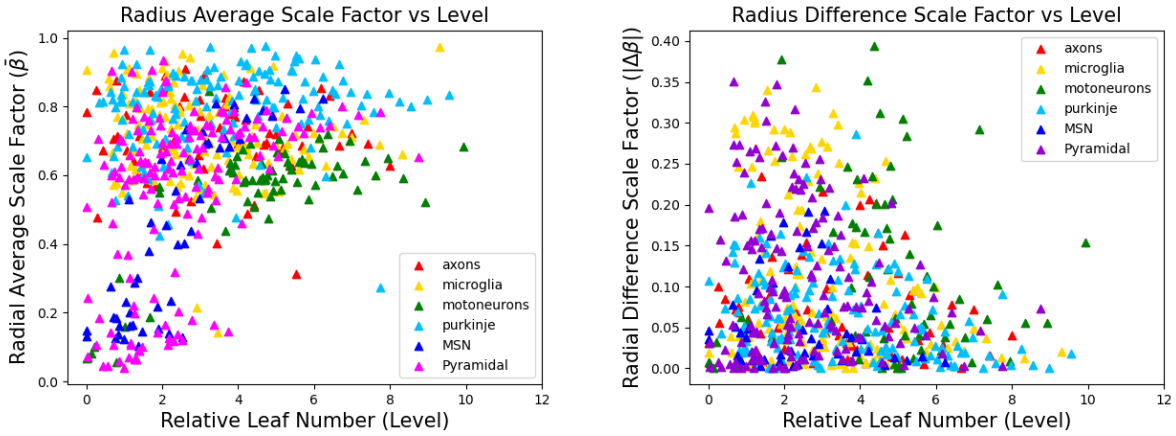

Figure 4.3. Plots showing the relationship between the average scale factor and the relative leaf number and the magnitude of the difference scale factor and the relative leaf number.

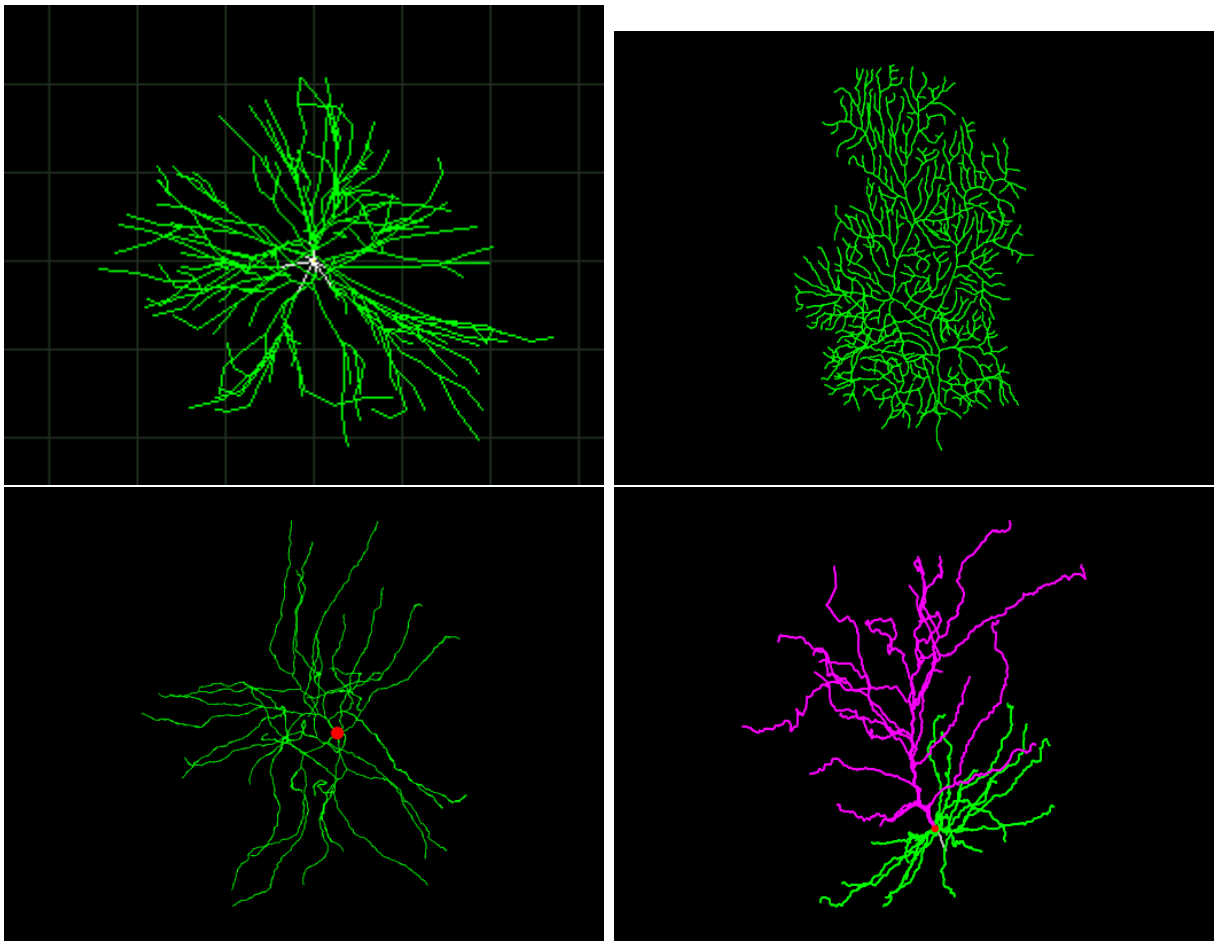

Figure 4.4. Images showing reconstructions of the images and morphological data from NeuroMorpho.Org [10] for different dendrite types including Motoneurons, from a cat [35] (upper left), Purkinje Cells, from a mouse [81] (upper right), Medium Spiny Neurons, from a mouse [49] (lower left), and Pyramidal Cells, from a human [5] (lower right).

4.4.2 Glia

Here, we compare two different types of glial cells—astrocytes and microglia. Visual representations of these cells, reconstructed from the image morphological data on NeuroMorpho.Org [10] are shown in Figure 4.9. Table 4.7 shows the performance of 7 different classification methods. We compare these glial cells using both the 2-dimensional and 3-dimensional feature spaces as previously defined, shown in Figure 4.10. The performance of these methods

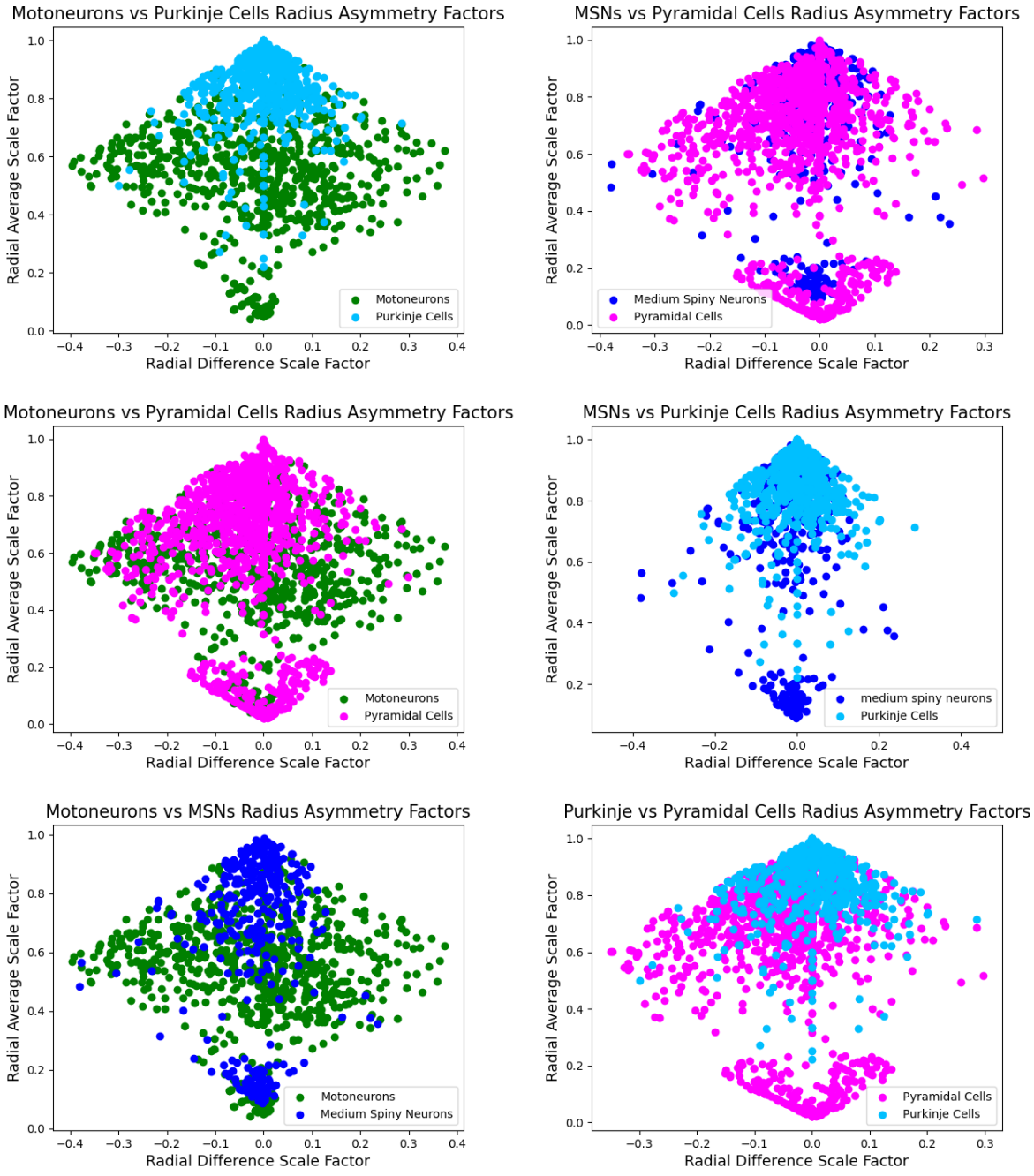

Figure 4.5. Plots of 2-dimensional feature spaces of the training data for 6 different combinations of dendritic types

Table 4.1. Motoneurons versus Purkinje Cells Classification AUC (Area Under ROC curve) Measures

Features/Method	LR	SVM	KNN	RF	DT	Bayes	NN
$\bar{\beta}, \mathbf{\Delta}\beta$	0.719 ±0.058	0.700 ±0.062	0.735 ±0.055	0.761 ±0.052	0.695 ±0.056	0.723 ±0.057	0.719 ±0.058
$\bar{\beta}, \mathbf{\Delta}\beta, L_{n,rel}$	0.723 ±0.056	0.766 ±0.053	0.691 ±0.058	0.715 ±0.056	0.729 ±0.053	0.724 ±0.057	0.738 ±0.057

Table 4.2. Medium Spiny Neurons versus Pyramidal Cells Classification AUC (Area Under ROC curve) Measures

Features/Method	LR	SVM	KNN	RF	DT	Bayes	NN
$\bar{\beta}, \mathbf{\Delta}\beta$	0.574 ±0.061	0.677 ±0.060	0.720 ±0.051	0.846 ±0.038	0.802 ±0.042	0.599 ±0.058	0.531 ±0.066
$\bar{\beta}, \mathbf{\Delta}\beta, L_{n,rel}$	0.760 ±0.041	0.830 ±0.043	0.834 ±0.034	0.912 ±0.026	0.856 ±0.031	0.740 ±0.043	0.766 ±0.043

Table 4.3. Motoneurons versus Pyramidal Cells Classification AUC (Area Under ROC curve) Measures

Features/Method	LR	SVM	KNN	RF	DT	Bayes	NN
$\bar{\beta}, \mathbf{\Delta}\beta$	0.681 ±0.041	0.816 ±0.033	0.792 ±0.036	0.827 ±0.032	0.793 ±0.035	0.776 ±0.038	0.680 ±0.041
$\bar{\beta}, \mathbf{\Delta}\beta, L_{n,rel}$	0.777 ±0.039	0.870 ±0.030	0.814 ±0.039	0.884 ±0.029	0.851 ±0.033	0.803 ±0.038	0.772 ±0.040

are measured by the AUC (area under curve) of the ROC curves, which are shown in Figure 4.11. The data in Table 4.7 are based on the combined branching point data for all images. Classification of the cell-types in the test sets based on the whole images, or the average prediction of each of the points in the images, is shown in Table 4.9.

Table 4.4. Medium Spiny Neurons versus Purkinje Cells Classification AUC (Area Under ROC curve) Measures

Features/Method	LR	SVM	KNN	RF	DT	Bayes	NN
$\bar{\beta}, \mathbf{\Delta}\beta$	0.578 ±0.075	0.599 ±0.074	0.616 ±0.073	0.771 ±0.059	0.639 ±0.064	0.624 ±0.072	0.579 ±0.075
$\bar{\beta}, \mathbf{\Delta}\beta, L_{n,rel}$	0.776 ±0.060	0.884 ±0.045	0.861 ±0.048	0.907 ±0.038	0.854 ±0.049	0.742 ±0.064	0.792 ±0.062

Table 4.5. Motoneurons versus Medium Spiny Neurons Classification AUC (Area Under ROC curve) Measures

Features/Method	LR	SVM	KNN	RF	DT	Bayes	NN
$\bar{\beta}, \mathbf{\Delta}\beta$	0.586 ±0.071	0.749 ±0.056	0.746 ±0.056	0.805 ±0.048	0.732 ±0.054	0.747 ±0.054	0.549 ±0.059
$\bar{\beta}, \mathbf{\Delta}\beta, L_{n,rel}$	0.885 ±0.035	0.924 ±0.029	0.871 ±0.036	0.952 ±0.021	0.923 ±0.027	0.835 ±0.047	0.886 ±0.035

Table 4.6. Purkinje versus Pyramidal Cells Classification AUC (Area Under ROC curve) Measures

Features/Method	LR	SVM	KNN	RF	DT	Bayes	NN
$\bar{\beta}, \mathbf{\Delta}\beta$	0.563 ±0.061	0.660 ±0.060	0.701 ±0.049	0.802 ±0.042	0.607 ±0.051	0.532 ±0.060	0.564 ±0.062
$\bar{\beta}, \mathbf{\Delta}\beta, L_{n,rel}$	0.585 ±0.063	0.794 ±0.053	0.784 ±0.051	0.873 ±0.038	0.824 ±0.052	0.566 ±0.064	0.665 ±0.060

Here, incorporating $L_{n,rel}$ as an additional feature in the classification significantly improves the performance of all 7 classification methods, as the data are nearly indistinguishable for the 2-dimensional feature space, but high AUC and accuracy values for most methods using the 3-dimensional space. The classification method that performed the best was Random

Table 4.7. Astrocytes versus Microglia Classification AUC (Area Under ROC curve) Measures

Features/Method	LR	SVM	KNN	RF	DT	Bayes	NN
$\bar{\beta}, \mathbf{\Delta}\beta$	0.549 $\pm$0.045	0.596 $\pm$0.043	0.596 $\pm$0.043	0.615 $\pm$0.044	0.571 $\pm$0.044	0.538 $\pm$0.046	0.544 $\pm$0.045
$\bar{\beta}, \mathbf{\Delta}\beta, L_{n,rel}$	0.753 $\pm$0.035	0.804 $\pm$0.031	0.775 $\pm$0.030	0.827 $\pm$0.027	0.702 $\pm$0.042	0.776 $\pm$0.031	0.794 $\pm$0.030

Forest.

4.4.3 Healthy versus Diseased Cells

Here, we apply these methods to attempt to distinguish between healthy and diseased dendrites in humans. We compare control cells for Pyramidal principle cells in the Middle Temporal Gyrus to two different classes of diseased cells—cells from patients with tumors and cells from patients with epilepsy. Table 4.8 shows the performance of 7 different classification methods, all using $\bar{\beta}$, $\Delta\beta$, and $L_{n,rel}$ as features. The performance of these classification methods are measured by the AUC (area under curve) of the ROC curves. The data in Table 4.8 are based on the combined branching point data for all images. Classification of the cell-types in the test sets based on the whole images, or the average prediction of each of the points in the images, is shown in Table 4.9.

We show both the 2-dimensional and 3-dimensional feature spaces for both these comparisons in Figure 4.12. As seen in these images, we can observe a significant distinction between the control and diseased cells in the data for both types, visible as clusters of the data with both low $\bar{\beta}$ and low $L_{n,rel}$ values. We filter the data to focus on the points with $L_{n,rel} = 0$, or the first branching junction in the tree from the soma, and then perform the classification methods again. This approach leads to better performance, although there is more uncertainty in the AUC values due to the limited number of data points. The per-

Table 4.8. Healthy versus Diseased Neurons Classification AUC (Area Under ROC curve) Measures

Features/Method	LR	SVM	KNN	RF	DT	Bayes	NN
Tumor	0.584 ±0.072	0.662 ±0.070	0.681 ±0.067	0.598 ±0.075	0.566 ±0.073	0.645 ±0.069	0.523 ±0.072
Tumor, Filtered	0.692 ±0.312	0.731 ±0.268	0.529 ±0.291	0.740 ±0.232	0.726 ±0.222	0.778 ±0.216	0.558 ±0.314
Epilepsy	0.563 ±0.057	0.661 ±0.054	0.608 ±0.056	0.748 ±0.047	0.699 ±0.051	0.588 ±0.056	0.585 ±0.049
Epilepsy, Filtered	0.668 ±0.186	0.806 ±0.145	0.827 ±0.136	0.812 ±0.132	0.868 ±0.117	0.796 ±0.171	0.796 ±0.158

formance of the classification methods using the filtered data is also reported in Table 4.8. We notice in the data that in this cluster where the distinction is observed, the $\Delta\beta$ values for the controls are closer to 0, or symmetric branching junctions, whereas the data for the diseased cells are significantly more asymmetric.

4.5 Discussion

Overall, radius scaling ratios, $\bar{\beta}$ and $\Delta\beta$, perform well in classifying between the 4 different types of dendrites, suggesting that information flow is a driving force in distinguishing different types of cells. For dendrites, signals generally travel from the synapses—the junctions between two cells—back to the cell body, and relate to the information flow of signals through the network through passive cable attentuation [94]. For most of these comparisons, these parameters related to information flow are generally sufficient to classify between them, as the improvement in the performance of all classification methods by including the third feature (relative leaf number) is minimal. In particular, the distinctions between Motoneurons and

Table 4.9. Image Based Classification Accuracy Measures

Classification/Method	LR	SVM	KNN	RF	DT	Bayes	NN
Motoneurons/Purkinje 2D	4/6	4/6	4/6	4/6	4/6	4/6	4/6
Motoneurons/Purkinje 3D	4/6	4/6	4/6	5/6	4/6	4/6	4/6
MSNs/Pyramidal 2D	13/21	13/21	13/21	17/21	14/21	13/21	10/21
MSNs/Pyramidal 3D	13/21	13/21	14/21	17/21	16/21	13/21	10/21
Motoneurons/Pyramidal 2D	3/6	4/6	4/6	4/6	4/6	4/6	4/6
Motoneurons/Pyramidal 3D	4/6	5/6	5/6	5/6	5/6	4/6	5/6
MSNs/Purkinje 2D	4/7	5/7	5/7	7/7	5/7	4/7	5/7
MSNs/Purkinje 3D	7/7	6/7	6/7	7/7	7/7	4/7	7/7
Motoneurons/MSNs 2D	3/7	4/7	5/7	6/7	4/7	4/7	3/7
Motoneurons/MSNs 3D	7/7	7/7	7/7	7/7	7/7	7/7	7/7
Purkinje/Pyramidal 2D	3/6	3/6	3/6	3/6	3/6	3/6	3/6
Purkinje/Pyramidal 3D	3/6	3/6	4/6	4/6	5/6	4/6	4/6
Astrocytes/Microglia 2D	7/10	7/10	7/10	7/10	7/10	7/10	6/10
Astrocytes/Microglia 3D	5/10	7/10	7/10	8/10	4/10	4/10	6/10
Tumor/Control	3/6	3/6	3/6	4/6	3/6	3/6	4/6
Tumor-Filtered/Control	3/6	5/6	2/6	4/6	5/6	4/6	4/6
Epilepsy/Control	5/10	5/10	6/10	9/10	6/10	6/10	7/10
Epilepsy-Filtered/Control	6/10	6/10	7/10	7/10	7/10	5/10	8/10

Purkinje Cells and between Motoneurons and Pyramidal Cells show minimal improvements. The cells with higher $\bar{\beta}$ values show on average less change in the radius from daughter to parent branches. It makes sense, for example, that these values are higher on average for Purkinje cells as compared to motoneurons because Purkinje cells have more extensive branching trees and signals must travel through many branching junctions in order to reach the soma. Less changes in the width means that the conduction velocity remains more steady

throughout the trajectory of a signal through the network. The observation that on average, the $\Delta\beta$ values remain closer to 0 for Purkinje cells is consistent with the fact that these structure tend to be symmetric.

For all the comparisons involving Medium Spiny Neurons, the incorporation of $L_{n,rel}$ as a feature more significantly improved performance across classification methods. This suggests that for Medium Spiny Neurons, there might be more region-specific differences in the information flow through dendrites. For classification between Purkinje Cells and Pyramidal Cells, both methods perform poorly for both 2-dimensional and 3-dimensional feature spaces, but some methods, such as Support Vector Machine, Decision Tree, and Neural Networks, perform better for the 3-dimensional feature space, and some methods, such as K-Nearest Neighbors and Random Forest, perform well for both spaces.

Interestingly, for glial cells, the distinction between the two cell-types—astrocytes and microglia—is not significant for the 2-dimensional feature space, but the addition of $L_{n,rel}$ as a feature very significantly boosts the performance of all classification methods. This suggests that for glial cells, there might be more region-specific differences in the information flow through their processes.

Due to the promise of these methods in classifying different types of neuronal and glial cell types, we apply these methods to look at distinctions between healthy cells and diseased cells in order to attempt to extract insights about the pathology. In this study, we focus on comparisons between control cells and cells from patients with tumors and epilepsy. Interestingly, although the classification methods were minimally successful in separating the diseased branching junctions from healthy branching junctions in the raw data, we observe that there is a clear distinction in the data localized at the soma. If we filter the data based on $L_{n,rel}$, focusing only on the data points with $L_{n,rel} = 0$, the classification methods perform much better. Observing the data, we notice that for the branching junctions at the soma, for the control cells, the $\Delta\beta$ values are centered closer to 0 (the symmetric case), whereas for both the tumor and epilepsy data, the $\Delta\beta$ values diverge from 0 (suggesting asymmetry).

We illustrate this observed phenomenon in Figure 4.13. This difference between healthy and diseased cells is localized near the soma, and suggests that there might be a potential biomarker to identify these diseased cells that is localized near the soma.

Out of all of the 7 machine learning classification methods utilized in this study, Random Forest performed consistently better than all other methods, both in terms of accuracy of classifying images and in terms of the tradeoff between true positive rates and false positive rates of classifying individual data points. The high performance of the Random Forest method over other standard methods has been previously noted [34]. The next method that tended to perform better than others was Support Vector Machine, using a radial kernel, which has been shown to perform well on biological data [2, 72]. An important advantage of both these methods is that they perform well when there is a relationship between the features [88, 102]. As we observe in Figure 2.4, there appears to be a nonlinear relationship between both $\bar{\beta}$ and $L_{n,rel}$ as well as between $\Delta\beta$ $L_{n,rel}$. This might explain the higher performance of RF and SVM over the Naïve Bayes method, for example, because Naïve Bayes makes the key assumption that the features are independent of one another [88, 105]. Moreover, methods such as K-Nearest Neighbors are sensitive to noise, which might explain their variable performance [88]. Random Forest methods are known to be more accurate compared to Decision Tree methods, as they are a combination of multiple decision trees [34].

In this analysis, we have chosen to focus on radius scaling ratios. Although length scaling ratios might provide additional insights into the distinctions between these cells in relation to other biological properties, such as the ways in which these branching processes fill space, the branch length measurements are not accurately characterized, as also previously reported for vascular scaling [85] as well as other types of plant and animal networks [23, 18]. Recent work suggests Horton-Strahler labeling — where the first level begins at the tips, and higher levels are determined when two branches of the same level combine — may yield better estimates of branch length scaling, as it has been previously applied to neurons and other

biological networks [21, 116, 120]. In future work, we plan to investigate how this alternative labeling scheme for branch lengths improves the characterization of length scaling ratios, and whether further insights into the distinctions between these cells can be gleaned from studying asymmetries in the lengths of daughter branches.

While our results are promising and suggest that this method of analysis is useful for extracting new insights about neuronal and glial cells, we are limited in the amount of morphological data available at a high enough precision to allow for this method of analysis. In particular, our ability to analyze axons was severely limited by the limited number of images available with the level of precision required for this analysis, as axons are generally thinner than dendrites and their widths are often smaller than the pixel size or resolution limit of the images. Moreover, we were limited in the number of tumor and epilepsy cells available at the precision level required for this analysis, and while the classification methods showed improved performance for the filtered data, localized to the soma of each individual neuron, the low number of data points led to more uncertainty in the AUC metrics. While this observation of increased asymmetry at the branching junctions closest to the soma might be a possible biomarker for tumor or epilepsy images, it is necessary to confirm this result by reproducing it with larger datasets. However, even with our relatively small sample of data, our methods using functionally informed structural parameters as features to classify between cells show enormous promise in extracting new information about neurons and glia.

Consequently, our study makes a strong case for collecting more high-precision morphological data across neuronal and glial cell types, applying these methods to larger datasets, using more modern classification methods, and reproducing these results as well as extending them further.

In conclusion, our study combines machine-learning methods with a functionally informed structural model of neuronal and glial processes to not only classify between different types of cells, but to understand the functional basis behind those differences in structure. Although machine-learning is a tool that often obscures mechanistic insight into how models are able to

make predictions, our features—$\bar{\beta}$ and $\Delta\beta$—have specific connections to functional principles related to information flow [23].

We introduce $L_{n,rel}$ as another feature in our model, providing insight into the localization of functionally driven structural differences across neuronal and glial cell types as well as potential disease-related alterations. As more and more data are becoming available using high precision microscopy, such as new electron microscopy datasets by the FlyEM project at Janelia [107, 6], many more opportunities to apply these methods to even larger datasets at higher resolutions and across more cell types will arise. In this paper, we have scratched the surface of attempting to understand the function of glial cells, about which current knowledge is limited, as well as disease-related morphological changes and functional underpinnings of those changes. Our results illustrate the promise of these methods to further tackle these important problems that will help us better understand the basic building blocks of the nervous system.

Chapter 4 is taken from a manuscript that is currently undergoing revisions (and will be submitted to a journal) by the dissertation author, ***Paheli Desai-Chowdhry****, Alexander B Brummer, Samhita Mallavarapu, and Van M Savage. "Information Flow Drives Localized Morphological Differences Across Neuronal and Glial Cell Types." In:* In Preparation *(2023).*

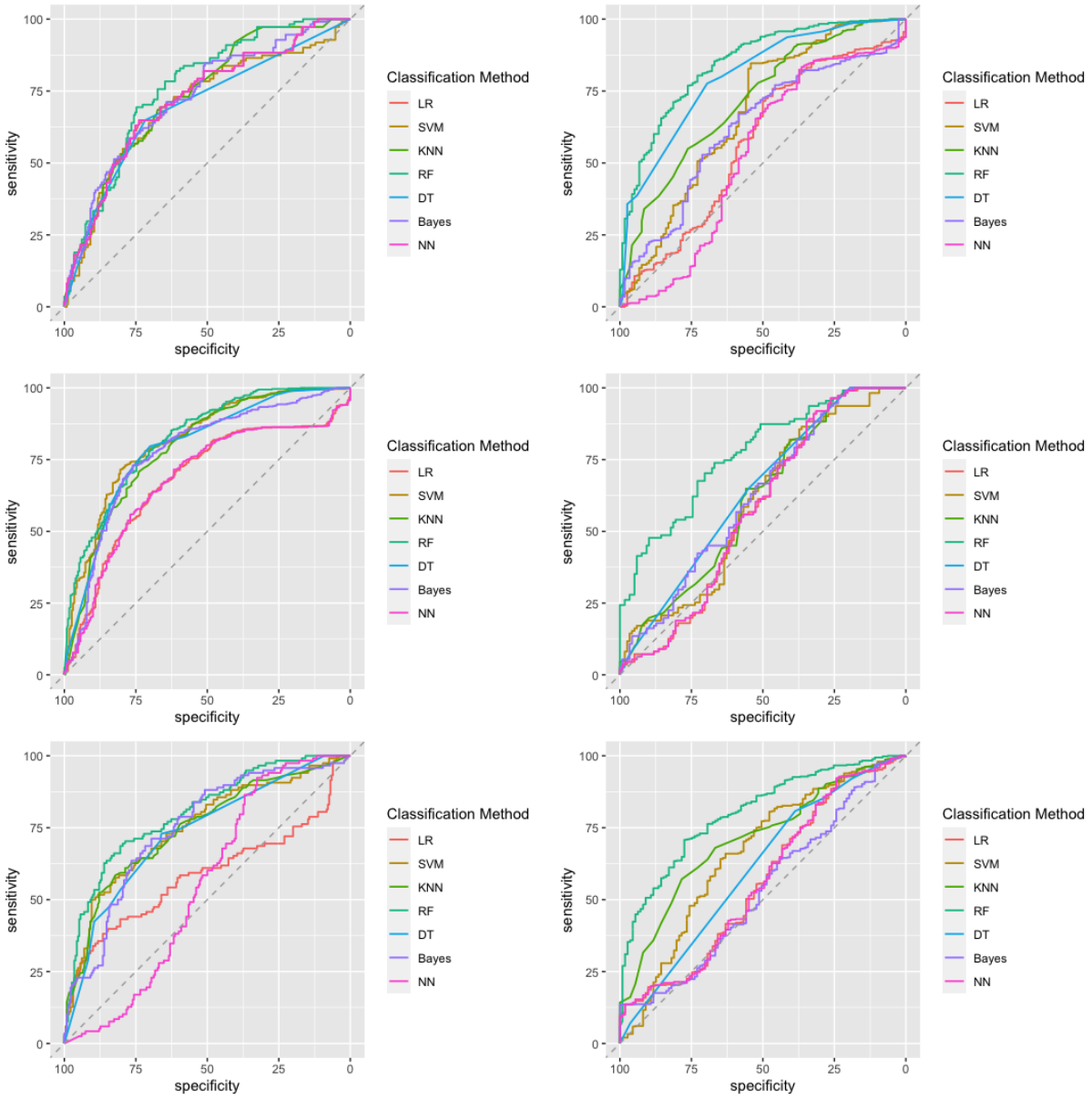

Figure 4.6. Plots of ROC curves for Motoneurons versus Purkinje Cells (upper left), MSNs versus Pyramidal Cells (upper right), Motoneurons versus Pyramidal Cells (middle left), MSNs versus Purkinje Cells (middle right), Motoneurons versus MSNs (lower left), and Purkinje versus Pyramidal Cells (lower right), illustrating the performance of classification methods for 6 different combinations of dendrite cell-type comparisons, using $\bar{\beta}$ and $\Delta\beta$ as features

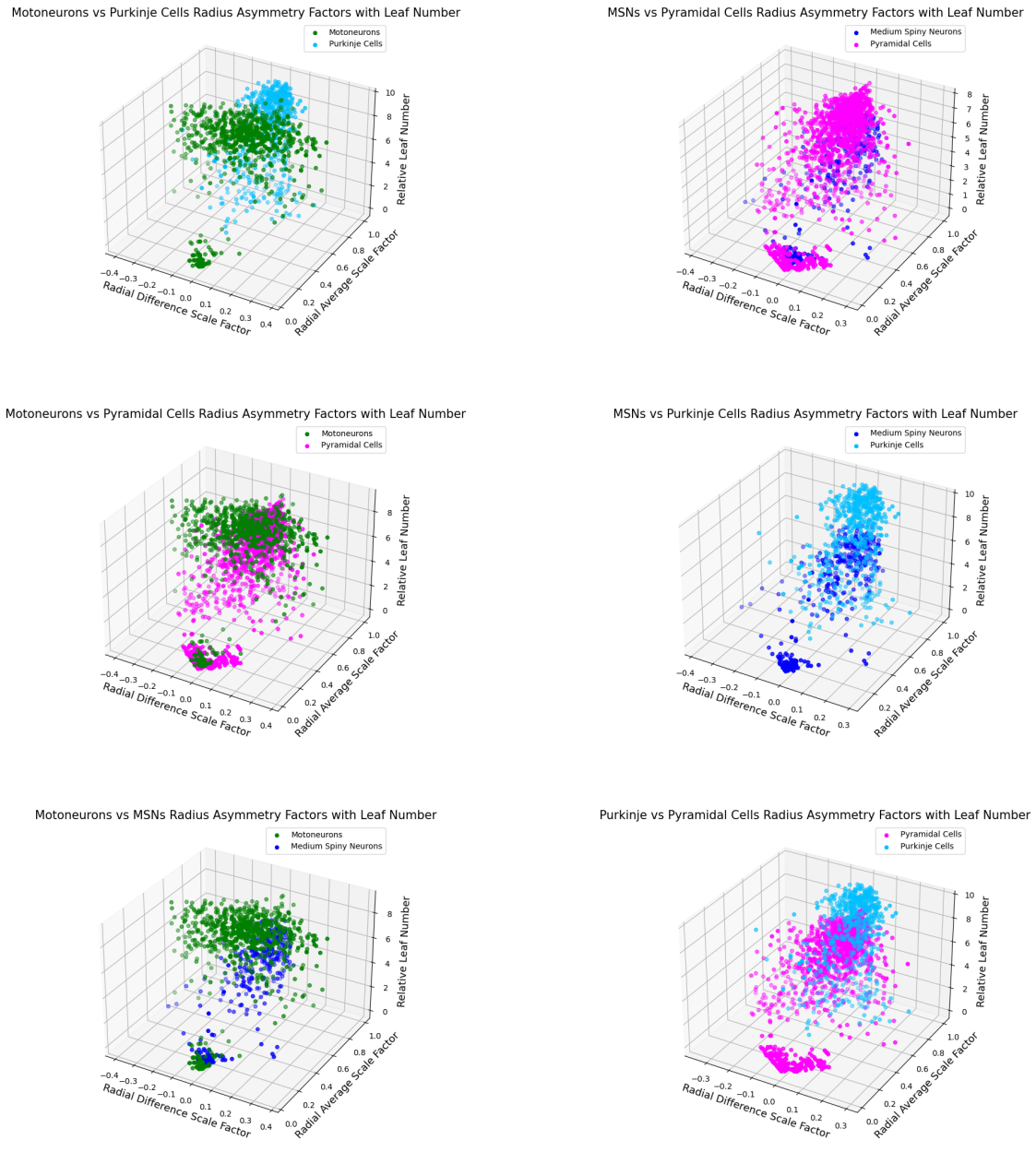

Figure 4.7. Plots of 3-dimensional feature spaces of the training data for 6 different combinations of dendritic types

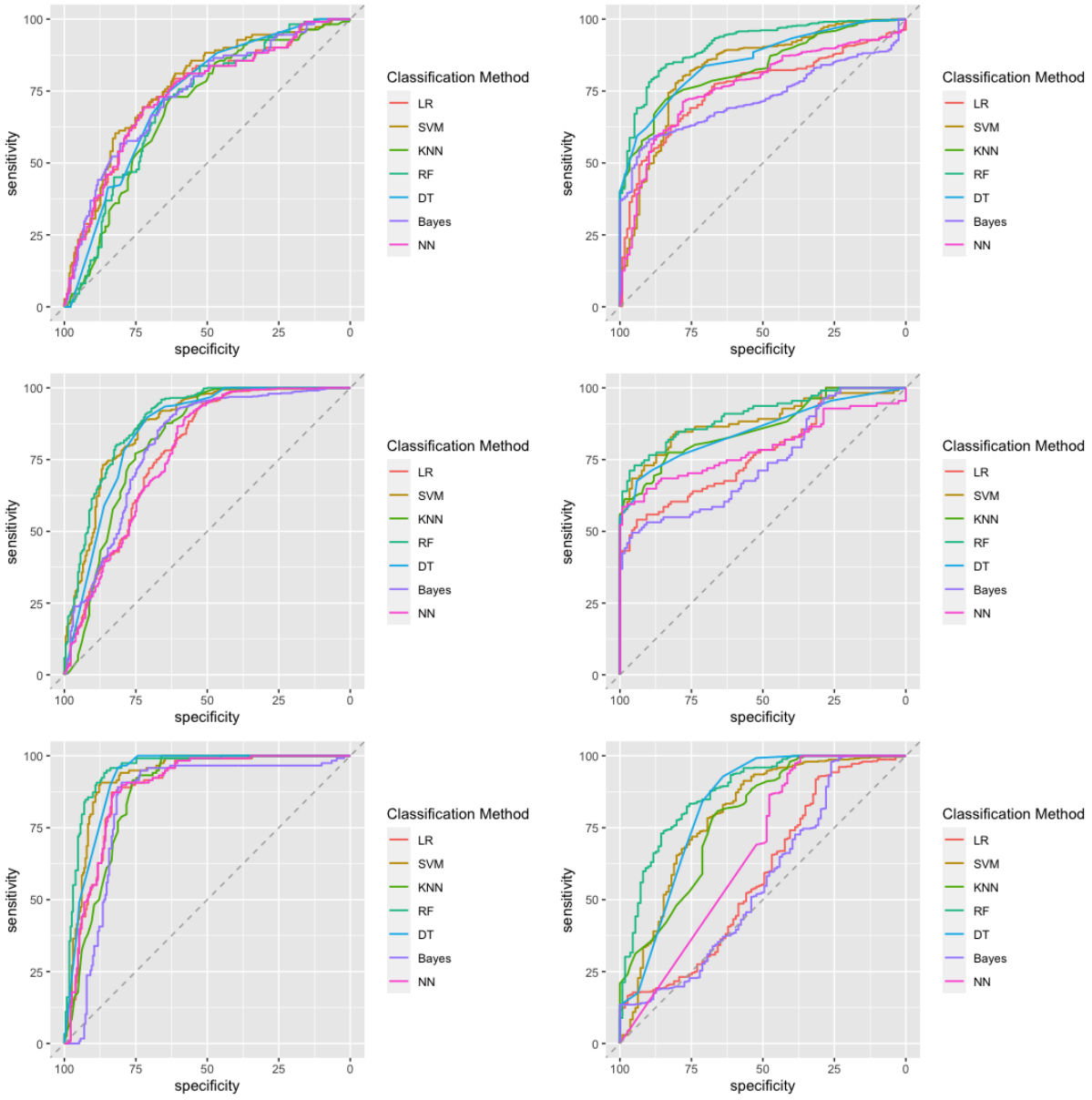

Figure 4.8. Plots of ROC curves for Motoneurons versus Purkinje Cells (upper left), MSNs versus Pyramidal Cells (upper right), Motoneurons versus Pyramidal Cells (middle left), MSNs versus Purkinje Cells (middle right), Motoneurons versus MSNs (lower left), and Purkinje versus Pyramidal Cells (lower right), illustrating the performance of classification methods for 6 different combinations of dendrite cell-type comparisons, using $\bar{\beta}$, $\Delta\beta$, and $L_{n,rel}$ as features

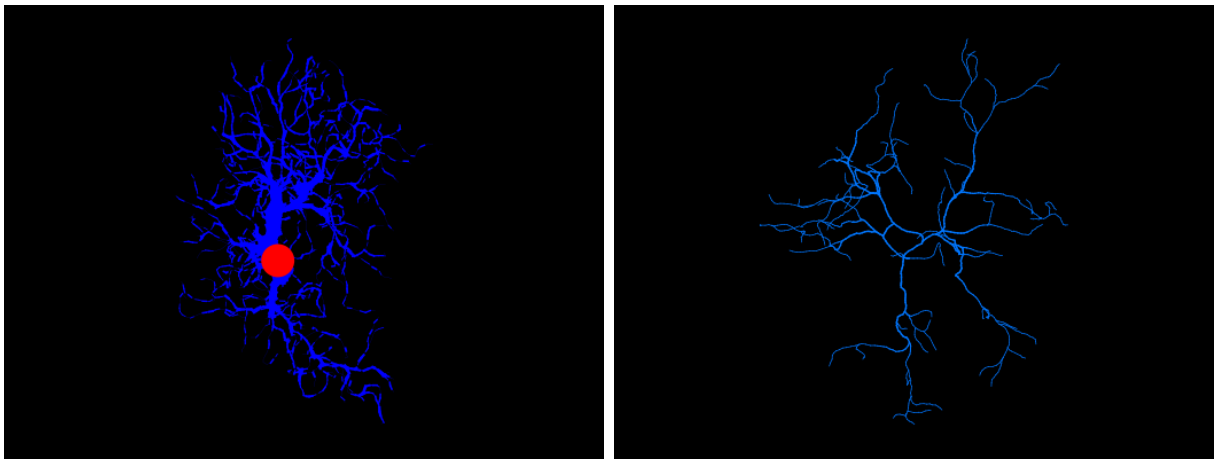

Figure 4.9. Images showing reconstructions of the images and morphological data from NeuroMorpho.Org [10] for different glial cell types including Astrocytes, from a mouse [32] (left) and Microglia, from a mouse [8] (right)

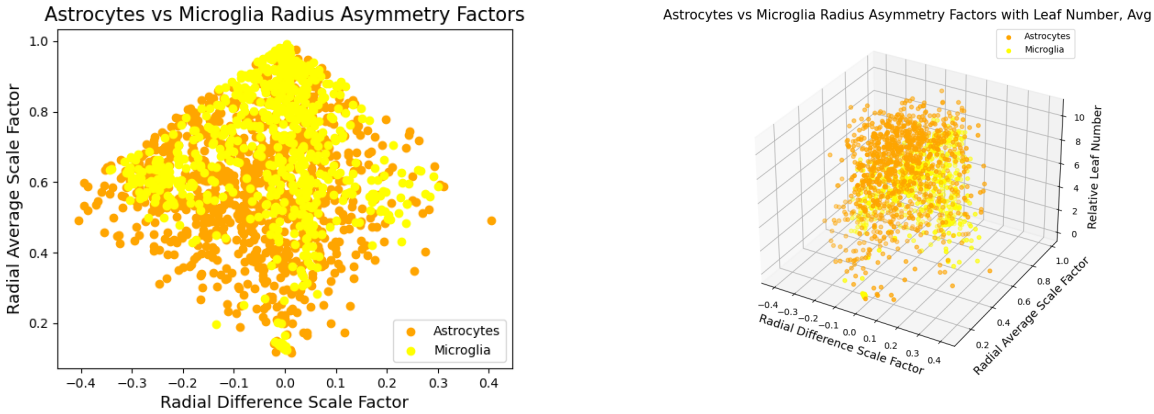

Figure 4.10. Plots of the feature spaces for comparing two different types of glial cells, astrocytes and microglia, using $\bar{\beta}$ and $\Delta\beta$ (left) and $\bar{\beta}$, $\Delta\beta$, and $L_{n,rel}$ (right) as features

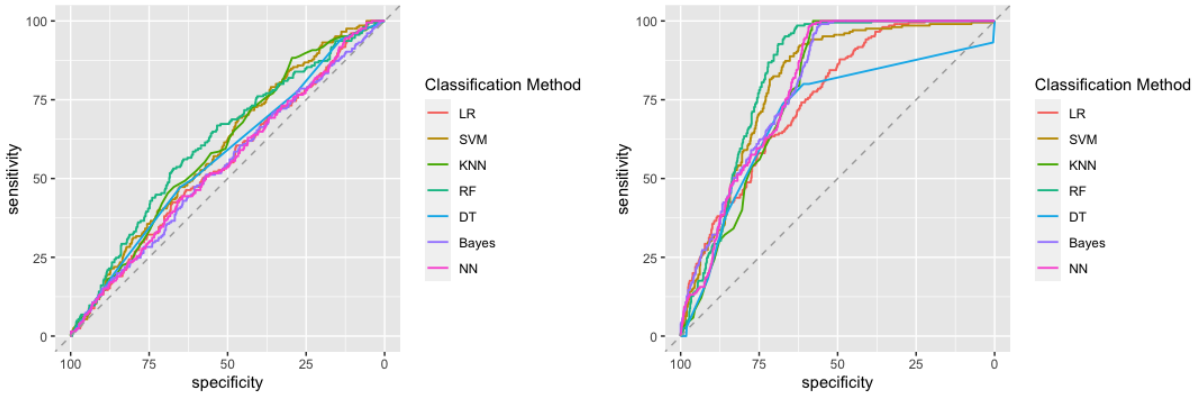

Figure 4.11. Plots of the ROC curves illustrating the performance of classification methods comparing two different types of glial cells—astrocytes and microglia—using $\overline{\beta}$ and $\Delta\beta$ (left) and $\overline{\beta}$, $\Delta\beta$, and $L_{n,rel}$ (right) as features.

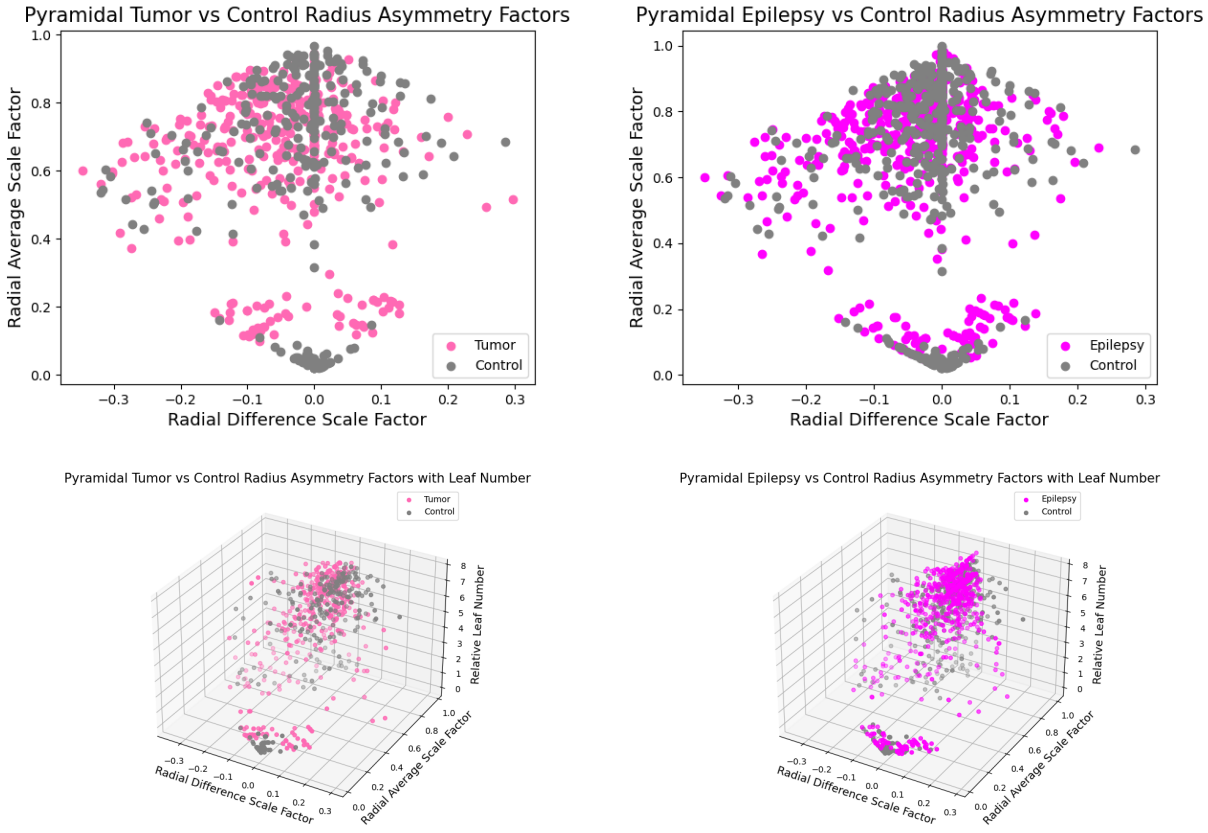

Figure 4.12. Plots of feature spaces showing the comparison of training data for control and diseased cells, tumor and epilepsy cells, with $\overline{\beta}$ and $\Delta\beta$, (top) and $\overline{\beta}$, $\Delta\beta$, and $L_{n,rel}$ (bottom) as features

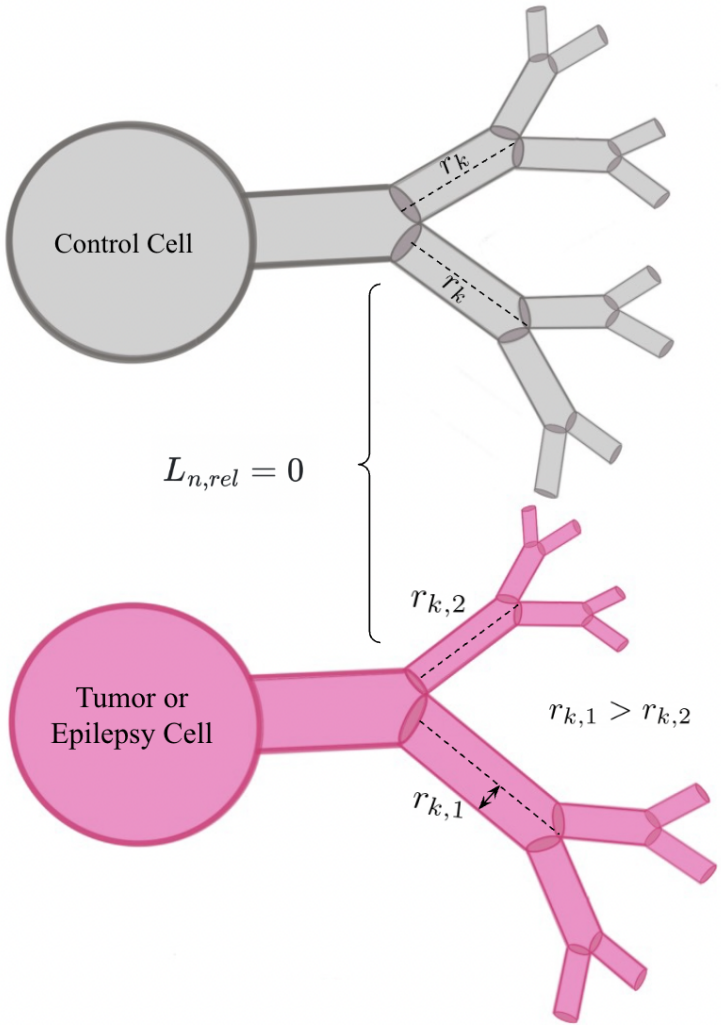

Figure 4.13. Visualization of the observed differences between control and tumor/epilepsy human pyramidal cells

CHAPTER 5

Future Directions and Conclusion

This work accomplishes the development of a unifying model that relates axon and dendrite structure to biophysical function, considering the tradeoff between conduction time delay and power loss minimization, subject to material costs and space-filling constraints. The model parameters can be varied to consider a range of cases that can predict morphological quantities that correspond to different cell-types, and the model can be used to consider symmetric as well as asymmetric branching junctions. The model can be used to extract characteristic features specific to cell-types that are consistent across species, while also being able to predict allometric scaling relationships that illustrate how functional principles vary across species of different sizes. From this theoretical framework, we learn that structural and functional properties in neuron processes vary based on position in the cell relative to the synapses and the soma, and this position, along with parameters related to information flow, can be used as features subjected to machine-learning methods to classify among different types of cells. These features can characterize differences in dendrites, glial cells, and diseased cells.

5.1 Future Directions: Length

Although the parameters related to information flow in our model–$\bar{\beta}$ and $\Delta\beta$—perform relatively well in classifying cell-types, sometimes even in the absence of the third feature, $L_{n,rel}$, the parameters relating to space-filling in our model—$\bar{\gamma}$ and $\Delta\gamma$—do not perform well in classifying cells. One possible explanation for this is that information flow is a

more substantial driving force of the diverse structures across cell types than is space-filling. However, it is more likely that these disparities are due to the fact that our labeling system for branches is insufficient or simply inaccurate for characterizing length scaling relationships, and hence, it will be necessary to adopt an alternate labeling scheme. In Section A.4, we show a distribution of the length scaling ratios for data combined across cell types and species. These data follow an exponential distribution rather than the expected normal distribution that we observe for radius scaling ratios. Similar disparities are observed for cardiovascular and plant networks [85, 23, 18], suggesting that an alternate labeling scheme might prove beneficial. In particular, the Horton-Strahler labeling method, which starts at the tips and increases as two branches fuse to form a junction, has previously been developed for river networks [116], and has also previously been applied to study neurons [120] as well as cardiovascular networks [21] and plant networks [58]. This method takes what they define as a *centripetal* approach to labelling, beginning at the tips, rather than a *centrifugal* approach, beginning at the soma or root. This Horton-Strahler labeling has proven advantageous in studying asymmetric networks and very extensive networks such as those of Purkinje cell dendrites. *Centripetal* labeling methods are said to be more useful for analyzing distal regions of cells, whereas *centrifugal* approaches are more useful for analyzing branches closer to the soma [120]. A promising future direction is applying such alternative labeling schemes to neurons using this method of analysis and attempting to extract more information about length scaling ratios and their connection to the principle of space-filling.

It is likely that space-filling plays an important role in determining the structure of neurons, as the three-dimensional structures of neurons provide them with a computational advantage over electrical circuits, which are planar [64]. However, some neurons, such as Purkinje cells, are planar [109]. Thus, given the differences in the way Purkinje cells fill space compared to other 3-dimensional neurons, such as motoneurons, it is surprising that the length scaling ratios did not separate them when applied as features in classification methods. Moreover, although we built a parameter, d, in the model, to account for differ-

ences in space-filling dimension, this parameter did not affect the prediction of the radius scaling ratios. Since we focused on radius scaling ratios in this analysis, dimension did not end up being a factor in our distinction of cell-type correspondences to theoretical predictions. Further characterization of the length scaling ratios might resolve these inconsistencies. In addition, further development of the space-filling constraint could help account for and integrate different patterns such as tiling and self-avoidance [25, 124]. A possible source of ideas for the mathematical incorporation of different types of space-filling in previous work that has characterized such differences in plants is work by Charles Price and Brian Enquist, which extends the WBE theory to look at scaling and morphology in plants [91]. Another idea is to develop a space-filling constraint that considers interactions between neurons. This might help account for additional features of biological neurons such as activity-dependent plasticity and environmental factors that might shape the growth of neurons [126], particularly in relation to their length.

5.2 Future Directions: Increasing Biological Realism

An interesting finding in our analysis of asymmetric branching in Chapter 3 is the emergence of multiple possible interpretations of the conduction time delay, as there are multiple possible paths between the soma and the synapses. For some predictions, the conduction time delay term or constraint was interpreted as the sum of all paths (thus related to the average path length), and the predictions from these cases agreed most with the empirical data that focus on the most asymmetric junctions. This suggests that it is possible that the whole network—rather than a single maximal or minimal path—is important in characterizing neuronal branching patterns. A possible explanation for this is that these structures are optimized in order to be robust to damage in localized regions. Previous work has found that in leaf-venation networks, the presence of closed loops makes these networks resilient to damage in localized regions [59]. Previous work has also quantified loops in cardiovascular

networks [47]. A possible future direction is attempting to characterize loops in neuronal branching networks, and determine whether they might be an adaptation to increase the robustness of these networks.

In order to further capture the essential features of biological neurons in our model, another potential avenue for the development of our model is incorporating some sort of tapering [51] or measure of curvature. In our model, we assume that the branches are cylindrical and the radius remains constant at each branch until it transitions in level. When analyzing the data, we take an average of the radius values at each branch. This ignores variation that might be important to the function of neurons. Moreover, incorporating cytoskeletal elements into the model might further strengthen its biological realism and provide new insights into the relationship between structure and function [51, 66].

5.3 Future Directions: Numerical Analysis of the Model

So far, we have looked at optimization problems that minimize power and time individually. However, it is possible that there might be intermediate values, and that different cell types might have different relative importance of time and power in determining structure. A goal of our future work is using numerical methods to extend the number of functional principles we consider in each prediction. Here, we will consider our general objective function with volume, mass, and space-filling constraints.

$$C = \alpha P + (1-\alpha)T + \lambda V_{N,TOT} \sum_{k=0}^{N} \left(\prod_{j=k}^{N-1} \left[\beta_{j,1}^2 \gamma_{j,1} + \beta_{j,2}^2 \gamma_{j,2} \right]^{-1} + \lambda_m m_c \right. \\ \left. + \sum_{k=0}^{N} \left(\lambda_k l_{N,TOT}^d \prod_{j=k}^{N-1} \left[\gamma_{j,1}^d + \gamma_{j,2}^d \right]^{-1} \right) \right. \tag{5.1}$$

Here, we can define P as follows:

$$P = R_{N,TOT} \sum_{k=0}^{N} \left(\prod_{j=k}^{N-1} \left[\frac{\beta_{j,1}^2}{\gamma_{j,1}} + \frac{\beta_{j,2}^2}{\gamma_{j,2}} \right] \right) \tag{5.2}$$

We can define T either in terms of the total, average, maximum, or minimum path. The four possible definitions of this term are:

$$T_{TOT} = T_{N,TOT} \sum_{k=0}^{N} \left(\prod_{j=k}^{N-1} \left[\frac{\gamma_{j,1}}{\beta_{j,1}^{\frac{1}{2}+\epsilon}} + \frac{\gamma_{j,2}}{\beta_{j,2}^{\frac{1}{2}+\epsilon}} \right]^{-1} \right) \tag{5.3}$$

$$\bar{T} = T_{N,TOT} \sum_{k=0}^{N} \frac{1}{2^k} \left(\prod_{j=k}^{N-1} \left[\frac{\gamma_{j,1}}{\beta_{j,1}^{\frac{1}{2}+\epsilon}} + \frac{\gamma_{j,2}}{\beta_{j,2}^{\frac{1}{2}+\epsilon}} \right]^{-1} \right) \tag{5.4}$$

$$T_{MAX} = T_{N,TOT} \sum_{k=0}^{N} \left(\prod_{j=k}^{N-1} \left[\frac{\beta_{j,1}^{\frac{1}{2}+\epsilon}}{\gamma_{j,1}} \right] \right) \tag{5.5}$$

$$T_{MIN} = T_{N,TOT} \sum_{k=0}^{N} \left(\prod_{j=k}^{N-1} \left[\frac{\beta_{j,2}^{\frac{1}{2}+\epsilon}}{\gamma_{j,2}} \right] \right) \tag{5.6}$$

In order to estimate the relative importance of the different functional principles, we will use numerical methods to minimize C and estimate the relative weights of these different principles as parameters. One possible way I might do this is using nonlinear regression methods in R such as polynomial regression, which uses the method of least squares minimization. Another way is to use functions from the optimize package in the SciPy library, which makes use of other methods such as the conjugate gradient algorithm. Table 5.1 summarizes the specific goals of this optimization problem.

In these expressions, $\beta_{k,1}$, $\beta_{k,2}$, $\gamma_{k,1}$, and $\gamma_{k,2}$ will be input from the neuron reconstruction data. In each neuron process, there will be N levels, so the input data will be a 4 x N matrix. One possible way to characterize k is using the $L_{n,rel}$ parameter that we defined in Chapter 4. If we define n_k as the number of branches at each level k, we will consider the average values for β_k and γ_k at each branching generation k as follows:

Table 5.1. Summary of Numerical Optimization Problem Specifications

Model	C (Equation 5.1)
Variables and Parameters in the Model	$\beta_{k,1}$, $\beta_{k,2}$, $\gamma_{k,1}$, $\gamma_{k,2}$, N, α, λ, λ_k, $\lambda_m m_c$, ϵ, d
Input Data (Known Variables and Parameters)	$[\beta_{k,1}, \beta_{k,2}, \gamma_{k,1}, \gamma_{k,2}]$ from $k \in 1 : N$
Output (Parameters to be Estimated)	α, λ, λ_k, $\lambda_m m_c$, ϵ, d

$$\bar{\beta_k} = \frac{\sum_{i=1}^{n_k} \beta_i}{n_k} \tag{5.7}$$

$$\bar{\gamma_k} = \frac{\sum_{i=1}^{n_k} \gamma_i}{n_k} \tag{5.8}$$

For each neuron reconstruction, we can minimize this function with the above input from the data and estimate the parameters: α, λ, λ_k, $\lambda_m m_c$, ϵ, and d. The estimation of the specific parameters ϵ, the parameter encoding the presence of myelination, and d, the parameter denoting the dimension of space filling, will likely be proof of concept because for a given type of neuron, we should already have this information from the data. The estimation of the constants that we previously defined as the Lagrange multipliers—λ, λ_k, and λ_m—will tell us about the relative importance of the biophysical constraints. Since the estimates of the cell mass, m_c, is often not readily available with the neuron reconstruction data, we can either estimate it through volume estimates or absorb it into the multiplier estimation as $\lambda_m m_c$. Based on averages in the literature and established concepts in scaling theory, we might estimate this value to extract λ_m. The parameter α will reflect an estimate of the relative importance of time versus power. We were previously only considering α to be equal to either 0 or 1, meaning that power and time minimization are completely separate. However, in biological neurons, it is likely that neuron cell structures are designed to optimize not only conduction speed or energy efficiency, but a relative combination of both.

5.4 Future Directions: Developmental Changes

It is widely understood that the morphology of dendritic arbors is not static, but is constantly modified based on interactions with surrounding neurons and glia, activity, and environmental factors such as chemoattractants and chemorepellants [109, 126]. Incorporating this dynamical aspect of neuron morphology will be useful in future development of our model. It is also interesting to consider the question of whether functional principles change how they influence structure over stages of development and whether these changes are reflected in the scaling ratios.

Another possible avenue of future development of this work is looking at in vivo image data that is taken across timepoints. By applying our machine learning classification methods using $\bar{\beta}$, $\Delta\beta$, and $L_{n,rel}$ as features, we might be able to capture the functional basis behind observed differences across time, such as in response to activity, environmental factors, disease progression, or stages of development. A potential resource for this type of data is fruit fly data from the NeuronBridge website [4].

5.5 Future Directions: Analyzing Images using Angicart++

So far, the data we have looked at has been from existing neuron reconstructions available on NeuroMorpho.Org and Allen Brain Atlas. However, we have run into issues in analyzing this data due to the resolution limits of the images and image reconstructions, particularly for the radius scaling ratios. For the histograms showing the distributions of scaling ratios in the whole range (for the data shown in this thesis, we have truncated the values at or above 1.0), we notice a large peak at 1.0, indicating that after a certain level of the network, the radius measurements are all equal to the pixel size. In addition, the distributions of asymmetric radius scale factors showed diagonal lines that were likely an artifact of the resolution limit of the images and the fact that for smaller processes, the difference scale factors occurred at regular intervals that were multiples of the pixel size. Many existing tools for neuron

reconstructions from images focus more on capturing the path length and connectivity than on radius [37]. Moreover, many of these reconstruction processes require some amount of user intervention. The automated systems that do exist are not general enough to replace manual reconstructions [89].

Previous work in our group has involved the development of a novel software, Angicart++, that allows the extraction of blood vessel radius, length, and connectivity from 3D image stacks using a volumetric approach to measure radius [85]. Due to the structural similarities between branching blood vessels and branching neuron processes, a goal of this work is to analyze 3D image stacks of neuron processes directly and compare the results to those in existing reconstructions. If we are able to replicate or possibly even improve the resolution of the image data, other groups analyzing morphological properties of neurons might be able to utilize this software to improve the efficiency of data processing through automation.

5.6 Future Directions: Additional Cell-Type Classification

While our machine learning classification methods using functionally informed structural quantities was successful in classifying some cell-types, other distinctions were not as obvious. In particular, we attempted to distinguish Medium Spiny Neurons (MSNs) in the Basal Ganglia based on the type of dopamine receptors—D1 or D2—that they express as they are functionally distinct and have different roles in the basal ganglia circuitry [46]. In Appendix C, we illustrate the findings of these classification attempts. Although there might be observable distinctions based on our parameters, we are hindered by the limited amount of data available at the precision and resolution required for our analysis. Upon collecting larger datasets, it might be fruitful to continue to attempt to distinguish these cells.

Additionally, we attempted to distinguish between excitatory and inhibitory cells by lumping them together into two groups from our individual cell types. We elaborate on these

results in Appendix C. Although we are able to observe significant distinctions between the two types, it is unclear whether these distinctions are because of their excitatory or inhibitory properties, or simply because of the distinctions between the cell types that were used in these categories. While distinctions could be observed between individual excitatory and inhibitory pairs, these distinctions were no more or less significant than those observed between pairs of two excitatory or two inhibitory neurons. Incorporation of additional cell types in this analysis that belong to both of these groups might clarify distinctions that are specific to this property.

5.7 Conclusion

Overall, this work lays the foundation for the analysis of the correspondence between neuron morphology and function using biological scaling theory and machine-learning methods. The promise of these results suggests that there is great potential for future studies using larger datasets at higher resolutions and across more species and cell types. In addition to providing useful insights into the structure-function correspondence of neurons, these results are also useful in the context of other studies of biological networks such as cardiovascular networks, plants, and lungs. Although these biological resource distribution networks have very different functions and are at different spatial scales, the ability to apply similar mathematical methods and obtain analogous results suggests that they possess essential and very generic similarities in their properties. That is, it is evidence that argues that these diverse biological systems are unified by a very similar or overlapping set of underlying physical principles.

APPENDIX A

Scaling Ratios and Allometry

A.1 Scaling Ratio Calculation

We use the method of Lagrange multipliers to solve for the values of the scaling ratios for radius and length, $\frac{r_{k+1}}{r_k}$ and $\frac{l_{k+1}}{l_k}$, that minimize the objective function. This is carried out by setting the derivatives of these functions - with respect to radius and length - equal to 0 and solving for the Lagrange multipliers. These values are assumed to be constant, so we solve for the scaling ratios by setting the ratio of the multiplier expressions at successive branching generations equal to 1.

Below, we show a sample calculation of the method of Lagrange multipliers for one of the cases. We will consider the objective function P - the function minimizing power with fixed volume, mass, and space-filling - for our sample calculation. Below is the equation for this function:

$$P = \sum_{k=0}^{N} \frac{l_k}{r_k^2 n^k} + \lambda \sum_{k=0}^{N} n^k r_k^2 l_k + \lambda_m m_c + \sum_{k=0}^{N} \lambda_k n^k l_k^d \tag{A.1}$$

A.1.1 Radius Scaling Ratio Calculation

To find the radius scaling ratio, we will minimize P with respect to r_k, at an arbitrary level k, and set the result equal to 0. Thus, we can find a formula for a Lagrange multiplier and derive the scaling law.

$$\frac{\partial P}{\partial r_k} = \frac{-2l_k}{n^k r_k^3} + 2\lambda n^k r_k l_k = 0 \tag{A.2}$$

Solving for the Lagrange multiplier, we have

$$\lambda = \frac{1}{n^{2k} r_k^4} \tag{A.3}$$

Since this is a constant, the denominator must be constant across levels.

$$\frac{n^{2(k+1)} r_{k+1}^4}{n^{2k} r_k^4} = 1 \tag{A.4}$$

Thus, we can solve for the scaling ratio

$$\frac{r_{k+1}}{r_k} = \left(n^{-2}\right)^{1/4} = n^{-1/2} \tag{A.5}$$

A.1.2 Length Scaling Ratio Calculation

To find the length scaling ratio, we will minimize P with respect to l_k, at an arbitrary level k, and set the result equal to 0. Thus, we can find a formula for a Lagrange multiplier, using the formula above, and derive the scaling law.

$$\frac{\partial P}{\partial l_k} = \frac{1}{n^k r_k^2} + \lambda n^k r_k^2 + d\lambda_k n^k l_k^{d-1} = 0 \tag{A.6}$$

Solving for the Lagrange multiplier, we have

$$\lambda_k = \frac{-\frac{1}{n^k r_k^2} - \lambda n^k r_k^2}{d n^k l_k^{d-1}} \tag{A.7}$$

Substituting λ, as calculated before, we can simplify the expression for this multiplier as follows

$$\lambda_k = \frac{-\frac{1}{n^k r_k^2} - \frac{1}{n^k r_k^2}}{d n^k l_k^{d-1}} = -\frac{2}{d n^{2k} l_k^{d-1} r_k^2} \tag{A.8}$$

Since this is a constant, the denominator must be constant across levels, so

$$\frac{n^{2(k+1)} l_{k+1}^{d-1} r_{k+1}^2}{n^{2k} l_k^{d-1} r_k^2} = 1 \tag{A.9}$$

Thus, substituting in the scaling ratio for radius, we can solve for the scaling ratio for length

$$\left(\frac{l_{k+1}}{l_k}\right)^{d-1} = n^{-2} \left(\frac{r_{k+1}}{r_k}\right)^{-2} \tag{A.10}$$

$$\left(\frac{l_{k+1}}{l_k}\right)^{d-1} = n^{-2} \left(n^{-1/2}\right)^{-2} = n^{-1} \tag{A.11}$$

For the case where the dimension of space-filling, d, is equal to 3, we have

$$\frac{l_{k+1}}{l_k} = n^{-1/2} \tag{A.12}$$

This method is repeated to solve for the theoretical predictions of scaling ratios for radius and length for the other objective functions.

A.2 Allometry Calculation

We can use the objective function P^* - the function minimizing power with fixed time delay, size, and space-filling - to derive a functional scaling relationship between conduction time

delay and species mass, considering the unmyelinated case where ϵ is equal to 0, and the case of 3-dimensional space-filling, choosing d to be 3. The equation for this function is

$$P^* = \sum_{k=0}^{N} \frac{l_k}{r_k^2 n^k} + \lambda \sum_{k=0}^{N} \frac{l_k}{r_k^{\frac{1}{2}}} + \lambda_m m_c + \sum_{k=0}^{N} \lambda_k n^k l_k^3 \tag{A.13}$$

We begin by setting the derivative of the function with respect to radius equal to zero to solve for the multiplier λ.

$$\frac{\partial P^*}{\partial r_k} = \frac{-2l_k}{r_k^3 n^k} - \frac{\lambda l_k r_k^{-3/2}}{2} = 0 \tag{A.14}$$

Below, we have the expression for the multiplier

$$\lambda = \frac{-4}{r_k^{3/2} n^k} \tag{A.15}$$

We can similarly solve for the multiplier λ_k by setting the derivative with respect to length equal to 0.

$$\frac{\partial P^*}{\partial l_k} = \frac{1}{r_k^2 n^k} + \lambda r_k^{-1/2} + 3\lambda_k n^k l_k^2 = 0 \tag{A.16}$$

Using the expression for λ above, we can solve for an expression for λ_k.

$$\lambda_k = \frac{1}{r_k^2 n^{2k} l_k^2} \tag{A.17}$$

If we plug this expression for λ_k back into the original expression for P^*, we get

$$P^* = \sum_{k=0}^{N} \frac{l_k}{r_k^2 n^k} + \lambda \sum_{k=0}^{N} \frac{l_k}{r_k^{1/2}} + \lambda_m m_c + \sum_{k=0}^{N} \left(\frac{1}{r_k^2 n^{2k} l_k^2} \right) n^k l_k^3 \tag{A.18}$$

The last term simplifies to a term that is identical in form to the power term. So we can rewrite this as

$$P^* = 2\sum_{k=0}^{N} \frac{l_k}{r_k^2 n^k} + \lambda \sum_{k=0}^{N} \frac{l_k}{r_k^{1/2}} + \lambda_m m_c \tag{A.19}$$

For simplicity, if we denote the power expression as P, the time delay expression as T, we can rewrite this as

$$P^* = 2P + \lambda T + \lambda_m m_c \tag{A.20}$$

Previous results have shown a proportional relationship between m_c, the mass of a single neuron, and the fourth root of an animal's body mass, $M^{1/4}$ [104]. Thus, we can replace this term and consider a new Lagrange multiplier with the absorbed constant

$$P^* = 2P + \lambda T + \lambda_M M^{1/4} \tag{A.21}$$

We will now take the derivative of this term with respect to M, the mass of the species, and set it equal 0.

$$\frac{\partial P^*}{\partial M} = 2\frac{\partial P}{\partial M} + \lambda \frac{\partial T}{\partial M} + \lambda_M \frac{\partial M^{1/4}}{\partial M} = 0 \tag{A.22}$$

Previous results have shown that the energetic cost, which we have interpreted here as power loss due to dissipation, decreases with increasing body weight of animals at a linear rate [121]. Thus, we can express $\frac{\partial P}{\partial M}$ generally as a negative constant, $-C$. We can rewrite the above expression as

$$\frac{\partial T}{\partial M} = \frac{-\lambda_M M^{-3/4}}{4\lambda} + 2\frac{C}{\lambda} \tag{A.23}$$

Solving this differential equation, we have

$$T = \frac{-\lambda_M}{\lambda} M^{1/4} + \frac{2C}{\lambda} M + C_0 \tag{A.24}$$

If we apply the initial condition T=0 for M =0, we get $C_0 = 0$. Thus, we obtain the following expression relating conduction time delay and body mass

$$T = \frac{-\lambda_M}{\lambda} M^{1/4} + \frac{2C}{\lambda} M \tag{A.25}$$

A.3 Allometric Scaling Relationship Regression Analysis

Our calculations have led to the following allometric relationship between conduction time delay and species mass

$$T = \frac{-\lambda_M}{\lambda} M^{1/4} + \frac{2C}{\lambda} M \tag{A.26}$$

Note that the function for conduction time delay is a linear combination of two terms. The first term depends on the $\frac{1}{4}$-power of the body mass and the second term depends linearly on the body mass.

In order to test the fit of this model to the data, we will run a regression analysis on the following linear model

$$T = \beta_0 + \beta_1 M + \beta_2 M^{1/4} \tag{A.27}$$

Here, β_0, β_1, and β_2 are the estimated coefficients. This will allow us to estimate the magnitude of each of these coefficients and the relative importance of each term in determining the conduction time, based on data.

Below is a summary of the results

Table A.1. Regression Coefficients

	Estimate	Standard Error	t value	Pr($>|t|$)
(Intercept)	-4.79	3.20	-1.50	0.172
M	0.00132	0.00326	0.408	0.694
$M^{1/4}$	9.40	1.66	5.66	0.000478

Estimated coefficients for each term in a linear model fitting conduction time delay to M and $M^{1/4}$ shows the relative weight of each of the terms in the model as well as the likelihood that the relationship between the term and conduction time delay is purely by chance. The notation Pr($>|t|$) represents the p-values, or the probability that the correlation observed is due to random variation.

These results suggest that the $M^{1/4}$ term dominates in terms of magnitude, as its coefficient, 9.40, is higher than the coefficient for the linear mass (M) term that is 0.00132. Moreover, the Pr($>|t|$) or p-values suggest that the $M^{1/4}$ term is the only term that is not likely to be due to random chance.

A.4 Length Scaling Ratio Distributions for Dendrites and Axons

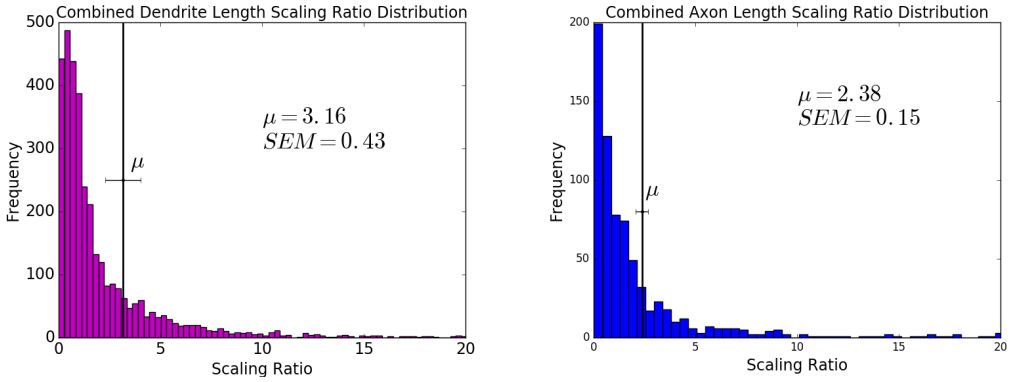

Figure A.1. Length Scaling Ratio Distributions Histograms showing the distributions of length scaling ratios for dendrites and axons in a range of species, brain regions, and cell types available on NeuroMorpho.Org. The mean dendrite scaling ratio is 3.16 ± 0.43 and the mean axon scaling ratio is 2.38 ± 0.15. In the figure, μ represents the mean and SEM represents the standard error of the mean. The standard deviations of the distributions are 25.10 for dendrites and 4.07 for axons. The black solid lines denote the mean in the distributions, shown with error bars. We zoomed in to the window to look at values between 0 and 20, although the mean is calculated from additional data beyond this point. The exponential distributions observed for length scaling ratios observed here reflect the distributions observed in the length scaling ratios for cardiovascular networks.

APPENDIX B

Asymmetry Calculations

In Table 3.1, we show a series of results calculated from specific cases of the general cost function in Equation 3.1. Here, we will show the calculations of these results in more detail.

B.1 Power Minimization with Fixed Volume

The simplest case for this type of calculation is the optimization of a cost function that minimizes power lost due to dissipation ($\alpha = 1$ in Equation 3.1) with a material cost constraint. We have represented the material cost constraint here as the total network volume, and this is a quantity that we hold to be fixed in the optimization.

The specific function we are minimizing here is:

$$P_{TOT} = I_0^2 R_{N,TOT} \sum_{k=0}^{N} \left(\prod_{j=k}^{N-1} \left[\frac{\beta_{j,1}^2}{\gamma_{j,1}} + \frac{\beta_{j,2}^2}{\gamma_{j,2}} \right] \right) + \lambda V_{N,TOT} \sum_{k=0}^{N} \left(\prod_{j=k}^{N-1} \left[\beta_{j,1}^2 \gamma_{j,1} + \beta_{j,2}^2 \gamma_{j,2} \right]^{-1} \right) + \lambda_m m_c + \sum_{k=0}^{N} \left(\lambda_k l_{N,TOT}^d \prod_{j=k}^{N-1} \left[\gamma_{j,1}^d + \gamma_{j,2}^d \right]^{-1} \right) \tag{B.1}$$

We begin the optimization by taking the derivative of the function with respect to $\beta_{i,1}$ and $\beta_{i,2}$ and setting them equal to 0.

$$\frac{\partial P_{TOT}}{\partial \beta_{i,1}} = \sum_{k=0}^{N} \left(\frac{2I_0^2 R_{N,TOT}\beta_{i,1}}{\gamma_{i,1}} \prod_{j=k,j\neq i}^{N-1} \left[\frac{\beta_{j,1}^2}{\gamma_{j,1}} + \frac{\beta_{j,2}^2}{\gamma_{j,2}} \right] - \frac{2\lambda V_{N,TOT}\beta_{i,1}\gamma_{i,1}}{\beta_{i,1}^2\gamma_{i,1} + \beta_{i,2}^2\gamma_{i,2}} \prod_{j=k,j\neq i}^{N-1} \left[\beta_{j,1}^2\gamma_{j,1} + \beta_{j,2}^2\gamma_{j,2} \right]^{-1} \right) \tag{B.2}$$

$$\frac{\partial P_{TOT}}{\partial \beta_{i,2}} = \sum_{k=0}^{N} \left(\frac{2I_0^2 R_{N,TOT}\beta_{i,2}}{\gamma_{i,2}} \prod_{j=k,j\neq i}^{N-1} \left[\frac{\beta_{j,1}^2}{\gamma_{j,1}} + \frac{\beta_{j,2}^2}{\gamma_{j,2}} \right] - \frac{2\lambda V_{N,TOT}\beta_{i,2}\gamma_{i,2}}{\beta_{i,1}^2\gamma_{i,1} + \beta_{i,2}^2\gamma_{i,2}} \prod_{j=k,j\neq i}^{N-1} \left[\beta_{j,1}^2\gamma_{j,1} + \beta_{j,2}^2\gamma_{j,2} \right]^{-1} \right) \tag{B.3}$$

Since both of these equations, B.2 and B.3, are equal to 0, we can simplify this expression by adding a linear combination of these equations, which is also equal to 0. We will multiply B.2 by $\beta_{i,1}$ and multiply B.3 by $\beta_{i,2}$, arriving at the following expression.

$$0 = \sum_{k=0}^{N} \left(2I_0^2 R_{N,TOT} \prod_{j=k}^{N-1} \left[\frac{\beta_{j,1}^2}{\gamma_{j,1}} + \frac{\beta_{j,2}^2}{\gamma_{j,2}} \right] - 2\lambda V_{N,TOT} \prod_{j=k}^{N-1} \left[\beta_{j,1}^2\gamma_{j,1} + \beta_{j,2}^2\gamma_{j,2} \right]^{-1} \right) \tag{B.4}$$

Since all of these terms are positive biological quantities and because the sum of the terms is equal to 0, then each of the individual terms in the sum must be equal to zero. Using this fact, we can solve for an expression for λ.

$$\lambda = \frac{I_0^2 R_{N,TOT}}{V_{N,TOT}} \prod_{j=k}^{N-1} \left[\beta_{j,1}^2\gamma_{j,1} + \beta_{j,2}^2\gamma_{j,2} \right] \left[\frac{\beta_{j,1}^2}{\gamma_{j,1}} + \frac{\beta_{j,2}^2}{\gamma_{j,2}} \right] \tag{B.5}$$

If we plug this expression for λ back into B.2, we can simplify the expression to the following:

$$\gamma_{i,1} = \gamma_{i,2} \tag{B.6}$$

Now, using the fact that λ is a constant and thus stays the same across generations; that is, $\lambda_k = \lambda_{k+1}$, we arrive at the following expression:

$$\left[\beta_{k,1}^2\gamma_{k,1} + \beta_{k,2}^2\gamma_{k,2} \right] \left[\frac{\beta_{k,1}^2}{\gamma_{k,1}} + \frac{\beta_{k,2}^2}{\gamma_{k,2}} \right] = 1 \tag{B.7}$$

Substituting B.6 in B.7 and simplifying, we arrive at

$$\beta_{k,1}^2 + \beta_{k,2}^2 = 1 \tag{B.8}$$

That is, the two scaling ratios are raised to a scaling exponent of 2. Note that in this case, we can rewrite the equation by expanding $\beta_{k,1}$ and $\beta_{k,2}$ based on their definitions, $\beta_{k,1} = \frac{r_{k+1,1}}{r_k}$ and $\beta_{k,2} = \frac{r_{k+1,2}}{r_k}$.

$$\left(\frac{r_{k+1,1}}{r_k}\right)^2 + \left(\frac{r_{k+1,2}}{r_k}\right)^2 = 1 \tag{B.9}$$

This leads to the following relationship between the radii:

$$r_{k+1,1}^2 + r_{k+1,2}^2 = r_k^2 \tag{B.10}$$

Note that this implies that the sum of the cross-sectional areas of the two daughter branches is equal to the cross-sectional area of the parent branch (scaling this equation by π would give this relationship). This implies that our scaling exponent relationship is **area-preserving** in this case. There is an analogous area-preserving case observed in studies of cardiovascular branching blood vessels [103].

B.2 Time Minimization, Umyelinated

The calculations involving optimization of conduction time delay are more complicated because in an asymmetric branching network, there are multiple possible paths from the soma to the synapses. Thus, different interpretations correspond to different optimization problems.

B.2.1 Average Path Interpretation

For the average interpretation, the idea is that for a bifurcating branching network, there is an average time at each level, divided by the total number of branches, 2^k. (This can be generalized for other types of networks with branching ratio n as n^k). Thus, we can define the function we are optimizing as follows:

$$T = T_{TOT} \sum_{k=0}^{N} \frac{1}{2^k} \left(\prod_{j=k}^{N-1} \left[\frac{\gamma_{j,1}}{\beta_{j,1}^{1/2}} + \frac{\gamma_{j,2}}{\beta_{j,2}^{1/2}} \right] \right) + \lambda V_{N,TOT} \sum_{k=0}^{N} \left(\prod_{j=k}^{N-1} \left[\beta_{j,1}^2 \gamma_{j,1} + \beta_{j,2}^2 \gamma_{j,2} \right]^{-1} \right) + \lambda_m m_c + \sum_{k=0}^{N} \left(\lambda_k l_{N,TOT}^d \prod_{j=k}^{N-1} \left[\gamma_{j,1}^d + \gamma_{j,2}^d \right]^{-1} \right) \tag{B.11}$$

Following the same steps for the optimization as in section B.1, we arrive at

$$\beta_{k,1}^{5/2} + \beta_{k,2}^{5/2} = 1 \tag{B.12}$$

That is, the two scaling ratios are raised to a scaling exponent of 5/2. As we saw before, we can rewrite this relationship as follows.

$$r_{k+1,1}^{5/2} + r_{k+1,2}^{5/2} = r_k^{5/2} \tag{B.13}$$

While the previous case was area-preserving, this case is **area-increasing**.

B.2.2 Maximum/Minimum Path Interpretation

For both the maximum and minimum path interpretations of conduction time delay, we focus on just one of the β values, the larger one, β_1 corresponding to the minimum time delay path (as the velocity is the greatest) and the smaller one, β_2 for maximum time delay path (as the velocity is the smallest). For simplicity, we will focus on the calculation minimizing the

conduction time delay of the optimal path using β_1, as the calculations are mathematically equivalent.

Thus, we can define the function we are optimizing as follows:

$$T = T_{TOT} \sum_{k=0}^{N} \left(\prod_{j=k}^{N-1} \frac{\gamma_{j,1}}{\beta_{j,1}^{1/2}} \right) + \lambda V_{N,TOT} \sum_{k=0}^{N} \left(\prod_{j=k}^{N-1} \left[\beta_{j,1}^2 \gamma_{j,1} + \beta_{j,2}^2 \gamma_{j,2} \right]^{-1} \right) + \lambda_m m_c + \sum_{k=0}^{N} \left(\lambda_k l_{N,TOT}^d \prod_{j=k}^{N-1} \left[\gamma_{j,1}^d + \gamma_{j,2}^d \right]^{-1} \right) \tag{B.14}$$

Note that here, since we are focusing on β_1, corresponding to the maximum velocity or the minimum conduction time delay, we are minimizing the minimum path here. We take the derivative of the function with respect to $\beta_{i,1}$ and $\beta_{i,2}$ and set them equal to 0.

$$\frac{\partial T}{\partial \beta_{i,1}} = \sum_{k=0}^{N} \left(\frac{T_{TOT}}{2} \frac{\beta_{i,1}^{-1/2}}{\gamma_{i,1}} \prod_{j=k, j\neq i}^{N-1} \frac{\beta_{j,1}^{1/2}}{\gamma_{j,1}} - \frac{2\lambda V_{N,TOT} \beta_{i,1} \gamma_{i,1}}{\beta_{i,1}^2 \gamma_{i,1} + \beta_{i,2}^2 \gamma_{i,2}} \prod_{j=k, j\neq i}^{N-1} \left[\beta_{j,1}^2 \gamma_{j,1} + \beta_{j,2}^2 \gamma_{j,2} \right]^{-1} \right) \tag{B.15}$$

$$\frac{\partial T}{\partial \beta_{i,1}} = -\frac{2\lambda V_{N,TOT} \beta_{i,2} \gamma_{i,2}}{\beta_{i,1}^2 \gamma_{i,1} + \beta_{i,2}^2 \gamma_{i,2}} \prod_{j=k, j\neq i}^{N-1} \left[\beta_{j,1}^2 \gamma_{j,1} + \beta_{j,2}^2 \gamma_{j,2} \right]^{-1} \Bigg) \tag{B.16}$$

Note that since $\beta_{i,2}$ does not appear in the conduction time delay term being minimized, the first term disappears when taking the derivative with respect to $\beta_{i,2}$. As before, since both of these equations, B.15 and B.16, are equal to 0, we can simplify this expression by adding a linear combination of these equations, which is also equal to 0. We will multiply B.15 by $\beta_{i,1}$ and multiply B.16 by $\beta_{i,2}$, arriving at the following expression.

$$0 = \sum_{k=0}^{N} \left(\frac{T_{TOT}}{2} \prod_{j=k}^{N-1} \frac{\beta_{j,1}^{1/2}}{\gamma_{j,1}} - 2\lambda V_{N,TOT} \prod_{j=k}^{N-1} \left[\beta_{j,1}^2 \gamma_{j,1} + \beta_{j,2}^2 \gamma_{j,2} \right]^{-1} \right) \tag{B.17}$$

As before, we can solve for an expression for λ.

$$\lambda = \frac{T_{TOT}}{4 V_{N,TOT}} \prod_{j=k}^{N-1} \frac{\beta_{j,1}^{1/2}}{\gamma_{j,1}} \left[\frac{\beta_{j,1}^2}{\gamma_{j,1}} + \frac{\beta_{j,2}^2}{\gamma_{j,2}} \right] \tag{B.18}$$

If we plug this expression for λ back into B.15, we can simplify the expression to the following:

$$\beta_{i,2}^2 \gamma_{i,2} = 0 \tag{B.19}$$

Now, using the fact that λ is a constant and thus stays the same across generations; that is, $\lambda_k = \lambda_{k+1}$, we arrive at the following expression:

$$\frac{\beta_{k,1}^{1/2}}{\gamma_{k,1}} \left[\beta_{k,1}^2 \gamma_{k,1} + \beta_{k,2}^2 \gamma_{k,2} \right] = 1 \tag{B.20}$$

By substituting B.19 in B.20 and simplifying, we arrive at

$$\beta_{k,1}^{5/2} = 1 \tag{B.21}$$

Here, we find that the scaling exponent, which only applies to β_1, is 5/2. Repeating this calculation with β_2, focusing on the maximum path, would yield the equation $\beta_{k,2}^{5/2} = 1$. As above, substituting the expressions for the scaling ratios, we can rewrite this as

$$r_{k+1,1}^{5/2} = r_k^{5/2} \tag{B.22}$$

This is for the minimum path calculation. Analogously, if we focus on the maximum path, we can write this equation as $r_{k+1,1}^{5/2} = r_k^{5/2}$. For either case, focusing on the relationship between the parent and the selected daughter branch, we see that the relationship is **area-increasing**.

B.3 Time Minimization, Myelinated

Here, we repeat the above calculations for the myelinated case, where the velocity is proportional to the radius of each branch rather than the square root of the radius. Thus, we

begin with a similar function but with different powers for β in the conduction time delay term.

B.3.1 Average Path Interpretation

As above, for the average interpretation, by the total number of branches, 2^k. Thus, we can define the function we are optimizing as follows:

$$T = T_{TOT}\sum_{k=0}^{N}\frac{1}{2^k}\left(\prod_{j=k}^{N-1}\left[\frac{\gamma_{j,1}}{\beta_{j,1}}+\frac{\gamma_{j,2}}{\beta_{j,2}}\right]\right)+\lambda V_{N,TOT}\sum_{k=0}^{N}\left(\prod_{j=k}^{N-1}\left[\beta_{j,1}^2\gamma_{j,1}+\beta_{j,2}^2\gamma_{j,2}\right]^{-1}\right) \\ +\lambda_m m_c+\sum_{k=0}^{N}\left(\lambda_k l_{N,TOT}^d\prod_{j=k}^{N-1}\left[\gamma_{j,1}^d+\gamma_{j,2}^d\right]^{-1}\right) \tag{B.23}$$

Following the same steps for the optimization as in sections B.1 and and B.2, we arrive at

$$\beta_{k,1}^3+\beta_{k,2}^3=1 \tag{B.24}$$

That is, the two scaling ratios are raised to a scaling exponent of 3, and this relationship is **area-increasing**. Note that this is the same as the area-increasing relationship pretended for branching blood vessels [103].

B.3.2 Maximum/Minimum Path Interpretation

As before, we optimize the function focusing on the path calculated with the larger scaling ratio, β_1, corresponding to the path of minimum conduction time delay.

The function we are optimizing for the myelinated case is as follows:

$$T = T_{TOT} \sum_{k=0}^{N} \left(\prod_{j=k}^{N-1} \frac{\gamma_{j,1}}{\beta_{j,1}} \right) + \lambda V_{N,TOT} \sum_{k=0}^{N} \left(\prod_{j=k}^{N-1} \left[\beta_{j,1}^2 \gamma_{j,1} + \beta_{j,2}^2 \gamma_{j,2} \right]^{-1} \right) + \lambda_m m_c + \sum_{k=0}^{N} \left(\lambda_k l_{N,TOT}^d \prod_{j=k}^{N-1} \left[\gamma_{j,1}^d + \gamma_{j,2}^d \right]^{-1} \right) \tag{B.25}$$

Following the same steps for the optimization as in sections B.1 and B.2, we arrive at

$$\beta_{k,1}^3 = 1 \tag{B.26}$$

Here, we find that the scaling exponent, which only applies to β_1, is 3, for the minimum path. Repeating this calculation with β_2 would yield the equation $\beta_{k,2}^3 = 1$ for the maximum path. As before, this relationship is **area-increasing**.

B.4 Power Minimization with Fixed Time Delay

Here, we repeat these calculations for the case where the constraint is conduction time delay rather than volume.

B.4.1 Total Paths Interpretation

For the total paths interpretation of the conduction time delay, we are optimizing the following function:

$$P^* = I_0^2 R_{N,TOT} \sum_{k=0}^{N} \left(\prod_{j=k}^{N-1} \left[\frac{\beta_{j,1}^2}{\gamma_{j,1}} + \frac{\beta_{j,2}^2}{\gamma_{j,2}} \right] \right) - \lambda T_{TOT} \sum_{k=0}^{N} \left(\prod_{j=k}^{N-1} \left[\frac{\gamma_{j,1}}{\beta_{j,1}^{1/2}} + \frac{\gamma_{j,2}}{\beta_{j,2}^{1/2}} \right] \right) + \lambda_m m_c + \sum_{k=0}^{N} \left(\lambda_k l_{N,TOT}^d \prod_{j=k}^{N-1} \left[\gamma_{j,1}^d + \gamma_{j,2}^d \right]^{-1} \right) \tag{B.27}$$

Note that the sign of the constraint function is arbitrary, so we use the negative one to simplify the calculation. We begin the optimization by taking the derivative of the function

with respect to $\beta_{i,1}$ and $\beta_{i,2}$ and setting them equal to 0.

$$\frac{\partial P^*}{\partial \beta_{i,1}} = \sum_{k=0}^{N} \left(\frac{2I_0^2 R_{N,TOT} \beta_{i,1}}{\gamma_{i,1}} \prod_{j=k, j\neq i}^{N-1} \left[\frac{\beta_{j,1}^2}{\gamma_{j,1}} + \frac{\beta_{j,2}^2}{\gamma_{j,2}} \right] - \frac{T_{TOT}\gamma_{i,1}}{2\beta_{i,1}^{3/2} \left[\frac{\gamma_{j,1}}{\beta_{j,1}} + \frac{\gamma_{j,2}}{\beta_{j,2}} \right]^2} \prod_{j=k, j\neq i}^{N-1} \left[\frac{\gamma_{j,1}}{\beta_{j,1}^{1/2}} + \frac{\gamma_{j,2}}{\beta_{j,2}^{1/2}} \right]^{-1} \right) \tag{B.28}$$

$$\frac{\partial P^*}{\partial \beta_{i,2}} = \sum_{k=0}^{N} \left(\frac{2I_0^2 R_{N,TOT} \beta_{i,2}}{\gamma_{i,2}} \prod_{j=k, j\neq i}^{N-1} \left[\frac{\beta_{j,1}^2}{\gamma_{j,1}} + \frac{\beta_{j,2}^2}{\gamma_{j,2}} \right] - \frac{T_{TOT}\gamma_{i,2}}{2\beta_{i,2}^{3/2} \left[\frac{\gamma_{j,1}}{\beta_{j,1}} + \frac{\gamma_{j,2}}{\beta_{j,2}} \right]^2} \prod_{j=k, j\neq i}^{N-1} \left[\frac{\gamma_{j,1}}{\beta_{j,1}^{1/2}} + \frac{\gamma_{j,2}}{\beta_{j,2}^{1/2}} \right]^{-1} \right) \tag{B.29}$$

Since both of these equations, B.28 and B.29, are equal to 0, we can simplify this expression by adding a linear combination of these equations, which is also equal to 0. We will multiply B.28 by $\beta_{i,1}$ and multiply B.29 by $\beta_{i,2}$, arriving at the following expression.

$$0 = \sum_{k=0}^{N} \left(2I_0^2 R_{N,TOT} \prod_{j=k}^{N-1} \left[\frac{\beta_{j,1}^2}{\gamma_{j,1}} + \frac{\beta_{j,2}^2}{\gamma_{j,2}} \right] - \lambda \frac{T_{TOT}}{2} \prod_{j=k, j\neq i}^{N-1} \left[\frac{\gamma_{j,1}}{\beta_{j,1}^{1/2}} + \frac{\gamma_{j,2}}{\beta_{j,2}^{1/2}} \right]^{-1} \right) \tag{B.30}$$

Since all of these terms are positive biological quantities and because the sum of the terms is equal to 0, then each of the individual terms in the sum must be equal to zero. Using this fact, we can solve for an expression for λ.

$$\lambda = \frac{-4I_0^2 R_{N,TOT}}{T_{TOT}} \prod_{j=k}^{N-1} \left[\frac{\beta_{j,1}^2}{\gamma_{j,1}} + \frac{\beta_{j,2}^2}{\gamma_{j,2}} \right] \left[\frac{\gamma_{j,1}}{\beta_{j,1}^{1/2}} + \frac{\gamma_{j,2}}{\beta_{j,2}^{1/2}} \right] \tag{B.31}$$

If we plug this expression for λ back into B.28, we can simplify the expression to the following:

$$\frac{\gamma_{i,1}}{\gamma_{i,2}} = \frac{\beta_{i,1}^{5/4}}{\beta_{i,2}^{5/4}} \tag{B.32}$$

Now, using the fact that λ is a constant and thus stays the same across generations; that is, $\lambda_k = \lambda_{k+1}$, we arrive at the following expression:

$$\beta_{k,1}^{3/2} + \frac{\beta_{k,1}^2}{\beta_{k,2}^{1/2}}\left[\frac{\gamma_{k,2}}{\gamma_{k,1}}\right] + \frac{\beta_{k,2}^2}{\beta_{k,1}^{1/2}}\left[\frac{\gamma_{i,1}}{\gamma_{i,2}}\right] + \beta_{k,2}^{3/2} = 1 \tag{B.33}$$

Substituting B.32 in B.33, simplifying, and factoring, we arrive at

$$\beta_{k,1}^{3/4} + \beta_{k,2}^{3/4} = 1 \tag{B.34}$$

That is, the two scaling ratios are raised to a scaling exponent of 3/4. As before, we can also represent this expression as

$$r_{k+1,1}^{3/4} + r_{k+1,2}^{3/4} = r_k^{3/4} \tag{B.35}$$

Note that this relationship, unlike the others mentioned above, is **area-decreasing**, as this scaling exponent is less than 2 and the sum of the cross-sectional areas of the daughter branches is less than the cross-sectional area of the parent.

B.4.2 Maximum/Minimum Path Interpretation

For the maximum/minimum interpretation of the conduction time delay constraint, we are optimizing the following function, focusing on β_1 (minimum path):

$$\begin{aligned} P^* = I_0^2 R_{N,TOT} \sum_{k=0}^{N} \left(\prod_{j=k}^{N-1} \left[\frac{\beta_{j,1}^2}{\gamma_{j,1}} + \frac{\beta_{j,2}^2}{\gamma_{j,2}} \right] \right) - \lambda T_{TOT} \sum_{k=0}^{N} \left(\prod_{j=k}^{N-1} \frac{\beta_{j,1}^{1/2}}{\gamma_{j,1}} \right) \\ + \lambda_m m_c + \sum_{k=0}^{N} \left(\lambda_k l_{N,TOT}^d \prod_{j=k}^{N-1} \left[\gamma_{j,1}^d + \gamma_{j,2}^d \right]^{-1} \right) \end{aligned} \tag{B.36}$$

Following the same steps for the optimization as in sections B.1, B.2, and B.3, we arrive at

$$\beta_{k,1}^{3/2} = 1 \tag{B.37}$$

Here, we find that the scaling exponent, which only applies to β_1, is 3/2. Repeating this calculation with β_2 for the maximum path would yield the equation $\beta_{k,2}^{3/2} = 1$. Note that this exponent is different than the exponent calculated for the total path interpretation of time delay, which is different from the previous cases that minimize conduction time delay. We can rewrite this expression as

$$r_{k+1,1}^{3/2} = r_k^{3/2} \tag{B.38}$$

An analogous expression can be written for the maximum path length calculation, with $r_{k+1,2}^{3/2} = r_k^{3/2}$. Focusing on just the relationship between one daughter and the parent branch, this relationship is **area-decreasing**. However, given that the radius of the second daughter does not affect this relationship, is it possible that it is in fact area-preserving or increasing.

APPENDIX C

Cell-Type Classification: Excitatory vs Inhibitory Neurons and D1 vs D2-expressing Medium Spiny Neurons

While our machine learning classification methods using functionally informed structural quantities was successful in classifying some cell-types, they were not as successful for others. Here, we highlight two areas of potential future investigation, where the results from our analysis were not conclusive.

C.1 Excitatory vs Inhibitory Neurons

Neurons connect to one another at the synapses, and the neuron receiving input from another neuron is referred to as the postsynaptic cell. Synapses are excitatory if the increase the likelihood of that the postsynaptic cell will generate an action potential, and inhibitory if they decrease this likelihood. Neurotransmitters bind to ion channel receptors on the postsynaptic cell, and the type of channel determines whether the synapse is excitatory or inhibitory [92]. Glutamate is a common example of an excitatory neurotransmitter, and GABA (γ-Aminobutyric acid) is a common example of an inhibitory synapse. An important factor contributing to the circuitry in the brain is the excitatory/inhibitory balance; networks are constantly adapting and changing their connectivity in order to maintain this balance [82]. To this end, we aim to examine whether there are any morphological differences that we can pinpoint between excitatory and inhibitory neurons.

Purkinje cells and Medium Spiny Neurons (MSNs) are inhibitory, whereas motoneurons and pyramidal cells are excitatory. Thus, we lumped together excitatory and inhibitory cells and attempted to classify between them.

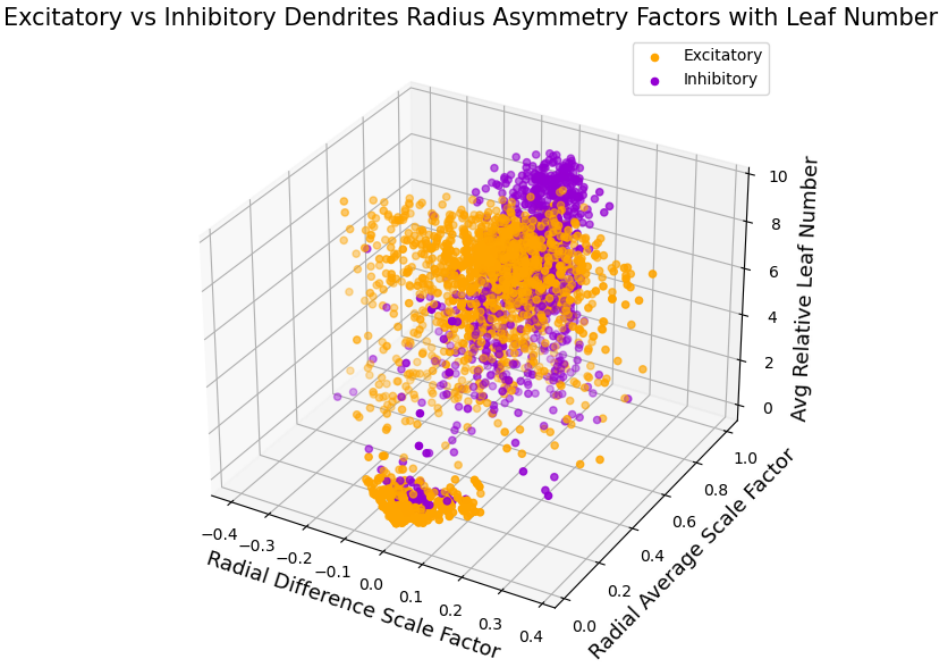

Figure C.1. Excitatory vs Inhibitory Cells Feature Space

Table C.1. Exhibitory vs Inhibitory Neurons AUC (Area Under ROC curve) Measures

Metric/Method	LR	SVM	KNN	RF	DT	Bayes	NN
AUC	0.610 ±0.42	0.747 ±0.035	0.725 ±0.37	0.792 ±0.031	0.727 ±0.036	0.565 ±0.044	0.573 ±0.044

While we were able to observe significant distinctions between the two types, it is unclear whether these distinctions are because of their excitatory or inhibitory properties, or simply because of the distinctions between the cell types. While distinctions could be observed

between individual excitatory and inhibitory pairs, these distinctions were no more or less significant than those observed between pairs of two excitatory or two inhibitory neurons. Incorporation of additional cell types in this analysis that belong to both of these groups might clarify distinctions that are specific to this property.

C.2 D1 vs D2-expressing Medium Spiny Neurons

In addition to examining differences among broad cell-type categories based on the types of receptors they expressed, we attempted to distinguish Medium Spiny Neurons (MSNs) in the Basal Ganglia based on the type of dopamine receptors they express, D1 or D2, as they are functionally distinct and have different roles in the basal ganglia circuitry [46]. We did this classification for the 2D and 3D feature spaces in the raw data as well as image-based classification using the maximum and average leaf numbers per cell.

Table C.2. D1- vs D2-expressing Medium Spiny Neurons Classification AUC (Area Under ROC curve) Measures

Features/Method	LR	SVM	KNN	RF	DT	Bayes	NN
$\bar{\beta}, \boldsymbol{\Delta}\beta$	0.557 ±0.107	0.571 ±0.107	0.578 ±0.104	0.524 ±0.108	0.536 ±0.107	0.538 ±0.106	0.528 ±0.106
$\bar{\beta}, \boldsymbol{\Delta}\beta, L_{n,rel}$	0.552 ±0.106	0.579 ±0.103	0.462 ±0.104	0.500 ±0.105	0.593 ±0.102	0.587 ±0.103	0.578 ±0.104
$\bar{\beta}, \boldsymbol{\Delta}\beta, L_{n,max}$	0.813 ±0.260	0.813 ±0.287	0.688 ±0.343	0.813 ±0.287	0.750 ±0.298	0.938 ±0.118	0.500 ±0.000
$\bar{\beta}, \boldsymbol{\Delta}\beta, L_{n,avg}$	0.750 ±0.325	0.938 ±0.118	0.375 ±0.381	0.688 ±0.374	0.750 ±0.097	0.875 ±0.204	0.875 ±0.204

Although there might be observable distinctions based on our parameters, specifically for the image based data, we are limited by the limited amount of data available at the precision

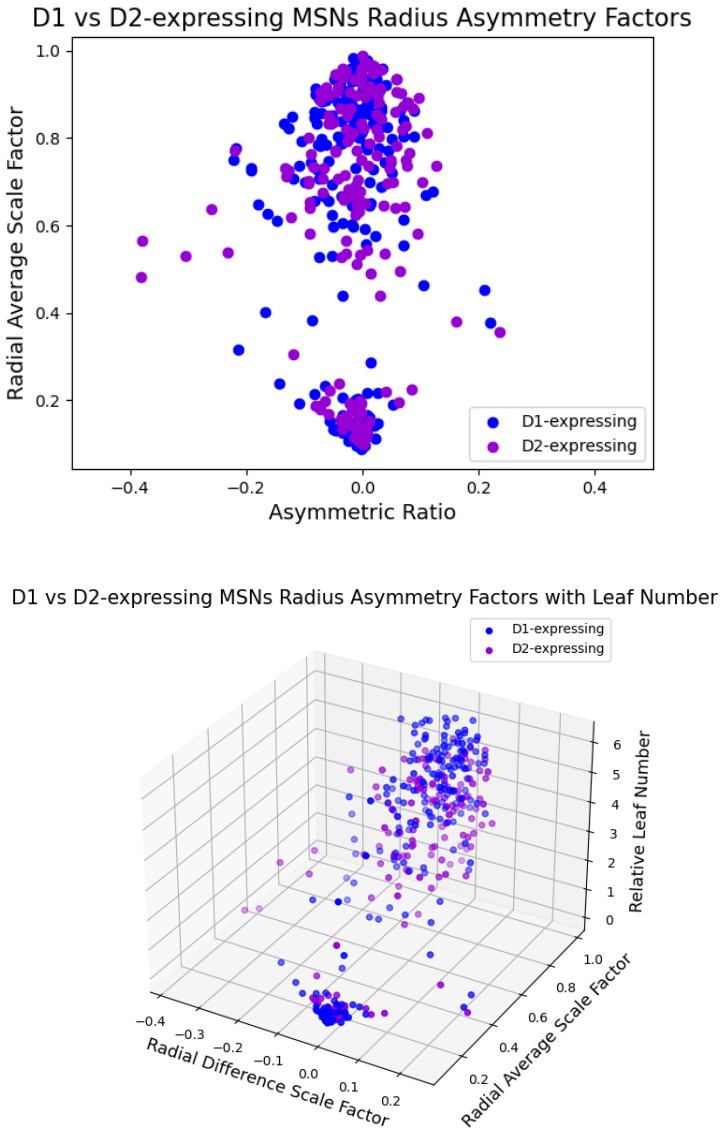

Figure C.2. D1 versus D2 MSN 2D and 3D Feature Spaces, Raw Data

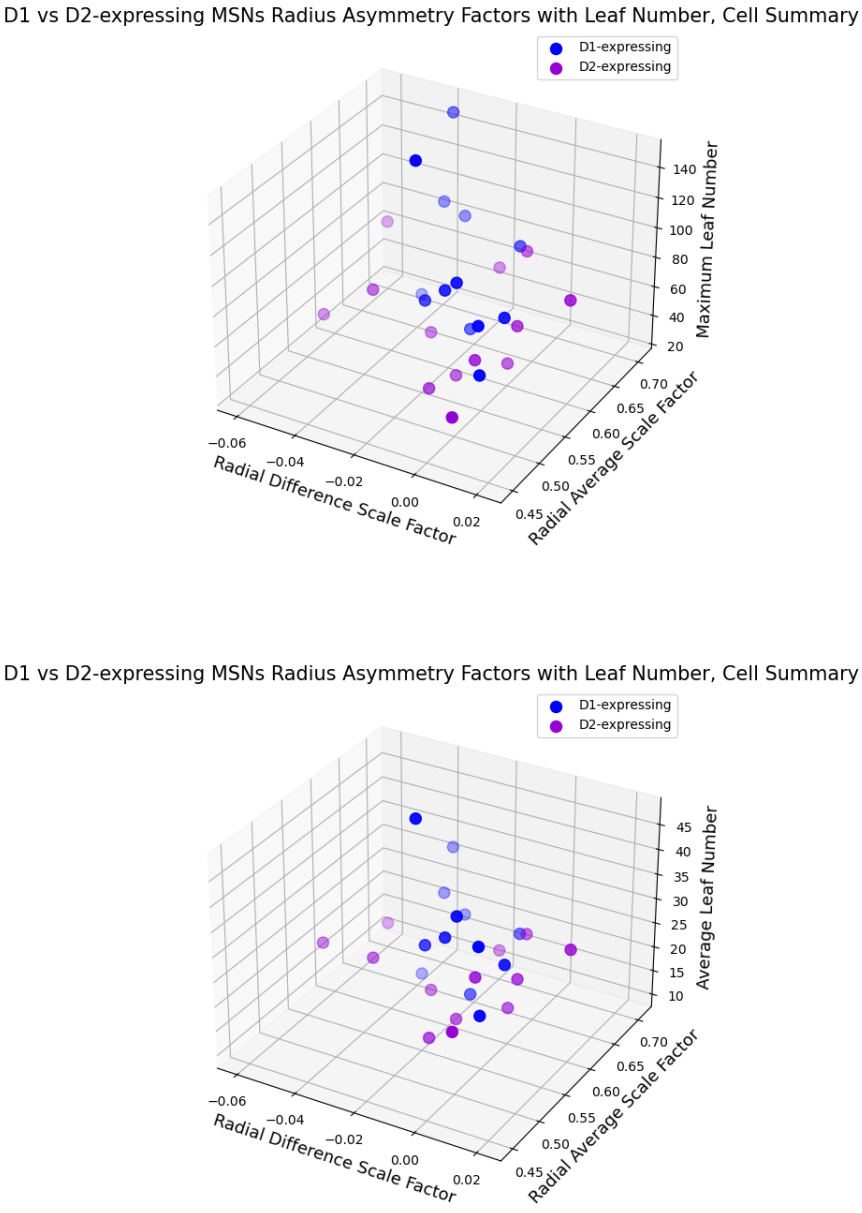

Figure C.3. D1 versus D2 MSN, Image-based Cell Summary Data with Maximum and Average Leaf Numbers

required for this analysis. As we can see, the uncertainty for the AUC measures are high. Upon collecting larger datasets, it might be fruitful to continue to attempt to distinguish these cells.

APPENDIX D

Data Availability

Here, we detail the sources of data we used from NeuroMorpho.Org [10], including the file names of the cells we analyzed, the cell type, region, species, and archive from which the data were taken.

Tables D.1-D.5 are the data sources used for Chapters 2 and 3. Table D.1 details the sources of data for the Golgi cell dendrites. Table D.2 details the sources of data for the Purkinje cell dendrites. Table D.3 details the sources of data for the Motoneuron dendrites. Table D.4 details the sources of data for the axons. Table D.5 details the sources of data for the Peripheral Nervous System dendrites.

Tables D.6 - D.15 are the data sources used for Chapter 4. Table D.6 details the sources of data for axons. Table D.7 details the sources of data for Astrocytes. Table D.8 details the sources of data for Microglia. Table D.9 details the sources of data for Motoneurons. Table D.10 details the sources of data for Purkinje Cells. Table D.11 details the sources of data for D1-expressing Medium Spiny Neurons. Table D.12 details the sources of data for the D2-expressing Medium Spiny Neurons. Table D.13 details the sources of data for Control Pyramidal Cells. Table D.14 details the sources of data for Tumor Pyramidal Cells. Table D.15 details the sources of data for Epilepsy Pyramidal Cells.

The code used to analyze this data can be accessed at the GitHub repository:

https://github.com/pahelidc/scalingtheoryneurons

Table D.1. Data Sources for Golgi Cells

Cell Type	Region	Species	Archive Name	File Name
Golgi cells	Cerebellum	*Giraffa*	Jacobs	185-4-4dw
Golgi cells	Cerebellum	*Giraffa*	Jacobs	186-4-7dw
Golgi cells	Cerebellum	*Giraffa*	Jacobs	187-4-1dw
Golgi cells	Cerebellum	*Homo Sapiens*	Jacobs	189-1-21dw
Golgi cells	Cerebellum	*Homo Sapiens*	Jacobs	189-1-25dw
Golgi cells	Cerebellum	*Homo Sapiens*	Jacobs	189-1-29dw
Golgi cells	Cerebellum	*Loxodonta africana*	Jacobs	155-1-2Gol
Golgi cells	Cerebellum	*Loxodonta africana*	Jacobs	155-2-6Gol
Golgi cells	Cerebellum	*Loxodonta africana*	Jacobs	155-4-5Gol
Golgi cells	Cerebellum	*Megaptera novaeangliae*	Jacobs	202-2-18nj
Golgi cells	Cerebellum	*Megaptera novaeangliae*	Jacobs	202-2-21nj
Golgi cells	Cerebellum	*Megaptera novaeangliae*	Jacobs	202-2-44nj
Golgi cells	Cerebellum	*Neofelis nebulosa*	Jacobs	195-4-8nj
Golgi cells	Cerebellum	*Pan troglodytes*	Jacobs	205-2-16nj
Golgi cells	Cerebellum	*Pan troglodytes*	Jacobs	205-2-21nj
Golgi cells	Cerebellum	*Pan troglodytes*	Jacobs	205-2-31nj
Golgi cells	Cerebellum	*Panthera tigris*	Jacobs	194-4-19nj
Golgi cells	Cerebellum	*Panthera tigris*	Jacobs	194-4-22nj
Golgi cells	Cerebellum	*Panthera tigris*	Jacobs	194-4-4nj
Golgi cells	Cerebellum	*Mus musculus*	Vervaeke	210710C0
Golgi cells	Cerebellum	*Mus musculus*	Vervaeke	240710C0
Golgi cells	Cerebellum	*Mus musculus*	Vervaeke	Golgi-cell-051108-C0-cell1

Table D.2. Data Sources for Purkinje Cells

Cell Type	Region	Species	Archive Name	File Name
Purkinje cells	Cerebellum	*Cavia porcellus*	Dendritica	v_e_purk1
Purkinje cells	Cerebellum	*Cavia porcellus*	Dendritica	v_e_purk2
Purkinje cells	Cerebellum	*Cavia porcellus*	Dendritica	v_e_purk3
Purkinje cells	Cerebellum	*Mus musculus*	Hess	180524_E4_KO
Purkinje cells	Cerebellum	*Mus musculus*	Dusart	Purkinje-slice-ageP35-1
Purkinje cells	Cerebellum	*Mus musculus*	DeMunter	SDM_Purkinje_WT3
Purkinje cells	Cerebellum	*Mus musculus*	Martone	e1cb4a5
Purkinje cells	Cerebellum	*Rattus*	Buffo	1-2-2_18
Purkinje cells	Cerebellum	*Rattus*	Buffo	1-2-8_6
Purkinje cells	Cerebellum	*Rattus*	Martone	alxP
Purkinje cells	Cerebellum	*Rattus*	Dendritica	p19
Purkinje cells	Cerebellum	*Rattus*	Dendritica	p20

Table D.3. Data Sources for Motoneurons

Cell Type	Region	Species	Archive Name	File Name
Motoneurons	Spinal Cord	*Danio rerio*	Morsch	1_180107_mnx1_mVenus_ taken160715
Motoneurons	Spinal Cord	*Danio rerio*	Morsch	2_180107_mnx1_mKO2CX_ taken160808
Motoneurons	Spinal Cord	*Danio rerio*	Morrice	NeuronStudio_VehicleControl _48hpf1
Motoneurons	Spinal Cord	*Felis Catus*	Burke	v_e_moto1
Motoneurons	Spinal Cord	*Felis Catus*	Burke	v_e_moto4
Motoneurons	Spinal Cord	*Felis Catus*	Burke	v_e_moto5
Motoneurons	Spinal Cord	*Mus musculus*	Leroy	04-04-MN9
Motoneurons	Spinal Cord	*Mus musculus*	Leroy	06-04-MN4
Motoneurons	Spinal Cord	*Mus musculus*	Leroy	06-09-MN
Motoneurons	Spinal Cord	*Oryctolagus cuniculus*	Quinian	KQa11-12-2015-tracing
Motoneurons	Spinal Cord	*Oryctolagus cuniculus*	Quinian	KQa29-3-2016$_3$60
Motoneurons	Spinal Cord	*Oryctolagus cuniculus*	Quinian	KQa8-4-2016-tracing
Motoneurons	Spinal Cord	*Rattus*	Alvarez	Alvarez-Control-Cell-2
Motoneurons	Spinal Cord	*Rattus*	Alvarez	Alvarez-Control-Cell-3
Motoneurons	Spinal Cord	*Rattus*	Alvarez	Alvarez-Regen-Cell-4
Motoneurons	Spinal Cord	*Testudines*	Chmykhova	2T-CMOT
Motoneurons	Spinal Cord	*Testudines*	Chmykhova	5Tmn1
Motoneurons	Spinal Cord	*Testudines*	Chmykhova	5Tmn2

Table D.4. Data Sources for Axons

Cell Type	Region	Species	Archive Name	File Name
Target-Selective Descending	Ventral Nerve Cord	*Anisoptera*	Peng	C150
Target-Selective Descending	Ventral Nerve Cord	*Anisoptera*	Peng	C168
Target-Selective Descending	Ventral Nerve Cord	*Anisoptera*	Peng	C201
Columnar	Optic Lobe	*Brachyura*	Bengochea	Me-LoP_columnar_Type1_3
Columnar	Optic Lobe	*Brachyura*	Bengochea	Me-LoP_columnar_Type1_5
Columnar	Optic Lobe	*Brachyura*	Bengochea	Me-LoP_columnar_Type2_3
Uniglomerular projection	Antennal lobe	*Drosophila melanogaster*	Jefferis	12070404c1
Uniglomerular projection	Antennal lobe	*Drosophila melanogaster*	Jefferis	CT12T2
Uniglomerular projection	Antennal lobe	*Drosophila melanogaster*	Jefferis	LHC6R
Shepherd's crook neuron	Mesencephalon	*Gallus gallus domesticus*	Marin	IMc
Shepherd's crook neuron	Mesencephalon	*Gallus gallus domesticus*	Marin	IPc
Shepherd's crook neuron	Mesencephalon	*Gallus gallus domesticus*	Marin	ShCr_Soma
Undefined	Neocortex	*Rattus*	Almeida	cm-ctx-e
Undefined	Neocortex	*Rattus*	Almeida	cm-ctx-f
Undefined	Neocortex	*Rattus*	Almeida	ctr-ctx-3-b

Table D.5. Data Sources for Peripheral Nervous System Neurons

Cell Type	Region	Species	Archive Name	File Name
Dendritic arborization	Peripheral Nervous System	*Drosophila melanogaster*	Ye	021804-2b_ddaC-3 -cd8_ch00
Dendritic arborization	Peripheral Nervous System	*Drosophila melanogaster*	Ascoli,Cox	11CL-IVxAnk2IR _ddaC
Dendritic arborization	Peripheral Nervous System	*Drosophila melanogaster*	Bellemer	36775-3
Sensory	Peripheral Nervous System	*Mus musculus*	Canavesi	control-contact-2
Sensory	Peripheral Nervous System	*Mus musculus*	Canavesi	control-noncontact-1
Sensory	Peripheral Nervous System	*Mus musculus*	Canavesi	diabetic-contact-4
Sensory	Peripheral Nervous System	*Mus musculus*	Yorek	image002
Sensory	Peripheral Nervous System	*Mus musculus*	Yorek	image008
Sensory	Peripheral Nervous System	*Mus musculus*	Yorek	image025_1
Somatic	Peripheral Nervous System	*Mus musculus*	Badea	Badea2012Fig6A -C-R
Somatic	Peripheral Nervous System	*Mus musculus*	Badea	Badea2012Fig6B
Somatic	Peripheral Nervous System	*Mus musculus*	Badea	Badea2012Fig6E -I-R
Touch receptor	Peripheral Nervous System	*Mus musculus*	Lumpkin	01-09-TD4
Touch receptor	Peripheral Nervous System	*Mus musculus*	Lumpkin	1-09-TD1-v3
Touch receptor	Peripheral Nervous System	*Mus musculus*	Lumpkin	1-09-TD4-v2

Table D.6. Data Sources for Axons - Machine Learning Classification

Cell Type	Region	Species	Archive Name	File Name
sensory	Peripheral Nervous System	mouse	Badea	Badea2012Fig6A-C-L
sensory	Peripheral Nervous System	mouse	Badea	Badea2012Fig6A-C-R
sensory	Peripheral Nervous System	mouse	Badea	Badea2012Fig6B
sensory	Peripheral Nervous System	mouse	Badea	Badea2012Fig6E-I-L
sensory	Peripheral Nervous System	mouse	Badea	Badea2012Fig6E-I-M
sensory	Peripheral Nervous System	mouse	Badea	Badea2012Fig6E-I-R
sensory	Peripheral Nervous System	mouse	Badea	Badea2012Fig6G
sensory	Peripheral Nervous System	mouse	Badea	Badea2012Fig6H
sensory	Peripheral Nervous System	mouse	Badea	Badea2012Fig6J
sensory	Peripheral Nervous System	mouse	Badea	Badea2012Fig6L
sensory	Peripheral Nervous System	mouse	Badea	Badea2012Fig7C

Table D.7. Data Sources for Glia - Astrocytes - Machine Learning Classification

Cell Type	Region	Species	Archive Name	File Name
astrocyte	hippocampus	rat	King	A1-CA1-L-C63x1zACR2
astrocyte	hippocampus	rat	King	A1-CA1-L-F63x1zACR1
astrocyte	hippocampus	rat	King	A2-CA1-L-A63x1zACR5
astrocyte	hippocampus	rat	King	A2-CA1-L-D63x1zACR1
astrocyte	hippocampus	rat	King	A2-CA1-R-H63x1zACR2
astrocyte	hippocampus	rat	King	A3-CA1-L-A63x1zACR3_1
astrocyte	hippocampus	rat	King	B4-CA1-L-A63x1zCell4ACR
astrocyte	hippocampus	rat	King	B4-CA1-L-C63x1zCell1ACR
astrocyte	hippocampus	rat	King	C6-CA1-L-D3x1zACR4
astrocyte	hippocampus	mouse	Zheng	PS19-C3aR-KO-astrocytes1
astrocyte	hippocampus	mouse	Zheng	PS19-C3aR-KO-astrocytes2
astrocyte	hippocampus	mouse	Zheng	PS19-astrocytes
astrocyte	neocortex	mouse	Hernandez-Garzon	S11_2_1
astrocyte	neocortex	mouse	Hernandez-Garzon	S2_3_1_2
astrocyte	neocortex	mouse	Hernandez-Garzon	S5_1_2
astrocyte	neocortex	mouse	Hernandez-Garzon	S7_1_2
astrocyte	neocortex	mouse	Hernandez-Garzon	S8_2_2
astrocyte	neocortex	mouse	Hernandez-Garzon	S9_2_2
astrocyte	basal ganglia	mouse	Hernandez-Garzon	Series027_1ok
astrocyte	basal ganglia	mouse	Hernandez-Garzon	Series029_3ok

Table D.8. Data Sources for Glia - Microglia - Machine Learning Classification

Cell Type	Region	Species	Archive Name	File Name
microglia	hippocampus	mouse	Bilkei-Gorzo	2_48
microglia	hippocampus	mouse	Bilkei-Gorzo	2_50
microglia	hippocampus	mouse	Bilkei-Gorzo	3_40
microglia	hippocampus	mouse	Bilkei-Gorzo	6_41
microglia	spinal cord	mouse	Morara	A11aCSF_Iba1-Z_32-26
microglia	spinal cord	mouse	Morara	A20CGRP_Iba1-Z_103-11
microglia	hypothalamus	rat	Althammer	PVN10_microglia_10
microglia	hypothalamus	rat	Althammer	PVN10_microglia_15
microglia	hypothalamus	rat	Althammer	PVN10_microglia_19
microglia	hypothalamus	rat	Althammer	PVN10_microglia_27
microglia	hypothalamus	rat	Althammer	PVN11_microglia_12
microglia	hypothalamus	rat	Althammer	PVN9_microglia_26
microglia	hypothalamus	rat	Althammer	PVN9_microglia_8
microglia	Central Nervous System	mouse	Abdolhoseini_Kluge	cell001_GroundTruth
microglia	Central Nervous System	mouse	Abdolhoseini_Kluge	cell004_GroundTruth
microglia	Central Nervous System	mouse	Abdolhoseini_Kluge	cell006_GroundTruth
microglia	Central Nervous System	mouse	Abdolhoseini_Kluge	cell010_GroundTruth
microglia	neocortex	rat	Roysam	farsight1083
microglia	neocortex	rat	Roysam	farsight1102
microglia	hippocampus	mouse	Bilkei-Gorzo	tgLPSF1684Iba1o_7

Table D.9. Data Sources for Motoneurons - Machine Learning Classification

Cell Type	Region	Species	Archive Name	File Name
motoneurons	spinal cord	rat	Alvarez	Alvarez-Control-Cell-3
motoneurons	spinal cord	rat	Alvarez	Alvarez-Regen-Cell-4
motoneurons	spinal cord	mouse	Branchereau_Cattaert	BranchereauCattaert_Scienfic Report2016_E17_5MN_x60
motoneurons	spinal cord	mouse	Branchereau_Cattaert	MartinNeurobiolDesease2013_ E17_5MN_SOD1G93A_x60
motoneurons	spinal cord	mouse	Branchereau_Cattaert	MartinNeurobiolDesease2013_ E17_5MN_WildType_x60
motoneurons	spinal neurons	cat	Burke	v_e_moto1
motoneurons	spinal neurons	cat	Burke	v_e_moto2
motoneurons	spinal neurons	cat	Burke	v_e_moto3
motoneurons	spinal neurons	cat	Burke	v_e_moto4
motoneurons	spinal neurons	cat	Burke	v_e_moto5
motoneurons	spinal neurons	cat	Burke	v_e_moto6

Table D.10. Data Sources for Purkinje Cells - Machine Learning Classification

Cell Type	Region	Species	Archive Name	File Name
purkinje	cerebellum	mouse	Dusart	Purkinje-slice-ageP35-1
purkinje	cerebellum	mouse	Dusart	Purkinje-slice-ageP35-2
purkinje	cerebellum	mouse	Dusart	Purkinje-slice-ageP35-3
purkinje	cerebellum	mouse	Dusart	Purkinje-slice-ageP35-4
purkinje	cerebellum	mouse	Dusart	Purkinje-slice-ageP37-5
purkinje	cerebellum	mouse	Dusart	Purkinje-slice-ageP43-6
purkinje	cerebellum	mouse	Watt	SCA6_P10_C1
purkinje	cerebellum	mouse	Watt	SCA6_P10_C5
purkinje	cerebellum	mouse	Watt	SCA6_P11_C2
purkinje	cerebellum	mouse	Watt	SCA6_P11_C3
purkinje	cerebellum	mouse	Watt	SCA6_P12_C4

Table D.11. Data Sources for D1-type dopamine receptor-expressing Medium Spiny Neuron (MSN) - Machine Learning Classification

Cell Type	Region	Species	Archive Name	File Name
D1 MSN	basal ganglia	mouse	Luebke	Apr12IR2a
D1 MSN	basal ganglia	mouse	Luebke	Apr12IR2a
D1 MSN	basal ganglia	mouse	Luebke	Apr26IR2e
D1 MSN	basal ganglia	mouse	Luebke	Apr29IR2a
D1 MSN	basal ganglia	mouse	Luebke	Apr29IR2b
D1 MSN	basal ganglia	mouse	Luebke	May24IR2b
D1 MSN	basal ganglia	mouse	Luebke	May5IR2a
D1 MSN	basal ganglia	mouse	Luebke	May9IR2a
D1 MSN	basal ganglia	mouse	Luebke	May9IR3b
D1 MSN	basal ganglia	mouse	Luebke	May9IR3d
D1 MSN	basal ganglia	mouse	Luebke	Nov3IR2c
D1 MSN	basal ganglia	mouse	Luebke	Nov8IR3a
D1 MSN	basal ganglia	mouse	Luebke	Nov9IR2a
D1 MSN	basal ganglia	mouse	Luebke	Nov9IR3c
D1 MSN	basal ganglia	mouse	Luebke	WT-D1-Jul19IR3d-stitch
D1 MSN	basal ganglia	mouse	Luebke	WT-D1-Jun19IR2a-whole-cell
D1 MSN	basal ganglia	mouse	Luebke	WT-D1-Jun27IR3b-whole-cell
D1 MSN	basal ganglia	mouse	Luebke	WT-D1-Jun5IR3b-whole-cell

Table D.12. Data Sources for D2-type dopamine receptor-expressing Medium Spiny Neuron (MSN) - Machine Learning Classification

Cell Type	Region	Species	Archive Name	File Name
D2 MSN	basal ganglia	mouse	Luebke	Apr12IR1b
D2 MSN	basal ganglia	mouse	Luebke	Apr12IR3a
D2 MSN	basal ganglia	mouse	Luebke	Apr12IR3b
D2 MSN	basal ganglia	mouse	Luebke	Apr19IR3f
D2 MSN	basal ganglia	mouse	Luebke	Apr26IR1a
D2 MSN	basal ganglia	mouse	Luebke	Apr29IR1c
D2 MSN	basal ganglia	mouse	Luebke	Apr29IR3a
D2 MSN	basal ganglia	mouse	Luebke	Nov3IR2a_1
D2 MSN	basal ganglia	mouse	Luebke	Nov3IR2d
D2 MSN	basal ganglia	mouse	Luebke	Nov3IR2e
D2 MSN	basal ganglia	mouse	Luebke	Nov3IR3b
D2 MSN	basal ganglia	mouse	Luebke	Nov8IR2b
D2 MSN	basal ganglia	mouse	Luebke	Nov9IR3b
D2 MSN	basal ganglia	mouse	Luebke	WT-D2-Jun19IR3a-whole-cell
D2 MSN	basal ganglia	mouse	Luebke	WT-D2-Jun27IR3c-whole-cell
D2 MSN	basal ganglia	mouse	Luebke	WT-D2-June19IR2c

Table D.13. Data Sources for Pyramidal Control Cells - Machine Learning Classification

Cell Type	Region	Species	Archive Name	File Name
pyramidal	neocortex	human	Allen Cell Types	H16-03-003-01-18-01_556380191_m
pyramidal	neocortex	human	Allen Cell Types	H16-03-008-11-11-02_601947643_m
pyramidal	neocortex	human	Allen Cell Types	H16-03-008-11-11-03_606347920_m
pyramidal	neocortex	human	Allen Cell Types	H16-06-004-01-04-01_538906745_m
pyramidal	neocortex	human	Allen Cell Types	H16-06-004-01-04-05_556380170_m
pyramidal	neocortex	human	Allen Cell Types	H16-06-004-01-13-02_538906639_m
pyramidal	neocortex	human	Allen Cell Types	H16-06-004-01-13-03_539990522_m
pyramidal	neocortex	human	Allen Cell Types	H16-06-004-02-13-04_538906871_m
pyramidal	neocortex	human	Allen Cell Types	H17-03-002-11-04-02_596792557_m
pyramidal	neocortex	human	Allen Cell Types	H17-03-002-11-04-04_603514410_m
pyramidal	neocortex	human	Allen Cell Types	H17-03-002-11-06-05_603514429_m
pyramidal	neocortex	human	Allen Cell Types	H17-06-003-11-05-01_605485079_m
pyramidal	neocortex	human	Allen Cell Types	H17-06-004-11-05-04_599474134_m
pyramidal	neocortex	human	Allen Cell Types	H17-06-004-11-05-05_605857665_m
pyramidal	neocortex	human	Allen Cell Types	H17-06-004-11-05-06_605851449_m
pyramidal	neocortex	human	Allen Cell Types	H17-06-005-12-10-07_605485535_m
pyramidal	neocortex	human	Allen Cell Types	H17-06-005-12-16-03_606347962_m
pyramidal	neocortex	human	Allen Cell Types	H17-06-006-11-08-04_585893370_m
pyramidal	neocortex	human	Allen Cell Types	H17-06-006-11-08-08_601946464_m
pyramidal	neocortex	human	Allen Cell Types	H17-06-006-11-09-04_591274508_m
pyramidal	neocortex	human	Allen Cell Types	H17-06-009-11-04-04_614429153_m

Table D.14. Data Sources for Pyramidal Tumor Cells - Machine Learning Classification

Cell Type	Region	Species	Archive Name	File Name
pyramidal	neocortex	human	Allen Cell Types	576110753_transformed
pyramidal	neocortex	human	Allen Cell Types	576118161_transformed
pyramidal	neocortex	human	Allen Cell Types	576134298_transformed
pyramidal	neocortex	human	Allen Cell Types	576140393_transformed
pyramidal	neocortex	human	Allen Cell Types	665713811_transformed
pyramidal	neocortex	human	Allen Cell Types	716918890_transformed
pyramidal	neocortex	human	Allen Cell Types	716929071_transformed
pyramidal	neocortex	human	Allen Cell Types	768819569_transformed
pyramidal	neocortex	human	Allen Cell Types	768848167_transformed
pyramidal	neocortex	human	Allen Cell Types	768867010_transformed
pyramidal	neocortex	human	Allen Cell Types	768885440_transformed
pyramidal	neocortex	human	Allen Cell Types	768904007_transformed
pyramidal	neocortex	human	Allen Cell Types	769228370_transformed

Table D.15. Data Sources for Pyramidal Epilepsy Cells - Machine Learning Classification

Cell Type	Region	Species	Archive Name	File Name
pyramidal	neocortex	human	Allen Cell Types	541557114_transformed
pyramidal	neocortex	human	Allen Cell Types	571732727_transformed
pyramidal	neocortex	human	Allen Cell Types	592532014_transformed
pyramidal	neocortex	human	Allen Cell Types	595572609_transformed
pyramidal	neocortex	human	Allen Cell Types	596898838_transformed
pyramidal	neocortex	human	Allen Cell Types	677088033_transformed
pyramidal	neocortex	human	Allen Cell Types	689306818_transformed
pyramidal	neocortex	human	Allen Cell Types	695521538_transformed
pyramidal	neocortex	human	Allen Cell Types	720828444_transformed
pyramidal	neocortex	human	Allen Cell Types	720862326_transformed
pyramidal	neocortex	human	Allen Cell Types	737089555_transformed
pyramidal	neocortex	human	Allen Cell Types	737134157_transformed
pyramidal	neocortex	human	Allen Cell Types	767433014_transformed
pyramidal	neocortex	human	Allen Cell Types	767829778_transformed
pyramidal	neocortex	human	Allen Cell Types	770255008_transformed
pyramidal	neocortex	human	Allen Cell Types	774420848_transformed
pyramidal	neocortex	human	Allen Cell Types	774620186_transformed
pyramidal	neocortex	human	Allen Cell Types	787239157_transformed
pyramidal	neocortex	human	Allen Cell Types	794276683_transformed
pyramidal	neocortex	human	Allen Cell Types	832627767_transformed

Bibliography

[1] M. Abdolhoseini et al. "Segmentation, Tracing, and Quantification of Microglial Cells from 3D Image Stacks". In: *Sci Rep.* 9(1) (2019), p. 8557. DOI: 10.1038/s41598-019-44917-6.

[2] M. A. Akram, Q. Wei, and G. A. Ascoli. "Machine learning classification reveals robust morphometric biomarker of glial and neuronal arbors". In: *Journal of Neuroscience Research* 101 (2022), pp. 112–129. DOI: 10.1002/jnr.25131.

[3] B. Jacobs et al. "Comparative neuronal morphology of the cerebellar cortex in afrotherians, carnivores, cetartiodactyls, and primates". In: *Front. Neuroanat.* 8 (2014), p. 24. DOI: 10.3389/fnana.2014.00024.

[4] G. W. Meissner et al. "A searchable image resource of Drosophila GAL4 driver expression patterns with single neuron resolution". In: *Elife* 12 (2023), e80660. DOI: 10.7554/eLife.80660.

[5] J. Berg et al. "Human cortical expansion involves diversification and specialization of supragranular intratelencephalic-projecting neurons". In: *bioRxiv* (2020). DOI: 10.1101/2020.03.31.018820.

[6] L. K. Scheffer et al. "A connectome and analysis of the adult Drosophila central brain". In: *Elife* 9 (2020), e57443. DOI: 10.7554/eLife.57443.

[7] R. Stephan et al. "Hierarchical microtubule organization controls axon caliber and transport and determines synaptic structure and stability". In: *Dev. Cell* 33 (2015), pp. 5–21. DOI: 10.1016/j.devcel.2015.02.003.

[8] F. Althammer et al. "Three-dimensional morphometric analysis reveals time-dependent structural changes in microglia and astrocytes in the central amygdala and hypothalamic paraventricular nucleus of heart failure rats". In: *J Neuroinflammation.* 17(1) (2020), p. 221. DOI: 10.1186/s12974-020-01892-4.

[9] A. Araque and M. Navarrete. "Glial cells in neuronal network function". In: *Philos Trans R Soc Lond B Biol Sci.* 365(1551) (2010), pp. 2375–81. DOI: 10.1098/rstb.2009.0313.

[10] G. A. Ascoli, D. E. Donohue, and M. Halavi. "NeuroMorpho.Org: a central resource for neuronal morphologies". In: *J Neurosci* 27(35) (2007), pp. 9247–51. DOI: 10.1523/JNEUROSCI.2055-07.2007.

[11] F. Ativie et al. "Cannabinoid 1 Receptor Signaling on Hippocampal GABAergic Neurons Influences Microglial Activity". In: *Front Mol Neurosci.* 11 (2018), p. 295. DOI: 10.3389/fnmol.2018.00295.

[12] D. Attwell and S. B. Laughlin. "An energy budget for signaling in the grey matter of the brain". In: *J. Cereb. Blood Flow Metab.* 21(10) (2001), pp. 1133–45. DOI: 10.1097/00004647-200110000-00001.

[13] D. Attwell et al. "Glial and neuronal control of brain blood flow". In: *Nature* 468 (2010), pp. 232–243. DOI: 10.1038/nature09613.

[14] T. C. Badea et al. "Combinatorial expression of Brn3 transcription factors in somatosensory neurons: genetic and morphologic analysis". In: *J Neurosci.* 32(3) (2012), pp. 995–1007. DOI: 10.1523/JNEUROSCI.4755-11.2012.

[15] A. P. Barnes and F. Polleux. "Establishment of Axon-Dendrite Polarity in Developing Neurons". In: *Annual Review of Neuroscience* 32 (2009), pp. 347–381. DOI: 10.1146/annurev.neuro.31.060407.125536.

[16] J. M. Bekkers and C. F. Stevens. "Two different ways evolution makes neurons larger". In: *Cell* 170(2) (1990), pp. 226–247. DOI: 10.1016/S0079-6123(08)61239-X.

[17] M. Bengochea et al. "A crustacean lobula plate: Morphology, connections, and retinotopic organization". In: *J Comp Neurol.* 526(1) (2018), pp. 109–119. DOI: 10.1002/cne.24322.

[18] L. P. Bentley et al. “An empirical assessment of tree branching networks and implications for plant allometric scaling models”. In: *Ecology Letters* 16 (2013), pp. 1069–1078. DOI: 10.1111/ele.12127.

[19] S. Boyd and L. Vandenberghe. *Convex Optimization*. Cambridge University Press, 2004.

[20] P. Branchereau et al. “Depolarizing GABA/glycine synaptic events switch from excitation to inhibition during frequency increases”. In: *Sci Rep.* 6 (2016), p. 21753. DOI: 10.1038/srep21753.

[21] A. B. Brummer and V. M. Savage. “Cancer as a Model System for Testing Metabolic Scaling Theory”. In: *Front. Ecol. Evol.* 9 (2021), p. 691830. DOI: 10.3389/fevo.2021.691830.

[22] A. B. Brummer, V.M. Savage, and B. J. Enquist. “A general model for metabolic scaling in self-similar asymmetric networks”. In: *PLoS Computational Biology* 13(3) (2017), e1005394. DOI: 10.1371/journal.pcbi.1005394.

[23] A. B. Brummer et al. “Branching principles of animal and plant networks identified by combining extensive data, machine learning and modelling”. In: *J. R. Soc. Interface* 18 (2021), p. 20200624. DOI: 10.1098/rsif.2020.0624.

[24] S. Ramón y Cajal. *Histologie Du Système Nerveux de L’homme & Des Vertébrés*. Trans. by N. Swanson and L. W. Swanson. New York: Oxford University Press, 1909.

[25] S. Cameron and Y Y. Rao. “Molecular mechanisms of tiling and self avoidance in neural development”. In: *Mol. Brain* 3(1) (2010), p. 28. DOI: 10.1186/1756-6606-3-28.

[26] C. Canavesi et al. “In vivo imaging of corneal nerves and cellular structures in mice with Gabor-domain optical coherence microscopy”. In: *Biomed Opt Express* 11(2) (2020), pp. 711–724. DOI: 10.1364/BOE.379809.

[27] S. Canchi et al. “Simulated blast overpressure induces specific astrocyte injury in an ex vivo brain slice model”. In: *PLoS One* 12(4) (2017), e0175396. DOI: 10.1371/journal.pone.0175396.

[28] X. R. Chen et al. “Mature Purkinje cells require the retinoic acid-related orphan receptor- (ROR) to maintain climbing fiber mono-innervation and other adult characteristics”. In: *J Neurosci* 33(22 (2013), pp. 9546–9562. DOI: 10.1523/JNEUROSCI.2977-12.2013.

[29] D. B. Chklovskii. “Synaptic Connectivity and Neuronal Morphology: Two Sides of the Same Coin”. In: *Neuron* 43 (2004), pp. 609–617. DOI: 10.1016/j.neuron.2004.08.012.

[30] D. B. Chklovskii and C. F. Stevens. “Wiring Optimization in Cortical Circuits”. In: *Adv. Neural Inf. Proc. Syst.* 34(3) (2002), pp. 341–347. DOI: 10.1016/S0896-6273(02)00679-7.

[31] N. M. Chmykhova et al. “Dorsal root afferent fiber termination in the spinal cord of the turtle Testudo horsfieldi and 3-dimensional reconstruction of the sensory-motoneuron connection”. In: *Tsitologiia* 50(10) (2008), pp. 843–854.

[32] S. Clavreul et al. “Cortical astrocytes develop in a plastic manner at both clonal and cellular levels”. In: *Nat Commun.* 10(1) (2019), p. 4884. DOI: 10.1038/s41467-019-12791-5.

[33] M. L. Concha, I. H. Bianco, and S. W. Wilson. “Encoding asymmetry within neural circuits”. In: *Nature Reviews Neuroscience* 13 (2012), pp. 832–843. DOI: 10.1038/nrn3371.

[34] R. Couronné, P. Probst, and A. L. Boulesteix. “Random forest versus logistic regression: a large-scale benchmark experiment”. In: *BMC bioinformatics* 19(1) (2018), p. 270. DOI: 10.1186/s12859-018-2264-5.

[35] S. Cullheim et al. “Membrane area and dendritic structure in type-identified triceps surae alpha motoneurons”. In: *J Comp Neurol.* 255(1) (1987), pp. 68–81. DOI: 10.1002/cne.902550106.

[36] H. Cuntz et al. “One rule to grow them all: a general theory of neuronal branching and its practical application”. In: *PLoS Comput Biol.* 6(8) (2010), e1000877. DOI: 10.1371/journal.pcbi.1000877.

[37] H. Cuntz et al. “The TREES toolbox-probing the basis of axonal and dendritic branching”. In: *Neuroinformatics* 9 (2011), pp. 91–96. DOI: 10.1007/s12021-010-9093-7.

[38] P. Desai-Chowdhry, A. B. Brummer, and V. M. Savage. “How Axon and Dendrite Branching Are Guided by Time, Energy, and Spatial Constraints”. In: *Scientific Reports* (2022). DOI: 10.1038/s41598-022-24813-2.

[39] P. Desai-Chowdhry et al. “Neuronal Branching is Increasingly Asymmetric Near Synapses, Potentially Enabling Plasticity While Minimizing Energy Dissipation and Conduction Time”. In: *bioRxiv* (2023). DOI: 10.1101/2023.05.20.541591.

[40] H. L. Moreand J. M. Donelan. “Scaling of sensorimotor delays in terrestrial mammals”. In: *Proc. Biol. Sci.* 285(1885) (2018), p. 20180613. DOI: 10.1098/rspb.2018.0613.

[41] J. E.Rash et al. “Molecular and Functional Asymmetry at a Vertebrate Electrical Synapse”. In: *Neuron* 79(5) (2013), pp. 957–969. DOI: 110.1016/j.neuron.2013.06.037.

[42] F. Leroy F et al. “Early intrinsic hyperexcitability does not contribute to motoneuron degeneration in amyotrophic lateral sclerosis”. In: *Elife* 3 (2014), e04046. DOI: 10.7554/eLife.04046.

[43] S. Fukuda, H. Maeda, and M. Sakurai. "Reevaluation of motoneuron morphology: diversity and regularity among motoneurons innervating different arm muscles along a proximal–distal axis". In: *Scientific Reports volume* 10 (2020), p. 13089. DOI: 10.1038/s41598-020-69662-z.

[44] F. Garrido-Charad et al. ""Shepherd's crook" neurons drive and synchronize the enhancing and suppressive mechanisms of the midbrain stimulus selection network". In: *Proc Natl Acad Sci U S A* 115(32) (2018), E7615–E7623. DOI: 10.1073/pnas.1804517115.

[45] A. Gellner, J. Reis, and B. Fritsch. "Glia: A Neglected Player in Non-invasive Direct Current Brain Stimulation". In: *Cell. Neurosci.* 10 (2016), p. 188. DOI: 10.3389/fncel.2016.00188.

[46] T. S. Gertler, C. S. Chan, and D. J. Surmeier. "Dichotomous anatomical properties of adult striatal medium spiny neurons." In: *J. Neurosci.* 28(43) (2008), pp. 10814–10824. DOI: 10.1523/JNEUROSCI.2660-08.2008.

[47] Adam Gomez. "Using Graph Theory to Compute Sets of Cycles in Vascular Networks". PhD thesis. University of California Los Angeles, 2019.

[48] P. T. Gonzalez-Bellido et al. "Eight pairs of descending visual neurons in the dragonfly give wing motor centers accurate population vector of prey direction". In: *Proc Natl Acad Sci U S A* 110(2) (2013), pp. 696–701. DOI: 10.1073/pnas.1210489109.

[49] J. W. Goodliffe et al. "Differential changes to D1 and D2 medium spiny neurons in the 12-month-old Q175+/- mouse model of Huntington's Disease". In: *PLoS One* 13(8) (2018), e0200626. DOI: 10.1371/journal.pone.0200626.

[50] J. A. Herman, A. B. Willits, and A. Bellemer. "Gαq and Phospholipase Cβ signaling regulate nociceptor sensitivity in Drosophila melanogaster larvae". In: *PeerJ* 6 (2018), e5632.

[51] D. E. Hillman. "Neuronal shape parameters and substructures as a basis of neuronal form". In: *Neurosciences: Fourth Study Program*. Ed. by G. Adelman and B. H. Smith. MIT Press, 1979, pp. 477–498.

[52] A. L. Hodgkin. "A note on conduction velocity". In: *J. Physiol.* 125(1) (1954), pp. 221–224. DOI: 10.1113/jphysiol.1954.sp005152.

[53] S. Jäkel and L. Dimou. "Glial Cells and Their Function in the Adult Brain: A Journey through the History of Their Ablation". In: *Front Cell Neurosci.* 11 (2017), p. 24. DOI: 10.3389/fncel.2017.00024.

[54] G. S. Jefferis et al. "Comprehensive maps of Drosophila higher olfactory centers: spatially segregated fruit and pheromone representation". In: *Cell* 128(6) (2007), pp. 1187–1203. DOI: 10.1016/j.cell.2007.01.040.

[55] D. St Johnston and J. Ahringer. "Cell Polarity in Eggs and Epithelia: Parallels and Diversity". In: *Cell* 141(5) (2010), pp. 757–774. DOI: 10.1016/j.cell.2010.05.011.

[56] D.W. Johnston and S. M. Wu. *Foundations of Cellular Neurophysiology*. MIT Press, 1995.

[57] R. Kaib. "Regulation of motor neuron dendrite growth by NMDA receptor activation". In: *Development* 120 (1994), pp. 3063–3071. DOI: 10.1.1.117.6925&rep=rep1&type=pdf.

[58] E. Katifori and M. O. Magnasco. "Quantifying loopy network architectures". In: *PLoS One* 7(6) (2012), e37994. DOI: 10.1371/journal.pone.0037994.

[59] E. Katifori, G. J. Szollosi, and M. O. Magnasco. "Damage and Fluctuations Induce Loops in Optimal Transport Networks". In: *J Neurophysiol* 104(4) (2010), p. 048704. DOI: 10.1103/PhysRevLett.104.048704.

[60] M. Kleiber. "Body size and metabolism". In: *Hilgardia* 6 (1932), pp. 315–353. DOI: 10.3733/hilg.v06n11p315.

[61] C. Koch and A. Jones. "Big Science, Team Science, and Open Science for Neuroscience". In: *Neuron* 92(3) (2016), pp. 612–616. DOI: 10.1016/j.neuron.2016.10.019.

[62] X. Z. Kong et al. "Mapping cortical brain asymmetry in 17,141 healthy individuals worldwide via the ENIGMA Consortium". In: *Proceedings of the National Academy of Sciences of the United States of America* 115(22) (2018), E5154–E5163. DOI: 10.1073/pnas.1718418115.

[63] V. Lanoue and H. M. Cooper. "Branching mechanisms shaping dendrite architecture". In: *Developmental Biology* 451(1) (2019), pp. 16–24. DOI: 10.1016/j.ydbio.2018.12.005.

[64] S. B. Laughlin and T. J. Sejnowski. "Communication in neuronal networks". In: *Science* 301(5641) (2003), pp. 1870–1874. DOI: 10.1126/science.1089662.

[65] D. R. Lesniak et al. "Computation identifies structural features that govern neuronal firing properties in slowly adapting touch receptor". In: *Elife* 3 (2014), e01488. DOI: 10.7554/eLife.01488.

[66] M. Liao, X. Liang, and J. Howard. "The narrowing of dendrite branches across nodes follows a well-defined scaling law". In: *PNAS* 118(27) (2021), e2022395118. DOI: 10.1073/pnas.2022395118.

[67] C. Ligneul et al. "Diffusion-weighted magnetic resonance spectroscopy enables cell-specific monitoring of astrocyte reactivity in vivo". In: *Neuroimage.* 191 (2019), pp. 457–469. DOI: 10.1016/j.neuroimage.2019.02.046.

[68] A. Litvinchuk et al. "Complement C3aR Inactivation Attenuates Tau Pathology and Reverses an Immune Network Deregulated in Tauopathy Models and Alzheimer's Disease". In: *Neuron* 100(6) (2018), 1337–1353.e5. DOI: 10.1016/j.neuron.2018.10.031.

[69] S. Jayabal Sand L. Ljungberg and A. J. Watt. "Transient cerebellar alterations during development prior to obvious motor phenotype in a mouse model of spinocerebellar ataxia type 6". In: *J Physiol.* 595(3) (2017), pp. 949–966. DOI: 10.1113/JP273184.

[70] X. H. Lu and X. W. Yang. "Genetically-directed sparse neuronal labeling in BAC transgenic mice through mononucleotide repeat frameshift". In: *Sci. Rep.* 7 (2017), p. 43915. DOI: 110.1038/srep43915.

[71] A. de Luca et al. "Distinct modes of neuritic growth in purkinje neurons at different developmental stages: axonal morphogenesis and cellular regulatory mechanisms". In: *PLoS One* 4(8) (2009), e6848. DOI: 10.1371/journal.pone.0006848.

[72] J. Luts et al. "A tutorial on support vector machine-based methods for classification problems in chemometrics". In: *Analytica Chimica Acta* 665(2) (2010), pp. 129–145. DOI: 10.1016/j.aca.2010.03.030.

[73] L. F. Martins et al. "Mesenchymal stem cells secretome-induced axonal outgrowth is mediated by BDNF". In: *Sci Rep* 7(1) (2017), p. 4153. DOI: 10.1038/s41598-017-03592-1.

[74] M. Martone et al. "CCDB:19, rattus norvegicus, Purkinje neuron". In: *Cell Image Library* Dataset (2002). DOI: doi:10.7295/W9CCDB19.

[75] M. E. Martone et al. "The cell-centered database: a database for multiscale structural and protein localization data from light and electron microscopy". In: *Neuroinformatics* 1(4) (2003), pp. 379–395. DOI: 10.1385/NI:1:4:379.

[76] M. Megjhani et al. "Population-scale three-dimensional reconstruction and quantitative profiling of microglia arbors". In: *Bioinformatics* 31(13) (2015), pp. 2190–8. DOI: 10.1093/bioinformatics/btv109.

[77] H. Memelli, B. Torben-Nielsen, and J. Kozloski. "Self-referential forces are sufficient to explain different dendritic morphologies". In: *Front. Neuroinform.* 7 (2013), p. 1. DOI: 10.3389/fninf.2013.00001.

[78] V. I. Mironov, A. V. Semyanov, and V. B. Kazantsev. "Dendrite and Axon Specific Geometrical Transformation in Neurite Development". In: *Front. Comput. Neurosci.* 9 (2016), p. 156. DOI: 10.3389/fncom.2015.00156.

[79] J. R. Morrice, C. Y. Gregory-Evans, and C. A. Shaw. "Modeling Environmentally-Induced Motor Neuron Degeneration in Zebrafish". In: *Sci Rep* 8(1) (2018), p. 14890. DOI: 10.1038/s41598-018-23018-w.

[80] S. De Munter et al. "Early-onset Purkinje cell dysfunction underlies cerebellar ataxia in peroxisomal multifunctional protein-2 deficiency". In: *Neurobiol Dis.* 94 (2016), pp. 157–168. DOI: 10.1016/j.nbd.2016.06.012.

[81] S. Murru et al. "Astrocyte-specific deletion of the mitochondrial m-AAA protease reveals glial contribution to neurodegeneration". In: *Glia* 67(8) (2019), pp. 1526–1541. DOI: 10.1002/glia.23626.

[82] Sukenik N et al. "Neuronal circuits overcome imbalance in excitation and inhibition by adjusting connection numbers". In: *Proc. Natl. Acad. Sci. USA* 118 (12) (2021), e2018459118. DOI: 10.1073/pnas.2018459118.

[83] S. Nanda et al. "Distinct Relations of Microtubules and Actin Filaments with Dendritic Architecture". In: *iScience* 23(12) (2020), p. 101865. DOI: 10.1016/j.isci.2020.101865.

[84] S. Nanda et al. "Morphological determinants of dendritic arborization neurons in Drosophila larva". In: *Brain Struct Funct.* 223(3 (2018), pp. 1107–1120. DOI: 10.1007/s00429-017-1541-9.

[85] M. G. Newberry, D. B. Ennis, and V. M. Savage. "Testing Foundations of Biological Scaling Theory Using Automated Measurements of Vascular Networks". In: *PLoS Computational Biology* 11(8) (2015), e1004455. DOI: 10.1371/journal.pcbi.1004455.

[86] S. Ocklenburg and O. Güntürkün. "Hemispheric asymmetries: the comparative view". In: *Front. Psychol.* 3 (2012), p. 3. DOI: 10.3389/fpsyg.2012.00005.

[87] N. Ofer, O. Shefi, and G. Yaari. "Branching morphology determines signal propagation dynamics in neurons". In: *Sci Rep* 7 (2017), p. 8877. DOI: 10.1038/s41598-017-09184-3.

[88] F.Y. Osisanwo et al. "Supervised Machine Learning Algorithms: Classification and Comparison". In: *International Journal of Computer Trends and Technology (IJCTT)* 48(3) (2017), pp. 128–138. DOI: 10.14445/22312803/IJCTT-V48P126.

[89] R. Parekh and G. A. Ascoli. "Neuronal Morphology Goes Digital: A Research Hub for Cellular and System Neuroscience". In: *Neuron* 77 (2013), pp. 1017–1038. DOI: 10.1016/j.neuron.2013.03.008.

[90] A. Peters. "The effects of normal aging on myelin and nerve fibers: a review". In: *J Neurocytol.* 31(8-9) (2002), pp. 581–93. DOI: 10.1023/a:1025731309829.

[91] C. A. Price and B. J Enquist. "Scaling mass and morphology in leaves: An extension of the WBE model". In: *Ecology* 88 (2007), pp. 1132–1141. DOI: 10.1890/06-1158.

[92] D. Purves, G. J. Augustine, and D. Fitzpatrick et al. "Excitatory and Inhibitory Postsynaptic Potentials". In: *Neuroscience 2nd edition*. Sinauer Associates, 2001.

[93] W. Rall. "Branching dendritic trees and motoneuron membrane resistivity". In: *Exp. Neurol* 1(5) (1959), pp. 491–527. DOI: 10.1016/0014-4886(59)90046-9.

[94] W. Rall. "Core Conductor Theory and Cable Properties of Neurons". In: *Handbook of Physiology, The Nervous System, Cellular Biology of Neurons* (1977). DOI: 10.1002/cphy.cp010103.

[95] M. Rapp, I. Segev, and Y. Yarom. "Physiology, morphology and detailed passive models of guinea-pig cerebellar Purkinje cells". In: *J Physiol.* 474(1) (1994), pp. 101–118. DOI: 10.1113/jphysiol.1994.sp020006.

[96] K. F. Riley, M. P. Hobson, and S. J. Bence. *Manual for Mathematical Methods for Physics and Engineering*. New York: Cambridge University Press, 2006.

[97] J. L. Ringo et al. "Time is of the essence: a conjecture that hemispheric specialization arises from interhemispheric conduction delay". In: *Cere Cortex* 4 (1994), pp. 331–343. DOI: 10.1093/cercor/9.1.2.

[98] I. Rossetti et al. "Calcitonin gene-related peptide decreases IL-1beta, IL-6 as well as Ym1, Arg1, CD163 expression in a brain tissue context-dependent manner while ameliorating experimental autoimmune encephalomyelitis". In: *J Neuroimmunol.* 323 (2018), pp. 94–104. DOI: 10.1016/j.jneuroim.2018.07.005.

[99] T. M. Rotterman et al. "Normal distribution of VGLUT1 synapses on spinal motoneuron dendrites and their reorganization after nerve injury". In: *J Neurosci.* 34(10) (2014), pp. 3475–3492. DOI: 10.1523/JNEUROSCI.4768-13.2014.

[100] W. A. H. Rushton. "A theory of the effects of fiber size in medullated nerve". In: *J. Physiol.* 115 (1951), pp. 101–122. DOI: 10.1113/jphysiol.1951.sp004655.

[101] A. Samara. "Single neurons needed for brain asymmetry studies". In: *Front. Genet.* 4 (2014), p. 311. DOI: 10.3389/fgene.2013.00311.

[102] A. Sarica, A. Cerasa, and A. Quattrone. "Random Forest Algorithm for the Classification of Neuroimaging Data in Alzheimer's Disease: A Systematic Review". In: *Analytica Chimica Acta* 9 (2017). DOI: 10.3389/fnagi.2017.00329.

[103] V. M. Savage, E. J. Deeds, and W. Fontana. "Sizing up Allometric Scaling Theory". In: *PLoS Computational Biology* 4(9) (2008), e1000171. DOI: 10.1371/journal.pcbi.1000171.

[104] V. M. Savage et al. "Scaling of number, size, and metabolic rate of cells with body size in mammals". In: *Proc. Natl. Acad. Sci. U.S.A.* 6104(11) (2007), pp. 4718–4723. DOI: 10.1073/pnas.0611235104.

[105] P.C. Sen, M. Hajra, and M. Ghosh. "Supervised Classification Algorithms in Machine Learning: A Survey and Review". In: *Emerging Technology in Modelling and Graphics. Advances in Intelligent Systems and Computing*. Ed. by J. Mandal and D. Bhattacharya. Vol. 937. Springer, Singapore, 2020. DOI: 10.1007/978-981-13-7403-6_11.

[106] H. Shevalye et al. "Effect of enriching the diet with menhaden oil or daily treatment with resolvin D1 on neuropathy in a mouse model of type 2 diabetes". In: *J Neurophysiol* 114(1) (2015), pp. 199–208. DOI: 10.1152/jn.00224.2015.

[107] K. Shinomaya et al. "Comparisons between the ON- and OFF-edge motion pathways in the Drosophila brain". In: *Elife* 8 (2019), e40025. DOI: 10.7554/eLife.40025.

[108] D. D. Smith et al. "Deviation from symmetrically self-similar branching in trees predicts altered hydraulics, mechanics, light interception and metabolic scaling". In: *New Phytologist* 201 (2014), pp. 217–229. DOI: 10.1111/nph.12487.

[109] L. R. Squire et al. *Fundamental Neuroscience*. Academic Press, 2013.

[110] P. R. Steele et al. "Altered Motoneuron Properties Contribute to Motor Deficits in a Rabbit Hypoxia-Ischemia Model of Cerebral Palsy". In: *Front Cell Neurosci* 14 (2020), p. 69. DOI: 10.3389/fncel.2020.00069.

[111] D. B. Chklovskiiand A. Stepanyants. "Power-law for axon diameters at branch point." In: *BMC Neurosci* 4 (12003), p. 18. DOI: 10.1186/1471-2202-4-18.

[112] A. J. Svahn et al. "Nucleo-cytoplasmic transport of TDP-43 studied in real time: impaired microglia function leads to axonal spreading of TDP-43 in degenerating motor neurons". In: *Acta Neuropathol.* 136(3) (2018), pp. 445–459. DOI: 10.1007/s00401-018-1875-2.

[113] Z. Szepesi et al. "Bidirectional Microglia–Neuron Communication in Health and Disease". In: *Front Cell Neurosci.* 12 (2018), p. 323. DOI: 10.3389/fncel.2018.00323.

[114] E. Tekin et al. “Do Vascular Networks Branch Optimally or Randomly across Spatial Scales?” In: *PLoS Comput Biol* 12(11) (2016), e1005223. DOI: 10.1371/journal.pcbi.1005223.

[115] D. Tsigankov and A. Koulakov. “Optimal axonal and dendritic branching strategies during the development of neural circuitry”. In: *Front Neural Circuits* 3 (2009), p. 18. DOI: 10.3389/neuro.04.018.2009.

[116] D. L. Turcotte, J. D. Pelletier, and W. I. Newman. “Networks with Side Branching in Biology”. In: *J. theor. Biol.* 193 (1998), pp. 577–592. DOI: 10.1006/jtbi.1998.0723.

[117] K. Vervaeke, A. Lorinczand Z. Nusser, and R. A. Silver. “Gap junctions compensate for sublinear dendritic integration in an inhibitory network”. In: *Science* 335(6076) (2012), pp. 1624–8. DOI: 10.1126/science.1215101.

[118] P. Vetter, A. Roth, and M. Häusser. “Propagation of action potentials in dendrites depends on dendritic morphology”. In: *J Neurophysiol.* 85(2) (2001), pp. 926–937. DOI: 10.1152/jn.2001.85.2.926.

[119] F. Vidal, C. Meckler, and T. Hasbroucq. “Basics for sensorimotor information processing: Some implications for learning”. In: *Front. Psychol.* 6 (2015), p. 33. DOI: 10.3389/fpsyg.2015.00033.

[120] A. Vormberg et al. “Universal features of dendrites through centripetal branch ordering”. In: *PLoS Comput Biol.* 13(7) (2017), e1005615. DOI: 10.1371/journal.pcbi.1005615.

[121] S. S. Wang et al. “Functional trade-offs in white matter axonal scaling”. In: *J. Neurosci.* 28(15) (2008), pp. 4047–4056. DOI: 10.1523/JNEUROSCI.5559-05.2008.

[122] S. G. Waxman and H. A. Swadlow. “The conducting properties of axons in central white matter”. In: *Progress Neurobiol.* 8 (1977), pp. 297–324. DOI: 10.1016/0301-0082(77)90009-0.

[123] Q. Wen and D. B. Chklovskii. "A cost-benefit analysis of neuronal morphology". In: *J. Neurophysiol.* 99(5) (2008), pp. 2320–2328. DOI: 10.1152/jn.00280.2007.

[124] Q. Wen et al. "Maximization of the connectivity repertoire as a statistical principle governing the shapes of dendritic arbors". In: *Proc. Natl. Acad. Sci. USA* 106(30) (2009), pp. 12536–12541. DOI: 10.1073/pnas.090153010.

[125] G. B. West, J. H. Brown, and B. J. Enquist. "A general model for the origin of allometric scaling laws in biology". In: *Science* 276(5309) (1997), pp. 122–126. DOI: 10.1126/science.276.5309.122.

[126] G. M. Wittenberg and S. S.-H. Wang. "Phylogeny and Evolution of Dendrites". In: *Dendrites (2nd edition)*. Ed. by G. Stuart. Vol. 42-67. Oxford University Press, 2007.

[127] B. Ye et al. "Differential regulation of dendritic and axonal development by the novel Krüppel-like factor Dar1". In: *J Neurosci.* 31(9) (2011), pp. 3309–19. DOI: 10.1523/JNEUROSCI.6307-10.2011.

[128] M. Zamir. "On fractal properties of arterial trees". In: *J Theor Biol.* 197(4) (1999), pp. 517–26. DOI: 10.1006/jtbi.1998.0892.

[129] M. Zamir. *The Physics of Coronary Blood Flow*. New York: Springer, 1995.

[130] H. Zeng and J. R. Sanes. "Neuronal cell-type classification: Challenges, opportunities and the path forward". In: *Nat. Rev. Neurosci.* 18 (2017), pp. 530–546. DOI: 10.1038/nrn.2017.85.